

# Electrochemical Phase Formation of Ni and Ni-Fe Alloys in a Magnetic Field

## DISSERTATION

zur Erlangung des akademischen Grades  
Doctor rerum naturalium  
(Dr. rer. nat.)

vorgelegt  
der Fakultät Mathematik und Naturwissenschaften  
der Technischen Universität Dresden

von  
Ispas, Adriana

geboren am 26. Juni 1977 in Buzău, Rumänien

Gutachter: Professor Waldfried Plieth (Technische Universität Dresden)  
Professor Ulrich Guth (Technische Universität Dresden)  
Professor Frank Endres (Technische Universität Clausthal)

Eingereicht am: 12.04.2007

Tag der Verteidigung: 31.08.2007



## Summary

Summary .....	I
Motivation .....	1
I. Theoretical aspects .....	5
I.1 Electrodeposition of Ni and Ni-Fe Alloys. Mechanisms .....	5
I.1.1 Nickel Electrodeposition .....	5
I.1.2 Hydrogen Evolution Reaction .....	6
I.1.3 Models for Ni-Fe Alloy Electrodeposition.....	6
I.2 Piezoelectricity and the Quartz Crystal Microbalance .....	8
I.3 Effects of a Superimposed Static Magnetic Field .....	11
I.3.1 Magnetic Field Effects in Electrodeposition .....	11
I.3.2 Magnetic Anisotropy .....	15
I.3.3 Magnetic Field and the Resonance Frequency of the Quartz.....	17
I.4 Preferred Crystal Orientations: Theories.....	18
I.5 Nucleation and Growth. Theoretical Aspects.....	20
I.5.1 Formation of Nuclei .....	20
I.5.2 Classical Growth Models .....	23
I.5.3 The Role of Overpotential in the Nucleation and Growth Processes.....	23
I.5.4 Theories for the Chronoamperometric Transients of Nucleation and Growth... 26	
I.5.4.a Scharifker-Hills model .....	26
I.5.4.b Scharifker-Mostany model .....	27
I.5.4.c Heerman-Tarallo model .....	28
II. Experimental Details .....	31
II.1 Experimental Techniques .....	31
II.1.1 Electrochemical Quartz Crystal Microbalance (EQCM) .....	31
II.1.2 Vibrating Sample Magnetometer (VSM).....	32
II.1.3 Atomic Force Microscopy (AFM) .....	33
II.1.4 Scanning Electron Microscopy (SEM).....	34
II.1.5 Energy Dispersive X-Ray (EDX).....	35
II.1.6 X-Ray Diffractometer (XRD) .....	35
II.2 Experimental Set-up and Electrolytes .....	37
III. Ni Electrodeposition.....	42
III.1 Nucleation and Growth of Ni: Bath with 0.01M Ni.....	42
III.1.1 Cyclic Voltammetry Analysis .....	42
III.1.2 Potentiostatic Step Experiments.....	47
III.1.2.a Magnetic Field Effects on the Current Transients.....	48
III.1.2.b Magnetic Field Effects on the Deposited Mass.....	53
III.1.2.c Magnetic Field Effects on the Nucleation and Growth.....	55

III.1.3	AFM Investigations on the Topography, Roughness and Grains Size of Deposited Ni Layers.....	61
III.2	Ni Electrodeposition from a Sulfamate Bath.....	63
III.2.1	XRD Investigations.....	66
III.2.2	Magnetic Field Effects on HER and Current Efficiency.....	69
III.2.3	Magnetic Field Effects on the Potential Transients.....	73
III.2.4	Morphology Aspects.....	74
III.2.5	Magnetic Properties of Electrodeposited Ni Layers.....	84
IV.	Ni-Fe Alloy codeposition in a Magnetic Field.....	87
IV.1	Initial Stages of Ni-Fe Alloys codeposition.....	87
IV.2	Effects Induced by Variations in the Total Current and by the Presence of a Magnetic Field in the Properties of Ni-Fe Alloys.....	93
IV.2.1	Effect of the Total Current Density on the Alloy Composition.....	93
IV.2.1.a	Ni-Fe alloy containing less than 10 at% Fe.....	94
IV.2.1.b	Ni-Fe alloy containing approximately 20 at% Fe.....	96
IV.2.2	Effect of a Superimposed Magnetic Field on the Alloy Composition.....	97
IV.2.2.a	Ni-Fe alloys containing less than 10 at% Fe.....	97
IV.2.2.b	Ni-Fe alloys containing approximately 20 at% Fe.....	99
IV.3	HER during Ni-Fe alloy codeposition.....	100
IV.4	Morphology and Roughness of Ni-Fe layers.....	103
IV.5	XRD Analysis.....	107
IV.5.1	Ni-Fe Alloys containing less than 10at.% Fe.....	107
IV.5.2	Permalloy.....	111
V.	Conclusions and Outlook.....	113
V.1	Conclusions for Ni Electrodeposition in a Magnetic Field.....	113
V.1.1	Ni Layers Electrodeposited from a dilute Ni Electrolyte.....	113
V.1.2	Ni Layers Electrodeposited from Ni-Sulfamate Electrolytes.....	115
V.2	Conclusions for Ni-Fe Alloys Electrodeposition in a Magnetic Field.....	117
VI.	References.....	121
VII.	Appendix.....	135

## Motivation

Magnetohydrodynamics (MHD) is a combination of two well known aspects: fluid dynamics and electromagnetism [1]. MHD studies the motion of electrically conducting fluids in magnetic fields. Thus, it has two main parts: the effects produced by the fluid flow on the magnetic field and the effect induced by the field on the flow.

Although the term MHD was coined in the 20<sup>th</sup> century, pioneering work was done in 1830 by Faraday, who tried to measure the velocity of the river Thames by using the magnetic field of the earth. But the enormous interest in this new science started when the astrophysicists realized that some stars, which are composed of plasma, have a magnetic field. Then it was thought that the astronomical phenomena could have a MHD explanation. The dynamo theory was developed, which explains the appearance of the magnetic field of the earth on the basis of MHD effects.

MHD effects are interesting not only in astronomy, but also on smaller scales, in the experiments made in a laboratory [2,3]. Electrodeposition has become an intensively used method in nanotechnology. Thus, Cu electrodeposition is used for example in fabrication of submicrometer interconnects of microelectronic devices [4], while ferromagnetic layers are used in the fabrication of magnetic writing/reading devices [5]. On a nanometre scale it is challenging to control the electrodeposition process. In order to obtain the desired surfaces and structures, a mixture of additives is usually added [4,5]. Instead of using the additives to control the properties and structure of the deposited layers, an external magnetic field could be used.

If the experimental conditions are chosen carefully, some useful effects can be promoted during metal electrodeposition by a magnetic field [3]. A superimposed magnetic field can change the crystallization behaviour and induce a more uniform deposited layer, and a more uniform current distribution. At the same time, the hardness of the deposit can increase, the macrostress of the layers can change, and their corrosion properties can be improved [3]. The composition of alloys can be changed under a superimposed magnetic field [3,6,7].

A superimposed magnetic field can affect the flow pattern of fluids. Thus, forces can be induced that will cause a preferential flow of the fluid [2]. If the electrochemical reaction is mass transport controlled, an increase of the limiting current density and of the deposition rate was reported [2,8] for specific configuration of the electrochemical cell. In other configurations (for example when the magnetic field is applied parallel to the electric

current), it was reported that the mass transport can be retarded [3].

Most of the effects induced by a magnetic field, which were reported in the literature, are described just qualitatively, and many of them are not yet fully understood. Furthermore, the reported results are often contradictory. Thus, different effects were claimed to be induced by an external magnetic field on the texture of the galvanostatically and potentiostatically deposited Ni layers. Yang [9] observed no effect on the crystalline orientation, while Chiba et al. [11] and Devos et al. [10] reported that the magnetic field changes the preferred crystalline orientation of Ni layers. Danilyuk [12] argued that the difference in the results reported is due to the fact that certain values of a magnetic field accelerate the electrodeposition reaction, while other values inhibit it. But the electrolyte composition and the deposition conditions were proved to play a more important role than the magnetic field intensity [13].

There is a lack of experimental data that presents the influence of the magnetic field on the nucleation and growth process. Recently, at least two PhD theses discussed the nucleation in a magnetic field of Cu [14] and Cu/Co [15]. The author of the present thesis could not find literature that discussed the influence of a magnetic field on the initial stages of Ni electrodeposition. The first part of this work is dedicated to this topic.

Ni and Ni-Fe alloy electrodeposition occur in parallel to the hydrogen evolution reaction (HER). The HER is a side reaction that reduces the efficiency of the electrodeposition process and can induce changes in the morphology of the deposited layers. The experimental method used in this study (Electrochemical Quartz Crystal Microbalance, EQCM, see sections I.2, p.8 and II.1.1, p.31) allows to determine with high accuracy the partial current of the HER. One can obtain from the EQCM data the current that corresponds just to Ni, or Ni-Fe alloy electrodeposition. This information is important when the experimental current transients are compared to different theoretical models, which describe nucleation and growth.

The HER is mass transport controlled. Thus, one can expect a strong effect of an external magnetic field, in terms of increasing of the limiting current density [3,8]. Similar to the HER, the Fe electrodeposition is usually mass transport controlled. Ni electrodeposition is (usually) mixed controlled. Due to many practical applications of thin and thick Ni layers, the effects induced by a magnetic field on Ni electrodeposition are intensely studied in the literature [8]. However, most of the experiments reported in the literature were performed with the Watts electrolyte, which contains  $\text{NiSO}_4$ ,  $\text{H}_3\text{BO}_3$  and  $\text{NiCl}_2$ . The changes of the morphology of the deposited layers and of the preferred crystalline orientation in a magnetic

field were reported, but these results are often controversial [9-13]. In the present study Ni electrodeposition from a sulfamate bath was investigated under the influence of a magnetic field. The sulfamate electrolyte was chosen because of its high relevance in technical applications, which is based on the very high plating rates and the low internal stresses in the deposit [16]. Typical technical applications comprise electroforming, surface finishing and the fabrication of microelectromechanical systems (MEMS) by the LIGA process [16-18]. Ni-Fe alloys are interesting especially in the microelectronics industry, due to their unique magnetic properties [19-34]

The aim of this work was to identify the effects induced by a superimposed magnetic field on the nucleation and growth of ferromagnetic layers, as well as the effects induced on the properties of the layers. The effects of a magnetic field on the grain size, texture, morphology and roughness of the deposited Ni and Ni-Fe alloys were investigated. The influence of a magnetic field on the magnetic properties of Ni layers and on the composition of Ni-Fe alloys was also studied.

At the same time, the magnetic field effects on the mass transport processes were analysed. The changes with the magnetic field of the HER during Ni and Ni-Fe alloys will be presented. The variation of the deposited mass and of the current or potential transients recorded during electrodeposition will be discussed.

This work was done at the Technical University of Dresden within the Collaborative Research Center 609 “Electromagnetic Flow Control in Metallurgy, Crystal Growth and Electrochemistry”.





## I. Theoretical aspects

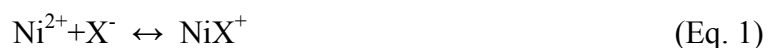
A short introduction of the mechanisms that govern the electrodeposition of Ni and Ni-Fe alloy is given in the beginning of this section (I.1). Most of the experiments reported in this thesis were performed with the Electrochemical Quartz Crystal Microbalance (EQCM) technique. Therefore, the piezoelectric effect and some basics on the functionality of the EQCM are described (I.2, p.8). If during the electrodeposition process a static magnetic field is superimposed, specific effects can be induced. Some possible effects (on the electrodeposition process, on the magnetic properties of the deposited layers or on the resonance frequency of the quartz crystal) will be shortly presented (I.3, p.11). Electrodeposited Ni and Ni-Fe alloys present a preferred crystalline orientation. Thus, some models that describe the formation of the texture for electrodeposited layers will be presented (I.4, p.18). Part of the experimental results deals with the effect induced by a magnetic field on the nucleation and growth of Ni. Therefore, the last part of the introduction is dedicated to some theories which describe the formation of new nuclei by electrodeposition and their growth (I.5, p.20).

### ***I.1 Electrodeposition of Ni and Ni-Fe Alloys. Mechanisms***

#### **I.1.1 Nickel Electrodeposition**

Nickel electrodeposition from aqueous solutions is known since 1837 [35,36]. Starting from then, many studies were done to improve the properties of the deposited layers. Thus, Ni electrodeposition was investigated from different baths, with different pH values, at different current densities and temperatures, and on different substrates.

The generally accepted deposition mechanism for Ni involves two consecutive one-electron charge transfer steps with the formation of an adsorbed cationic Ni-containing complex (Eq. 1-3), [37]:



The anion  $\text{X}^-$  was assumed to be  $\text{OH}^-$ ,  $\text{SO}_4^{2-}$  or  $\text{Cl}^-$  [37].

### I.1.2 Hydrogen Evolution Reaction

Hydrogen Evolution Reaction (HER) takes place simultaneously with the Ni or Ni-Fe alloy electrodeposition on a cathode surface. There is a three-reaction mechanism proposed for the HER (Eq.4-6), [38]:



Equation 4 is known as the Volmer reaction. Equation 5 is called the Heyrovsky reaction or the electrochemical desorption (ion-atom recombination) and Eq. 6 is known as the Tafel reaction or atom-atom recombination. Me represents the metal surface of the cathode. According to [38], the HER on Au and on Ni substrates occurs first via the Volmer reaction (that is the slowest), followed by the Heyrovsky reaction. According to [39], for metals that are good catalysts for the HER, the Tafel reaction is the rate determining step at low overpotentials, while at higher overpotentials the Heyrovsky mechanism becomes the rate determining step. The Volmer reaction is the rate determining step at very high overpotentials. Normally, the Volmer reaction is followed either by the Tafel or by Heyrovsky reaction.

### I.1.3 Models for Ni-Fe Alloy Electrodeposition

Alloy deposition represents the simultaneous deposition of more than one metal [19]. There are some advantages in depositing the alloys, like some of the alloys can be deposited without much difficulty and that some of the alloys have useful properties (finer grains, harder, stronger, more corrosion resistant than the parent metals, high magnetic permeability). These advantages made possible the replacement of the single metals by alloys in some applications. One of the disadvantages of the alloy deposition is in some cases the need to control the electrolytic bath carefully during the deposition [19].

The electrodeposition of Ni-Fe alloys has been and it is still intensively studied [19-34]. The motivations are the special properties of these alloys like high internal strength, hardness and special magnetic properties.

Ni-Fe alloy deposition (Fe-50%Ni) has a decorative applications, while Fe-80%Ni, which is also called Permalloy, is being used for magnetic purposes [35]. Ni-Fe alloys are

magnetically isotropic (that means the N or S pole direction of each crystal is randomly oriented), and this property makes them very interesting in microelectronics. The permalloys present one of the best magnetic properties needed in the magnetic applications like a maximum permeability and a high coercive force. It is reported that the magnetic properties vary with the thickness of the deposit and that the best magnetic properties are obtained for a thickness between 500- 5000Å [40]. Beside the thickness of the deposited layer, the magnetic properties depend on the composition of the deposit, roughness of the substrate, crystal size and internal stress in the deposit [40-42].

A superimposed magnetic field during the deposition can influence the deposition process and the properties of the electrodeposited alloys. One of the points of interest of the present work was to investigate if and how the intensity of an external magnetic field and its direction affect the properties of the Ni-Fe alloys.

The deposition of Ni-Fe alloys was classified by Brenner [19] to be an anomalous one, which means that the less noble metal (iron) is deposited preferentially compared to the more noble one (nickel).

Some models were developed during the last years to explain this behaviour. Dahms and Croll [20] explained the anomalous codeposition via the pH increase in front of the cathode. This would induce the formation of nickel and iron hydroxides. The iron hydroxides are the source for the iron deposition and at the same time suppress the adsorption of nickel at the electrode surface. Hessami and Tobias developed a mathematical model (solved numerically) that included the mass transfer equations and the interfacial kinetics in order to evaluate the surface pH, the formation of metal-hydroxide ions and the surface concentration of the metal ions [21]. They explained the inhibition of the Ni partial current with the smaller surface concentration of  $\text{NiOH}^+$  compared to the  $\text{FeOH}^+$ , which has the smaller dissociation constant. Matlosz [22] confirmed by calculations based on a competitive adsorption model that the reduction of nickel and iron are two-step reactions. The inhibition of nickel at a specific potential is due to the preferential surface coverage of the adsorbed iron intermediate and does not need necessary a variation of the pH. Landolt [23] underlined the importance of considering both the thermodynamic and kinetic factors when discussing the deposition of the alloys, which he explained with the mixed potential theory. A recent theory [24] developed for the nickel-iron deposition from a sulfate bath (identical with the bath that is used in the present study) claims that the electroactive species are the  $\text{Ni}^{2+}$  and the  $\text{Fe}^{2+}$  and that the hydroxide species are not involved in the reaction mechanism. A very recent model that describes the occupation of the kink site positions by the various components of

the alloy based on the finite Markov chain theory was proposed by Plieth and Georgiev [25-29]. This model describes the relationship between the alloy composition and the corresponding metal ion concentrations in the electrolyte. The model is based on the definition of residence times of the Fe and Ni atoms in the kink site positions of the surface [25,26]. The selectivity of the alloy surface for the metal ions in the electrolyte is described by selectivity constants,  $g_{Fe}$  and  $g_{Ni}$ . The selectivity constants explain the anomalous deposition by the different residence times of the alloy components on the surface. At higher current densities the selectivity constants represent the ratio of the partial currents of Fe and Ni.

## ***1.2 Piezoelectricity and the Quartz Crystal Microbalance***

$\alpha$ -Quartz is a piezoelectric material. The piezoelectricity was discovered in 1880 by Jacques and Pierre Curie and represents the appearance of an electric potential across a crystal when a mechanical stress is applied on it. The charges generated in a quartz crystal can be explained on the basis of acentricity of this material. Thus, when a mechanical stress is applied on the crystal, the atoms of the crystalline structure will move and dipoles will result [43,44].

The inverse piezoelectric effect consists in a mechanical movement of the crystal when a potential is applied on its faces. If an alternating potential is applied, an oscillatory motion of the quartz crystal will result. Because quartz crystals can vibrate with small energy dissipation, they can be used to build very stable oscillator circuits [43]. The quartz oscillator has a strong preference to vibrate at a characteristic resonant frequency ( $f_0$ ), which depends on the shear modulus ( $\mu_q$ ), density ( $\rho_q$ ) and the thickness of the quartz ( $t_q$ ),  $f_0=(\mu_q/\rho_q)^{1/2}/2t_q$ . AT quartzes were used in this work, which are obtained by cutting the quartz wafer at approximately 35° from the z-axis. The AT-cut has a minimal dependence of the resonance frequency on the temperature.

Sauerbrey described how the resonance frequency of a quartz crystal can change when a foreign mass is deposited on the top of the oscillator (Eq. 7).

$$\Delta f = -\frac{2f_0^2}{Z_q} \Delta m \quad (\text{Eq. 7})$$

where  $\Delta f$  represents the shift in the resonance frequency of the quartz crystal when a rigid mass density,  $\Delta m$ , is deposited on one side of the resonator,  $Z_q$  is the mechanical impedance

of quartz ( $Z_q=(\mu_q\rho_q)^{1/2}$ ) and  $f_0$  is the resonance frequency of the unloaded quartz. This equation is valid just if the mechanical impedance of the deposited layers does not differ strongly from that of the quartz crystal and if the deposited layer has a uniform thickness. Practically, masses up to 10% from the quartz mass can be calculated with the Sauerbrey equation, (Eq. 7).

Because the quartz crystal can be used to monitor mass changes, it is usually referred as the Quartz Crystal Microbalance (QCM). It can also be applied in electrochemistry, in order to monitor in-situ the mass changes at one electrode surface (working electrode) during electrochemical measurements. In this case, the technique is called Electrochemical Quartz Crystal Microbalance, EQCM. The sensitivity of the EQCM is high: a shift of one Hertz in the resonance frequency of a 10 MHz quartz crystal corresponds to a mass change of  $4.425 \text{ ng cm}^{-2}$ .

When an AT-cut quartz vibrates, a transverse acoustic wave occurs that will propagate through the quartz crystal and that will be reflected at the surface of the quartz. Thus, AT-cut quartzes can be seen as electroacoustical resonators [44], as they combine mechanic and electric properties. In order to understand the oscillating properties of the QCM, equivalent circuits can be constructed.

In fact, all the electroacoustical resonators can be described by some mechanical and electrical equivalent circuits. For the quartz crystal, two electrical models are often used: the transmission line model and the Butterworth-van Dyke circuit [45]. These models were made in order to describe the propagation of the acoustic wave in analogy with the electrical waves. We will discuss just the Butterworth-van Dyke circuit.

The oscillating properties of a quartz crystal can be easily understood if one understands how a simple R-L-C system works, connected to a generator of rectangular potential. After applying the potential, the capacitor starts to be charged, the charging current grows from zero to a maximum value, and after that it starts to decrease. Because the current inside is changing, an autoinduced electromotive force will appear in the inductor. After some time, a stationary state will be reached, when the capacitor is charged with the maximum charge, and the current in the circuit becomes zero. The energy given by the generator will be partially stored between the plates of the capacitor- as electrical energy, partially taken by the inductor- as magnetic energy, and the rest will be dissipated on the total resistance of the circuit. When the external potential is not applied any longer, the capacitor starts to loose the charge, but not at once; the existence of the inductor will delay the discharge of the capacitor. A discharging current, which is opposite to the charging

current, will flow in the circuit. This will induce an electromotive force in the inductor, in an opposite direction to the initial current. The final result will be a zero current in the circuit and a zero charge on the capacitor. The repetition of this process will make an electrical oscillation, attenuated in time because of the existence of the total resistance of the circuit.

The oscillation of a quartz resonator, produced by the application of an alternating potential on opposite faces, is similar to the electrical oscillations of an R-L-C system. But in the description of an oscillating quartz, one has to take into account also other elements, like the capacity induced by the presence of the two electrodes on the surface.

The electrical equivalent circuit of a quartz resonator has two branches: one is the “shunt” branch, that contains just the capacitor  $C_0$ , that is the shunt capacitance of the crystal electrodes, and the other branch is the “motional” branch. This second branch contains the R-L-C circuit, to which can be added the mass or the viscous loading of the quartz crystal, in form of a mechanical load (Fig. 1).

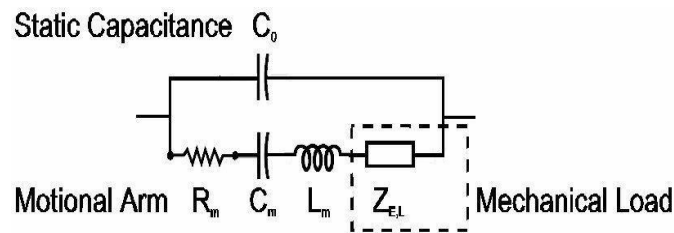


Figure 1. Equivalent electric circuit for a quartz resonator according to the Butterworth-van Dyke model.

At the resonance frequency, the electric impedance of the quartz crystal has a minimum, which makes the admittance maximum. The admittance is proportional to the current that goes across the device when an external potential is applied. It is a complex value, which can be expressed by a real component and an imaginary one [45,46]. When a foreign mass is deposited on the quartz crystal, its resonance frequency will shift (Eq. 7). One can express this shift in frequency as a complex entity, where the real part is the shift in frequency ( $\Delta f$ ), and the imaginary part is proportional with the shift in the full width at half maximum, FWHM, ( $\Delta w$ ) (Eq. 8, [46]):

$$\Delta f^* = \Delta f + i \frac{\Delta w}{2} = (f - f_0) + i \frac{(w - w_0)}{2} \quad (\text{Eq. 8})$$

Here  $f_0$  and  $w_0$  are the frequency and the full width at half maximum for the unloaded quartz.

A network analyser provides the real part of the admittance (Fig. 2, and section II.1).

One can calculate the mechanical impedance of the layer (Eq. 9, [46]):

$$Z_M^* = Z_M' + iZ_M'' = \frac{-\pi Z_q \Delta f}{f_0} + i \frac{\pi Z_q \Delta w}{2f_0} \quad (\text{Eq 9})$$

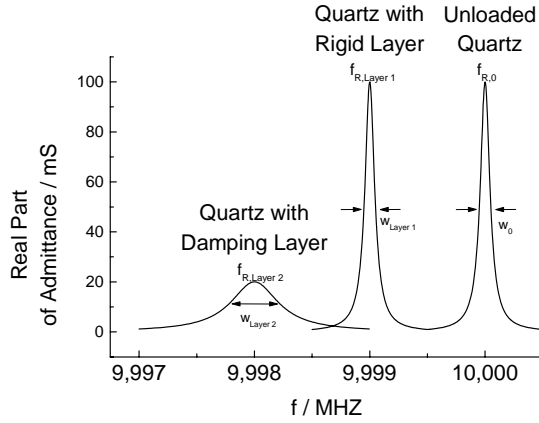


Figure 2. Resonance curves measured with a network analyzer for an unloaded quartz, a quartz loaded with a rigid layer and a quartz loaded with a viscous layer.

From the frequency shift one can get information about the mass deposited on the quartz (Eq. 7), while from the FWHM shift one can get information about the damping of the quartz [46,47]. Furthermore, from the damping information semi-quantitative information about the surface roughness can be obtained in situ [48-50].

The FWHM is given only by the network analyser measurements. The energy dissipation during the quartz oscillations can be found in the values of the motional resistance,  $R_m$  (Fig. 1), when the measurements are performed with a Phase Lock Oscillator (PLO) (see section II.1.1).  $R_m$  includes the internal friction, mechanical losses in the mounting system and acoustical losses due to the surrounding environment.

### ***1.3 Effects of a Superimposed Static Magnetic Field***

#### **1.3.1 Magnetic Field Effects in Electrodeposition**

The effects that a static magnetic field can produce during electrochemical processes have been summarized in a recent review by Fahidy [51]. His conclusions were that the magnetic field can influence the transport of the electroactive species, the kinetics of the charge transfer, corrosion rates and the properties of the deposited layer. Besides these

effects on the electrochemical reaction changes of the electrolyte behaviour have been observed, too. These comprise the Hall effect, changes in the values of diffusivity and in viscosity, and variation of equilibrium composition in electrolytes with the magnetic flux density. However, most of these effects are described only qualitatively in the literature, and in most cases not well understood.

Among the effects, which are fairly understood is the magnetohydrodynamic effect (MHD) [51-54]. When a magnetic field is applied to an electrochemical cell, the charged particles that are moving in the electrolyte will experience a Lorentz force density,  $F_L$ , (Eq. 10)

$$\vec{F}_L = \vec{j} \times \vec{B} \quad (\text{Eq. 10})$$

which is perpendicular to the current density,  $j$ , and the magnetic flux density,  $B$ . This force will induce convective movements in the solution. The flow profile and the Lorentz force density are related by the Navier-Stokes Equation (NSE). Taking into consideration the complex geometries of cells and electrodes usually used, an analytical solution of the NSE will be difficult in most cases. There are, however, some analytical and numerical approaches for simple geometries and boundary conditions [54,55].

Aogaki [56] mentioned that the total MHD effect would be due to the sum of local Lorentz forces. These will usually produce small “circular” convection movements. The overall effect will be a tangential convection at the electrode surface that reduces the diffusion layer thickness. As a consequence the limiting current density,  $j_L$ , increases. A linear dependence of  $j_L$  with  $B^{1/3}$  was reported in the literature [57,58] in the case of millielectrodes. For microelectrodes, Ragsdale et al. affirmed that  $j_L$  is almost proportional with  $B$  [59]. It has been reported that depending on the geometry of the cell and the interplay of the magnetic forces with the natural convection  $j_L$  can also decrease [60,61].

In electrolytes that contain paramagnetic ions ( $\text{Cu}^{2+}$ ,  $\text{Fe}^{2+}$ ,  $\text{Co}^{2+}$ ,  $\text{Ni}^{2+}$ , etc) one should take into account also the magnetic force generated by the concentration gradient of these paramagnetic species [59,62,63] (Eq. 11).

$$\vec{F}_{\nabla c} = \frac{\chi_m B^2}{2\mu_0} \vec{\nabla} c \quad (\text{Eq. 11})$$

where  $\chi_m$  is the molar susceptibility,  $c$  the concentration and  $\mu_0$  the vacuum permeability, ( $\mu_0=4\pi*10^{-7}$  H m<sup>-1</sup>). Because  $B$  enters as square in Eq. 11 the effects due to this force should depend just on the magnitude of the magnetic induction and not its direction. Coey et al. argue that this force is six orders of magnitude smaller compared with the other forces occurring in an electrochemical reaction (mainly diffusion and migration) [64]. Therefore,



the effects produced by this paramagnetic force should be relatively small. Another force that can influence the electrodeposition process is due to the gradient of the magnetic field (Eq. 12).

$$\vec{F}_{\nabla B} = c \frac{\chi_m B \vec{\nabla} B}{\mu_0} \quad (\text{Eq. 12})$$

This force appears in the case that the magnetic field is inhomogeneous. It should be noted that the deposition of thick ferromagnetic layers could cause such inhomogeneities. However, in most cases the forces will be small compared to diffusion and/or migration forces [64]. The conclusion of Coey et al. was that the effects of the forces described by (Eq. 10)-(Eq. 12) are non negligible just in the case when they are combined with the convective movements in the solution [64].

When the magnetic field is applied perpendicular to the electric current,  $F_L$  is maximal, while in magnetic field parallel to the electric field,  $E$ , the Lorentz force should be negligible, but concentration gradient forces,  $F_{\nabla c}$ , can still be active due to concentration gradients of paramagnetic ions, (Eq. 11). The works of Iwakura et al. [65], Aogaki et al. [66,67], Shannon et al. [68], Arumugam et al. [69] show the role of the direction of  $B$  with regard to  $E$ . For example, in [66] it is claimed that microturbulences will appear when the magnetic field is parallel to the electric field, which will locally suppress the nucleation. Therefore, a specific morphology will be generated [66,70]. The existence of the microturbulences mentioned above can be explained based on one theory about the mechanism of nucleation in the absence of a magnetic field. In this theory, two types of fluctuation responsible for the electrodeposition are proposed [71]. A magnetic field parallel to an electric field will induce two types of vortices from these fluctuations, and the interaction between them will generate a velocity of the fluctuations [66]. The final effect will be local Lorentz forces around the growing nuclei.

The effects that the magnetic fields can induce on the kinetics of the charge transfer are discussed controversially in literature [72,73]. It is difficult to distinguish clearly between kinetic effects and effects arising from magnetically induced mass transport. The general tendency in the recent literature [58,73-77] is to affirm that the magnetic field is not influencing the kinetics of the charge transfer, and that all the effects reported in literature are due to the changes of the active area of the electrodes, or due to an indirect transport that is not controlled.

When discussing the effects induced by a magnetic field in electrodeposition processes, one should take into account the natural convection, too. Natural convection is driven by

density gradients which appear as a consequence of the electrochemical reaction. For a cathodic deposition metal ions are removed from the electrolyte near the electrode which causes a decrease of the density. It was proved that the thickness of the deposited layers is not uniform all over a vertical cathode surface [78], this being caused by different concentrations at different heights of the cathode. A flow of the electrolyte from lower to upper part of a vertical cathode is generated [79]. A superimposed magnetic field during electrodeposition will generate a MHD body force that can point upwards or downwards to the electrode surface, parallel to the natural convection. Due to the interplay between the MHD convection and the natural convection, deposits of uniform thickness can be obtained if one designs carefully the electrochemical cells [80].

If the cathode is fixed at an arbitrary angle with regard to the gravitational force direction, the interplay between the natural convection and the MHD flow can not be described in a simple way [81]. Thus, Quraishi and Fahidy [81] reported that the mass transport is not influenced by the value of the inclination angle for specific range of Hartman's number,  $H_a$ , ( $H_a = |B|(L/2)(\sigma_{av}\mu_{av})^{1/2}$ , where  $B$  is the magnetic flux density,  $L$  the distance between cathode and anode,  $\sigma_{av}$  the average conductivity between bulk and electrode surface and  $\mu_{av}$  the averaged dynamic viscosity). At the same time, for other values of the inclination angle between the cathode and the gravitational force, a strong effect on the mass transport could be noticed [81].

Some theoretical studies were done in order to understand the effects of natural convection in electrochemical reactions. The limiting current of Cu deposition and the relative ionic mass coefficients for different electrochemical systems were calculated. The later can be used to determine the buoyancy force [82,83]. For Cu it has been pointed out that the electrode arrangement with regard to the gravitational field can influence the nucleation behaviour [84], the size of the crystals [85] and the pattern of the fractal growth [77]. If the anode was placed above the cathode, more nuclei appeared due to a Rayleigh-Bénard type natural convection [84] and a decrease of the fractal dimensionality was observed [77]. Furthermore, it has been reported [85] that the plating rate of Cu can be suppressed in the presence of a  $B$  field parallel to the  $E$  field, but promoted by a  $G$  field (gravity) parallel to the  $E$  field.

The effect of natural convection on the flow and concentration profiles can be verified by optical methods [86-88]. Unfortunately those methods cannot be applied to our experimental setup (recessed electrode).

### I.3.2 Magnetic Anisotropy

Before describing the magnetic anisotropy, the notions of magnetic moment and magnetization will be remembered. Most of the magnetism of matter is generated by electrons. The simplified models of an atom describe it as small solar system, where the electrons rotate around the nucleus like the planets around sun and also around their own axis. The movement of electrons will produce magnetism. The first component of the electron motion produces the orbital magnetism, which is not important in most solids. The second component of the electron motion (spin movement of electrons around their own axis) produces most of the magnetism (electron spin magnetism). The magnetic moment ( $m$ ) characterizes quantitatively the magnetism of a particle. For a close elementary loop of area  $A$  through which a current ( $I$ ) can pass, one can define the magnetic moment as the product between the current and the area of the loop.

In ferromagnetic materials, the spins of neighbouring atoms are strongly coupled by an exchange force, which makes them all to point in the same direction within a magnetic domain. The magnetization of a medium is a property of the material, defined as the magnetic moment on an elementary volume. The magnetization of a material depends on the individual magnetic moments of constituent ions or atoms and how these dipole moments interact with each other.

The ferromagnetic materials have an easy axis along which the magnetization prefers to lie. By applying an external magnetic field the magnetization can rotate from the easy axis, thus the internal energy of a magnetic material will change. This phenomenon is known as magnetic anisotropy [89].

The orientation of the magnetization is normally the result of the energy balance between the exchange energy, the dipolar energy, the magneto-crystalline energy and the magneto-elastic energy [89]. One might assume that an external magnetic field which is applied during the deposition of a ferromagnetic layer might induce some magnetic anisotropy. Corresponding to the types of energies, there are different types of anisotropy, like magneto-crystalline anisotropy, shape anisotropy, exchange anisotropy or the induced magnetic anisotropy [90]. In the following we will discuss them shortly.

From all the anisotropy types mentioned above, the magneto-crystalline anisotropy is the strongest one [90]. Therefore it has the most important influence on the magnetic properties of ferromagnetic samples.

For cubic crystals, like Ni and Fe, the anisotropy energy can be expressed in terms of the

cosines ( $\alpha_1, \alpha_2, \alpha_3$ ) of the angles between the magnetization vector and the axis of the cube [89] (Eq. 13):

$$E_a = K_1(\alpha_1^2\alpha_2^2 + \alpha_2^2\alpha_3^2 + \alpha_3^2\alpha_1^2) + K_2\alpha_1^2\alpha_2^2\alpha_3^2 + K_3(\alpha_1^2\alpha_2^2 + \alpha_2^2\alpha_3^2 + \alpha_3^2\alpha_1^2)^2 + \dots \quad (\text{Eq. 13})$$

where  $K_i$  are called the anisotropy constants that are dependent on temperature. For Fe at 20°C,  $K_1 > 0$  while for Ni,  $K_1 < 0$ . Thus it can be shown ([89], Fig. 3) that the easy axis for Fe is [100] (or its equivalent ones [010] or [001]) and for Ni the [111] (or its equivalent directions  $[\bar{1}11]$ ,  $[1\bar{1}1]$  and  $[11\bar{1}]$ ). “ $\bar{1}$ ” defines the negative direction of an axis.

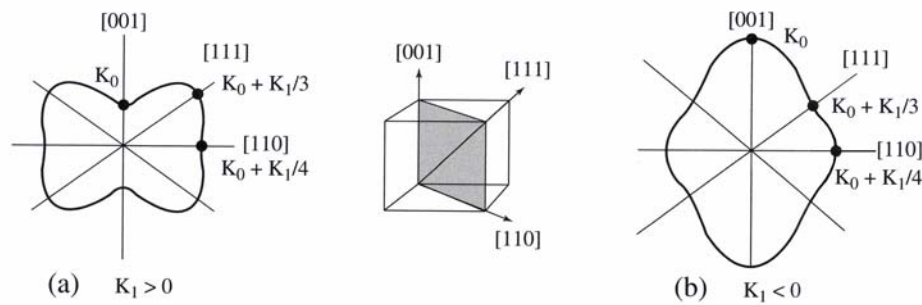


Figure 3. Polar diagrams of the cubic (magneto-crystalline) anisotropy energy from reference [90]. The energy is represented as function of the angle that the magnetization vector makes with the plane that contains all the three main directions of symmetry.  $K_0$  is a constant that was introduced to make the representation easier.

The magneto-crystalline energy is caused by the spin-orbit coupling. This anisotropy favors a magnetization along a given crystalline axis, called easy axis of magnetization, and may be responsible for a magnetization perpendicular to the plane of growth.

The shape anisotropy is produced by the dipole-dipole interaction. The magnetostatic energy produced by all the dipoles from a specimen depends on the shape of the specimen. If the ferromagnetic specimen is elongated along one direction, the magnetization will tend to lie along this direction. In the case of a deposited magnetic layer, the shape anisotropy favors the in plane magnetization. It has been reported that dipolar forces can influence the process of nucleation and growth of a layer, for example in the case of iron arborescent growth [91].

The exchange anisotropy is produced by the exchange energy at the surface of a magnetic specimen [89]. Usually, the magnetic moments of a substance interact with each other or with the surrounding medium. For example, if a magnetized sample is cooled in the presence of a magnetic field, the magnetization vector can rotate along the direction of the external field. This type of anisotropy is called the exchange anisotropy and together with the magneto-crystalline anisotropy is responsible for the magnetic behavior of materials at

microscopic scales [90]. This type of anisotropy manifests itself by a shift of the hysteresis curves to the left [89].

The stress anisotropy or the anisotropy of magnetostriction is the result of a phenomenon called magnetostriction of exchange [90]. That implies the deformation of the crystalline cell when the intensity and the direction of the magnetization of a ferromagnetic specimen change [89]. The magnetostriction of exchange can appear at very low temperatures, which are below the temperature where the crystalline order forms, or under the influence of an external magnetic field [90]. The deformation induced will not affect the symmetry of the specimen, therefore, in the case of isotropic substances or for those that present cubic symmetry, just a variation of the volume will appear. This anisotropy can be visualized as a shift of reflections in the XRD pattern.

The induced magnetic anisotropy is produced by a treatment (often an annealing treatment) of the magnetic specimen [89]. However, other treatments like rolling during the cooling of the alloys, neutron irradiation, crystallographic transformation, etc. [89] can induce different anisotropies. For example, the phase transformation of Co from fcc (face-centred-cubic) into hcp (hexagonal-closed-packed) can occur by cooling a polycrystalline Co in a magnetic field [89]. The induced magnetic anisotropy can be ignored in the present study, as no thermal treatment was applied to the deposited layers.

### **I.3.3 Magnetic Field and the Resonance Frequency of the Quartz**

The quartz is very sensitive to small perturbations, like those produced by changes in mass loading, viscosity, electrical conductivity or dielectric properties of the crystal [43]. An external magnetic field can be one source of perturbation.

In the literature are discussed some possible causes for the quartz resonators sensitivity to an external magnetic field [92,93]. The force induced by the non-homogeneity of the magnetic field, that depends on the gradient of  $B$  and the magnetic susceptibility of the quartz, which could generate a shift in frequency, is quite small (10-14N); the eddy currents that can change the motional resistance of the quartz are also small. Therefore, the changes of the resonance frequency and of the damping of the quartz in a magnetic field can be due to secondary electric fields that can appear from the simultaneous action of magnetic and electric fields [92]. Ferromagnetic springs used to hold the quartz plate were also mentioned to cause changes in the resonance frequency of the quartz crystal [92].

The experiments that we did in order to check the influence of a magnetic field on the resonance frequency of the quartz crystal showed a shift of approximately 40 Hz in the frequency (for the quartz in electrolyte) and 20 Hz (for a quartz in air), when the electromagnet was turned on ( $B=206\text{mT}$ ). The change in damping during the starting or stopping the current through the coils of the electromagnet was of approximately 150 Hz in electrolyte and around 15Hz in air. This jump appears just when the electromagnet is started or stopped, for some fractions of seconds. During the continuous operation of the electromagnet, the resonance frequency and the damping are oscillating around a constant level, with a corresponding noise. As the magnetic field does not perturb the quartz crystal during the time when the magnetic flux density was constant, all the measurements were performed after the electromagnet was turned on.

### ***1.4 Preferred Crystal Orientations: Theories***

A crystalline material is characterized by the macroscopic and microscopic symmetry. The macroscopic symmetry represents the symmetry of the external form of a crystalline solid. It is expressed through the existence of symmetric planes, borders and edges. The microscopic symmetry is reflected through the periodic distribution of atoms, ions or molecules in a crystalline material. In crystallography, the term texture is introduced to define the preferred orientation of the crystalline grains along specific crystalline planes or crystalline directions.

The interest in finding the preferred crystal orientation of electrodeposited layers dates back as early as 1924, when Glocker and Kaupp [94] reported that electrodeposited Copper, Silver, Chromium, Nickel and Iron crystallites presented a preferred crystalline orientation  $[hkl]$ , grown parallel to the direction of the electric field. “ $h,k,l$ ” are known as the Miller indexes and they will be further presented in section II.1.6.

Several mechanisms have been proposed to describe the appearance of a texture. Pangarov [95] made a competitive nucleation model. He affirmed that firstly two-dimensional nuclei are formed and that their orientation depends on the cathodic overvoltage. This preferred orientation cannot be changed by the three-dimensional crystallites, which grow latter. Some authors confirmed this theory [96,97], some contradicted it [98]. In another model, Reddy [99] invoked the growth competition induced by the adsorbed hydrogen ( $H_{\text{ads}}$ ). The critics to this model referred to the fact that the

hydrogen is not the only inhibiting species [100]. Furthermore, the model considered the competition occurring just between single crystals. In reality it was observed that texture like  $\{211\}$ ,  $\{110\}$  or  $\{111\}$  are polycrystalline [98] (the  $\{hkl\}$  defines all the  $(hkl)$  planes that present the same symmetry properties). Amblard [98,101] explained the texture development via the selective adsorption theory. Different species can be present in the diffusion layer, like hydrogen, hydroxides, organic complexes, etc. The presence of these species depends on the local pH value and on the electrochemical balance between various cathodic reactions that occur at a given potential. They may block growth sites or slow down the propagation of steps. Textured deposits indicate that at least one crystal direction is not blocked during the growth process.

Li and Szpunar [102-104] made Monte Carlo simulations as well as experiments to find the mechanism that governs the texture formation of electrodeposited Fe in an external magnetic field. They affirmed that two energies are responsible for the formation and development of the texture: the surface energy (expressed in terms of surface-energy anisotropy) and magnetic free energy (discussed in terms of magnetocrystalline anisotropy). The surface anisotropy of a crystalline plane  $(hkl)$  is given by the difference between the free energies of the crystal's surface layer and its middle plane. Both planes are parallel to the  $(hkl)$  plane. The magnetocrystalline anisotropy (see section I.3.2) is given by the difference between the magnetization energies of differently oriented grains. If a grain of a ferromagnetic material grows along the easy axis of magnetization it will be easier magnetized (provided the growth occurs in a magnetic field) and it will have smaller magnetization energy. If the grains are oriented randomly this anisotropy will not have an important contribution. The magnetocrystalline anisotropy should modify the preferred orientation of grains.

It is well known that the texture of the deposited layers is affected by several factors [103]. The current density was proved to be an important one [94,96]. Furthermore, the HER that accompanies the deposition can lead to a change of the texture. This can be attributed to the fact that the adsorbed hydrogen can change the surface energy of the deposited layers and it can also induce an increase of the pH in front of the working electrode. The later induces the formation of inhibiting metal hydroxide species that can be specifically adsorbed [7,10].

Other factors that were invoked to affect the texture of the deposited layers are the solution pH, the concentration of the active species, the presence of different inhibitors (like 2-butyne-1,4-diol,  $\text{HO-CH}_2\text{-C}\equiv\text{C-CH}_2\text{-OH}$ ) [98,101] or the mass transport conditions [105].

Many studies analysed the changes in the texture of different metals induced by the factors mentioned above. Therefore, in the present study just the influence of a magnetic field on the preferred orientation will be discussed.

An orientation index,  $M(hkl)$ , was introduced in the literature in order to find the preferred crystalline orientation [96]:

$$M(hkl) = \frac{\frac{I(hkl)}{\sum I(h'k'l')}}{\frac{I_0(hkl)}{\sum I_0(h'k'l')}} \quad (\text{Eq.14})$$

where  $I(hkl)$  represents the intensity of the diffraction peak measured,  $I_0(hkl)$  is the intensity in JCPDS (Joint Committee for Powder Diffraction Studies) cards, and  $\sum I(hkl)$  is the sum of the intensity of all the peaks that appeared in a XRD-diffractogram.

It was shown that the highest intensity of the XRD pattern does not (always) correspond to the texture axis [106]. Thus, the orientation index is useful to find the preferred plane (hkl) of growth. The latter corresponds to the maximum value in the orientation index.

## ***1.5 Nucleation and Growth. Theoretical Aspects***

### **1.5.1 Formation of Nuclei**

After introducing a metal electrode in an aqueous solution of its ions, a thermodynamic equilibrium will be established, that can be expressed as a potential difference ( $E_{\text{Me}/\text{Me}^{z+}}$ ) between the electrode and the electrolyte.  $E_{\text{Me}/\text{Me}^{z+}}$  depends on the type of metal electrode and also on the concentration of metal ions.

$$E_{\text{Me}/\text{Me}^{z+}} = E_{\text{Me}/\text{Me}^{z+}}^0 + \frac{RT}{zF} \ln \frac{a_{\text{Me}^{z+}}}{a_{\text{Me}}} \quad (\text{Eq. 15})$$

Equation 15 is known as Nernst's equation. Here  $E$  is the Nernst potential of the electrode;  $E_0$  is the standard electrode potential;  $R$  is the universal gas constant (8.315 J / K mol);  $T$ - temperature;  $F$ - Faraday constant (96485 C / mol);  $z$ - the number of transferred electrons and  $a_{\text{Me}^{z+}}$  is the activity of  $\text{Me}^{z+}_{\text{solv}}$  ions in the electrolyte. The term  $a_{\text{Me}}$  is unity for a pure  $\text{Me}$  bulk phase.

Three stages can be identified in an electrodeposition process: formation of metal ad-atoms, via adsorption ( $\text{Me}_{\text{ads}}$ ), nucleation ( $\text{Me}$  phase formation by phase transitions) and crystal growth.



Under the influence of an imposed electric field, metal atoms are ionized at the anode, and then hydrated. The ions move through electrolyte by migration, diffusion or convection (Fig. 4). When they reach the cathode surface, the ions lose some hydrating molecules and they will retain part of their charge. Thus, they become adsorbed ions. The “ad-ion“ is the entity that results from transfer from the solution side of the double layer to the electrode. This term ad-ion was introduced by Conway and Bockris [107], who made fundamental pioneering research about the manner in which the hydration sheath is stripped from the metal ion and how the ion is incorporated in the lattice. The ad-ion can diffuse across the electrode surface to a crystal building site (kink site), which is a site of low energy. In the kink-site the ad-ion will be recombined with the missing number of electrons that are needed to form the metal phase.

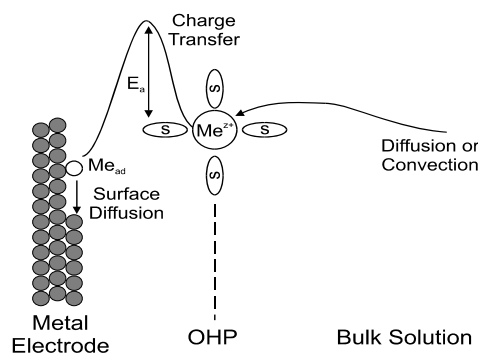


Figure 4. Schematic of the principal processes of the electrodeposition of a hydrated metal (Me) ion.

In the following the formation of metal nuclei (grains) will be shortly described. The term “grain” was used by Volmer to express the small primary parts that are generated in a phase transition system, in form of small drops or small crystallites. These grains can start to grow when the equilibrium between them (crystal phase) and the supersaturated ambient phase is disturbed [108]. Initially, Volmer considered the primary grains to have a spherical geometrical form. At the same time, other theories were developed (like that of Brandes) that considered in the beginning of the deposition a 2D grain to occur. Avrami [109] made a clear distinction between the terms “grain” and “nucleus”. After him, the term *nucleus* is connected to a *cluster of the new phase smaller than the critical size*, while the term *grain* refers to a *cluster larger than the critical size*. The critical size represents the dimensions that a growing formation (cluster) should have in order to grow.

Detailed overviews of the theories for three, two- and one- dimensional grain formation and growth were made by Fischer [110] and Budevski and co-workers [111].

How do the small particles (nuclei) form? The classical theory of Volmer stated that

these small particles, because of their surface tension, are less stable than the bulk phase. Thus, an energetic barrier should be passed for the formation of a small particle. When this happens, there will be a change in the free energy of the system (which is the total amount of energy that can be converted to do work). In the case of a spherical nucleus, its critical radius at which it starts to “exist” corresponds to the maximum of the free energy change. Volmer assumed that the probability for a nucleus with the critical radius to be born, is given by a Boltzmann expression ( $\exp(-W/kT)$ , where  $W$  is the fluctuation energy, or in other words, the free energy necessary to form a nucleus). Generally, the free energy change has two terms: one is given by the transferred number of atoms from the ambient phase into the crystal phase (volume free-energy, negative) and the second one is related to the new surface created of the crystallites (surface free-energy, positive). The nucleation process can occur at different rates (quickly or slowly), in function of the system (liquid in a gas, crystals in a liquid, etc) [112].

Kossel and Stranski introduced independently the notion of “kink site position”, named also “half crystal position” or growth site of the crystal [111,113]. In Fig. 5 the crystallization process of a crystal with cubic lattice is schematically presented, as described in the theory of Kossel and Stranski. There are three positions of atoms or ions on the crystal surface (substrate). They can be located in the lattice plane as ad-atoms or ad-ions (b). They can be in a crystal edge (step) (c) or in a kink position (d). The crystallization process can happen with different rates, due to the different path through which an atom/ion outside the crystal phase (a) will become incorporated in the crystal lattice. Thus, the process can happen as  $a \leftrightarrow b \leftrightarrow c \leftrightarrow d$ ,  $a \leftrightarrow c \leftrightarrow d$  or  $a \leftrightarrow d$  [113], in function of the activation energies of the partial steps and on the frequency of occurrence of these states.

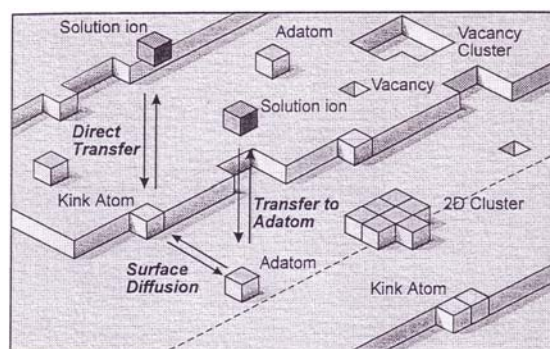


Figure 5. The crystallization process according to the theory of Kossel and Stranski. [111]

The kink site is the only site of the crystal that does not change after deposition or dissolution. It will be just shifted along the step by one atom, but the total number of kink sites will remain constant, as well as their properties.

### I.5.2 Classical Growth Models

The crystal growth process is given by the addition of atoms and molecules from the mother phase. In the pioneering literature one can find three growth models [111]: Volmer-Weber, Frank-van der Merve and Stranski-Krastanoff. The Volmer-Weber model predicts that the nucleation occurs in the shape of 3D islands rather than monolayers. These islands will grow independently and at one moment they can merge. This type of growth is specific when the binding energy between  $\text{Me}_{\text{ads}}$  and the foreign substrate, S, is lower than the binding energy of  $\text{Me}_{\text{ads}}$  on the native substrate, Me. The other two models describe the case when binding energy between  $\text{Me}_{\text{ads}}$  and the foreign substrate is larger than the binding energy of  $\text{Me}_{\text{ads}}$  on the native substrate. In comparison with the first model, they can predict also the formation of monolayers. When there is a small crystallographic Me-S misfit, the Frank-Van der Merve growth model is valid, while when there is a significant crystallographic Me-S misfit, the Stranski- Krastanoff model can be applied. The Frank-Van der Merve model predicts that the growth is layer by layer, thus epitaxial. The atoms can migrate across the surface to the edge. The Stranski- Krastanoff model predicts that the nucleation occurs as islands, but these are formed on top of few monolayers of the same deposited material.

The competition between nucleation and growth was proved to be very important for the morphology of the deposited layers. If the nucleation rate is higher, finer grains materials will be obtained. If the growth rate is higher, specific structure of the deposited layer can be generated (e.g. fibrous) [111].

### I.5.3 The Role of Overpotential in the Nucleation and Growth Processes

The frequency of forming new nuclei is given by the number of ad-atoms that are moving on the cathode surface. The latter depends on the flux of ions carried by the deposition current. Thus, the frequency of nucleation is influenced by the current density.

Many experimental methods were developed in order to understand the phase formation in electrochemical systems [111]. In early times, the relation between the overpotential and the kinetics of nucleation was done by direct microscopic observation of the electrode [108,114] or indirectly, by determining the current transients in function of the active area of the electrode, that was related to the total number of nuclei [115]. Recently, in situ STM and EQCM measurements were performed to determine with high accuracy the electrochemical

phase formation on the electrodes [116-118]. At the same time, many theoretical models were built to explain the kinetics of a phase change [109-125]. These models described the current transients in function of the number of nucleation sites ( $N_0$ ) and nucleation rate ( $A$ ) by different approaches. Some of them will be shortly described later, as they were chosen in this study for comparison with our experimental data (sections I.5.4, III.1.2.c).

With the help of a potentiostat, the nucleation process can be studied by three methods [124]. First, from linear sweep voltammetry one can get qualitative information about the occurrence of the nucleation process. Secondly, galvanostatic deposition can be also performed, in order to force the nucleation process to take place at a determined rate. In this case, the potential changes will be monitored during the nucleation process. Thirdly, potentiostatic depositions were largely used, where either a single or double potential pulse step was applied. The current transients can reveal information about the nucleation rate or about the number of nucleation sites. Potentiostatic deposition was the method chosen in the present study in order to identify the first steps of the Ni and Ni-Fe alloy deposition process.

The nuclei can grow parallel or/and perpendicular to the electrode surface. If the growth probability is equal in all three direction of the space, hemispheres will be formed. In fact, the recent theories describe the nuclei (mostly) as hemispherical entities randomly distributed on the electrode surface. Each individual nucleus is surrounded by a hemispherical diffusion zone (the *short time* behaviour). This is valid also for nuclei that have different geometrical form, because it was observed that the depletion zones around the growing nuclei advance in a radial way more quickly. When the nuclei grow, their diffusion zones will overlap. From this point, the growth of the mature nuclei cannot be considered to occur independently of each other. If the diffusion zones are large enough, then some planes in the vicinity of the electrode will be hindered for further nucleation. Now the deposition can occur only in a direction almost perpendicular to the electrode [125]. Thus, the growth of the deposit is controlled by linear diffusion to the electrode surface (the *long time* behaviour).

Two types of nucleation can be identified: instantaneous and progressive nucleation. In the instantaneous nucleation, an array of nuclei forms on the electrode surface, even if the critical value of the overvoltage (from the relation overvoltage- nucleation rate), is not reached yet. In the theoretical studies, the nuclei formed by instantaneous nucleation are considered to be born in the same moment and to grow at the same rates [125]. The progressive nucleation occurs above a critical overvoltage. In this case, the nuclei can appear in different moments of time and grow at different growth rates.

Another classification for the nucleation and growth processes distinguishes between two cases: *interfacial (or charge) controlled* and *diffusion controlled* [127]. The first one is favoured at high concentration of the electrolyte and low deposition overpotentials, and the second one characterizes the deposition from a low concentration electrolyte and high overpotentials. The limiting step for nuclei growth for the interfacial controlled growth is the rate with which a new phase incorporates in an old one. For the diffusion controlled growth the rate at which the ions are transported in the solution toward the electrode is the limiting step.

In the classical model proposed by Gruz and Volmer in 1931, the shape of the curves overpotential - current density during an electrodeposition depends mostly on the active surface of the cathode. This can change strongly during the deposition. At small overpotentials (small current densities) the ion concentration in the double layer is just slightly higher than the equilibrium one, established in the super-saturated state. Therefore, the deposition will occur not all over the electrode surface, but just in the active places. The further generation of new nuclei is suppressed and the crystal growth occurs. At higher overpotentials, the generation of new nuclei is accelerated. Thus, large grains are expected at low overpotentials and fine ones at higher overpotentials.

Plieth [128] showed that from the electrochemical expression of the Kelvin equation (Eq. 16), the critical radius of a spherical nucleus,  $r_{\text{crit}}$ , can be described to be inversely proportional to the overpotential,  $\eta$ , and thus to the current. As predicted also by the model of Gruz and Volmer, smaller and numerous particles are expected to appear at higher current densities.

$$r_{\text{crit}} = -\frac{2\gamma V_{\text{M}}}{zF\eta} \quad (\text{Eq. 16})$$

where  $\gamma$  is the surface energy and  $V_{\text{m}}$  is the molar volume.

When the diffusion fields around the growing nuclei overlap, the nucleation process will stop in these regions of the electrode. On longer time scales, nucleation will occur also in these regions, because of the onset of natural convection, which will disturb the diffusion zones.

## I.5.4 Theories for the Chronoamperometric Transients of Nucleation and Growth

As discussed above, different theories were elaborated to describe the current transients in function of the number of nucleation sites ( $N_0$ ) and nucleation rate ( $A$ ). Some of them were chosen for fitting our experimental data: the Scharifker-Hills model (SH) [125], Scharifker-Mostany (SM) [122], and Heerman-Tarallo model (HT) [121].

### I.5.4.a Scharifker-Hills model

Scharifker and Hills considered the nuclei to be hemispherical. For short deposition times, the diffusion zones will be hemispherical, but for long times the diffusive flux and growth current can be expressed in terms of semi-infinite linear diffusion. Normally, the nucleation is a complicated problem between 2D and 3D, as the nuclei grow first at the plane of the electrode surface, but later, they will grow also in the bulk electrolyte.

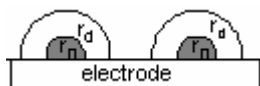


Figure 6. Schematic representation of two independent growth centres.  $r_0$  is the radius of the nuclei and  $r_d$  the radius of the hemispherical diffusion zones around the growth centres

Two independent growth centres that occur on the surface of the electrode are schematically represented in Fig. 6. The radius of the hemispherical diffusion zones ( $r_d$ ) around the nuclei is time dependent. This dependence is expressed differently by the different models.

Scharifker and Hills simplified the nucleation problem to a 2D problem by considering the equivalent area of plane surface towards which diffuses, by linear diffusion, the same amount of material that would be transferred through spherical diffusion to a growing centre. They introduced a constant,  $k$ , that characterizes the radial growth of a nucleus radius,  $r_d$ , in time ( $r_d(t) = (kDt)^{1/2}$ , with  $D$ - the diffusion coefficient). Thus, the planar area of  $N$  independently growing nuclei will be  $S(t) = N\pi r_d^2(t)$ .

According to Avrami's theorem, one can express the area ( $\theta$ ) on which new nuclei can appear in function of the extended area ( $\theta_{ext}$ ) via the following equation (Eq. 17):

$$\theta = 1 - \exp(-\theta_{ext}) \quad (\text{Eq. 17})$$

The extended area represents the theoretical fraction of area  $\theta$  that is nucleated if the overlap is ignored, thus, it will be the same as  $S(t)$ . In this way, Scharifker and Hills used the Avrami theorem in order to express radial diffusion zones as the equivalent diffusive flux on an electrode of area  $\theta$ . Conservation of mass requires that the material entering the diffusion zones must be equal to the amount incorporated in growing nuclei. Thus, taking this into account, the current density on the whole surface of the electrode can be calculated by integration for the two types of nucleation, progressive and instantaneous (Eq. 18):

$$I(t) = \frac{zFD^{1/2}c\theta(t)}{\pi^{1/2}t^{1/2}} \begin{cases} = NI_{1,t} \frac{zF\pi(2Dc)^{3/2}M^{1/2}Nt^{1/2}}{\rho^{1/2}}, & \text{for instantaneous nucleation} \\ = \frac{2zFAN_{\infty}\pi(2Dc)^{3/2}M^{1/2}t^{3/2}}{3\rho^{1/2}}, & \text{for progressive nucleation} \end{cases} \quad (\text{Eq. 18})$$

where  $I_{1,t}$  is the current needed by a single nucleus to grow,  $c$  is the concentration,  $\rho$  the density of the depositing species,  $M$  the molar mass of the depositing species,  $N_{\infty}$  the density number of active sites,  $A$  the nucleation rate per site. The left part of the Eq. 18 represents the current calculated from Cottrell's equation for planar diffusion with fractional coverage  $\theta$ .

Two different values were obtained for  $k$ , specific for the instantaneous and progressive nucleation. Normally, the obtained equations were used in an dimensionless form:  $(I/I_{\max})^2$  is plotted versus  $(t/t_{\max})$ , where  $I_{\max}$  represents the maximum current obtained in the potentiostatic transients at a specific moment in time,  $t_{\max}$  (Eq. 19).

$$\begin{aligned} \frac{I^2}{I_{\max}^2} &= \frac{1.9542}{t/t_{\max}} \{1 - \exp[-1.2564(t - t_{\max})]\}^2, & \text{instantaneous} \\ \frac{I^2}{I_{\max}^2} &= \frac{1.2254}{t/t_{\max}} \{1 - \exp[-2.3367(t - t_{\max})]\}^2, & \text{progressive} \end{aligned} \quad (\text{Eq. 19})$$

The values  $I_{\max}$  and  $t_{\max}$  can be evaluated from the condition that the first derivative of the  $I$ - $t$  relation is equal to zero ( $dI/dt=0$ ). The experimental curves can be then compared to those predicted by the theory. The disadvantage of this method is that the instantaneous and progressive nucleations are treated separately. Nevertheless, it is the method most largely used to compare experimental data obtained for different systems [127].

#### 1.5.4.b Scharifker-Mostany model

The improvement introduced by the SM model compared to the SH theory is that now

the two types of nucleation are treated together. The  $k$  values are considered to be the same for instantaneous and progressive nucleation and equal with the  $k$  value from the SH model for instantaneous nucleation.

As in the SH model, the expression for the total current results from the projection on the electrode surface of hemispherical diffusion zones towards a free hemispherical nucleus. Thus the approach to the problem of nucleation becomes 2D. Circular diffusion zones were obtained, whose radius will depend on the ages of the nucleation centres ( $t-u$ ). The age of a nucleus is given by the difference between the time that passed from the moment when the potential was applied ( $t$ ) and the moment when the nucleus was born ( $u$ ).

In the SM formulation, the diffusion zones born at different times grow at exactly the same rate. Another particularity of this model is that the heights of the diffusion cylinders grow immediately after their appearance.

The current transients obtained by the SM model can be compared to those given by Sluyters-Reybach (SRWBS) [123]. The only difference is the way the authors considered the evolution of the radius of diffusion zones in time [129].

$$I_{SM} = \left( \frac{zFD^{1/2}c}{\pi^{1/2}t^{1/2}} \right) \left( 1 - \exp \left\{ -N_0 \pi k D \left[ t - \frac{(1 - e^{-At})}{A} \right] \right\} \right), \text{ where } k = \left( \frac{8\pi cM}{\rho} \right)^{1/2} \quad (\text{Eq. 20})$$

The conclusion of Scharifker and Mostany [129] was that their model, similar to the Sluyters-Rehbach model, can describe accurately the instantaneous nucleation. Furthermore, the SM model (unlike the SRWBS model) can describe the progressive nucleation, too. However, both models fail to describe accurately an intermediate case. By an intermediate case one can define a nucleation which is not pure instantaneous (very large  $A$  and small  $N_0$ ) or pure progressive (very large  $N_0$  and very low  $A$ ). Another disadvantage is that the fitting of the experimental transients will look the same for different values of  $N_0$  and  $A$  [127].

### **I.5.4.c Heerman-Tarallo model**

Heerman and Tarallo compared the SM and SRWBS models, as they arrived to different expressions for current although they start from similar ideas. HT observed that the SRWBS model overestimates the fractional surface coverage and thus it will predict the position of the current maximum at too early times. By comparison, the SM model is correct for extended coverage.

The changes introduced by the HT model consist in expressing the current not via



Cottrell's equation with only time variable, but also in function of the thickness of the uniform diffusion layer in case of overlap,  $r_d$ . This parameter is calculated following the ideas of SRWBS: the height of all the diffusion cylinders is taken equal to the thickness of the Nernst diffusion layer for a simple redox reaction. Applying the Avrami's theorem, they could express the current density as dependent on time, on the nucleation rate,  $A$ , and on the nucleation site density,  $N_0$ .

The current in the HT model is expressed with the help of Dawson's integral ( $\Phi$ ), in the following form (Eq. 21):

$$i(t) = zFDc\alpha N_0 t^{1/2} \Phi = zFDc\alpha N_0 t^{1/2} \left[ 1 - \frac{e^{-At}}{(At)^{1/2}} \int_0^{(At)^{1/2}} e^{-\lambda^2} d\lambda \right] \quad (\text{Eq. 21})$$

In the Eq. 21  $\alpha$  is equal to  $2\pi(2MDc/\rho)^{1/2}$ . The Dawson's integral ( $\Phi = \Phi[(At)^{1/2}]$ ) is a tabulated function [121].

Later, Heerman et al. improved their model [130]. They suggested that the previous approach from the literature was not correct, even if the final expression of the current was accurate. The planar diffusion zones were described by Cottrell equation that implied a flux balance. In reality, this is not correct. Furthermore, they underlined that the concept of planar diffusion zone should be related to an ensemble of growing nuclei rather than to a single nucleus.



## II. Experimental Details

### II.1 Experimental Techniques

#### II.1.1 Electrochemical Quartz Crystal Microbalance (EQCM)

For the EQCM experiments 10 MHz optically polished AT-cut quartzes provided by KVG (Neckarbischofsheim, Germany) were used. They had two gold electrodes, of 100nm thickness, deposited on the opposite faces of a quartz crystal, on a 5-10nm adhesion layer of chromium. These quartzes are approximately 15mm in diameter and 165 $\mu$ m thick.

The resonance frequency of the quartz was measured with a Maxtek PLO-10 (Phase Lock Oscillator, Santa Fe Springs, USA) and a frequency counter card (GT200, Guide Technologies). The PLO circuit also provides information about the damping of the quartz as a voltage, which was acquired with a Keithley DMM and converted to the motional resistance,  $R_m$ , of the quartz.

There are three main parts in a PLO device: an internal oscillator, referred as Voltage Control Oscillator (VCO), used to drive the quartz crystal, a phase detector, which continuously monitors the phase difference between the crystal's current and voltage, and an integrator, which accumulates the phase error. The output of the phase detector is fed into the integrator and the integrator output is connected to the VCO. Imagine that the VCO frequency is initially smaller than the resonance frequency of the quartz crystal. Thus, a positive phase between the current and the potential of the crystal will occur that will induce a positive output at the phase detector. This causes the integrator output to increase, which causes the frequency of the VCO to increase. If the new resonant frequency of the VCO is the same as the resonance frequency of the quartz crystal, then the phase between the current and the potential will become null and the integrator output will hold steady [131].

An alternative EQCM set-up consisted of an Advantest R3753BH network analyzer (Advantest, Tokyo, Japan) in the reflection mode. A network analyzer (NA) is a device for analyzing the properties of electrical networks. These properties are associated with the reflection and transmission of electrical signals, and are quantified in the scattering parameters,  $S$  [132]. The NA can measure the incident, reflected and the transmitted signal. There are four main parts in a NA: a source, which supplies the stimulus for the system and which can be a VCO, devices for separation the signals (splitters or directional couplers), which separate the incident and the reflected signals, receivers that detect the signals (diode

detectors) and a display of the results [132].

The NA records the admittance spectra of the resonator near its resonance frequency. Each admittance spectrum was transferred to a computer via a GPIB card and then fitted with a Lorentzian [46, 47]. The connection between the electrochemical cell and the network analyzer was made by a pi network adapter (TeleQuarz, Neckarbischofsheim, Germany) and a LC network (capacity  $C=0.1\mu\text{F}$ , inductance,  $L=1\text{mH}$ ) to decouple the high and the low frequency signals of the quartz and the electrochemistry, respectively. Details can be found in [46, 47].

Like the PLO, the NA provides information on the resonance frequency of the quartz crystal and on its damping. However, with the NA the damping of the quartz is expressed as the value of the full width at half maximum (FWHM) of the resonance curve.

### II.1.2 Vibrating Sample Magnetometer (VSM)

The Vibrating Sample Magnetometer (VSM) is used to measure the magnetic properties of materials. Normally, a sample, magnetized by a homogeneous magnetic field created by an electromagnet, is made to vibrate [90]. The vibration can be a sinusoidal motion on the vertical axis, for example. The magnetic dipole moment of the magnetized sample will create a magnetic field around the sample. As the sample is moved up and down, this magnetic field will change in function of time. According to the Faraday's law, the resulting field change will induce an electric current, thus an induced voltage will appear in a set of pick-up coils. This voltage is proportional to the magnetic moment of the sample.

Usually, a measurement takes place as follows: first, the strength of the constant magnetic field is fixed. Then, the sample starts to vibrate. The signal received from the pick-up coils is translated into the value of the magnetic moment of the sample by the computer. The strength of the magnetic field is changed to a new value and the new corresponding magnetic moment is calculated. Finally, hysteresis loops, which are the plots of the magnetization ( $M$ ) in function of the applied magnetic field ( $H$ ), are generated.

Using a vibrating sample magnetometer one can determine from the hysteresis loops the magnetization of saturation ( $M_s$ ), that represents the maximum moment measured, the coercivity ( $H_c$ ), that is the field required to reduce a saturated sample to zero induction, the magnetic susceptibility of the sample or its anisotropy. The magnetic susceptibility is defined as the slope  $dM/dH$  at  $H_c$ . The anisotropy (defined in section I.3.2) can be observed

from the way the magnetization curves vary with the angle of the sample.

For the characterization of the magnetic properties of the layers, thin nickel layers (ca. 3-5 $\mu\text{m}$ ) were deposited at  $-3.5\text{mA cm}^{-2}$  onto cylindrical copper electrodes (diameter 6mm, height 6mm). Hysteresis curves (-1.0 to 1.0T) were recorded with a vibrating sample magnetometer (VSM, model 7300, Lake Shore, Ohio, USA). The H field could be applied parallel (in the following called  $0^\circ$  position) and normal ( $90^\circ$ ) to the plane of growth. Furthermore, the sample could be rotated in the H field to check for anisotropies.

### II.1.3 Atomic Force Microscopy (AFM)

Atomic Force Microscopy (AFM) is an imaging technique that can be applied for conducting and non-conducting samples. AFM functionality is based on the interaction between a flexible cantilever (with a low spring constant) and the atoms of a sample (Fig. 7). A very thin tip (around 2 nm diameter) is fixed at the end of the cantilever. Between this tip and the sample, interaction forces exist that are smaller than the interatomic forces. Thus, by moving this tip across the surface of the sample one can measure its topography, roughness, its adhesion properties, viscoelasticity, etc [133], without displacing the atoms of the sample.

There are three major components in an AFM device: the computer workstation, a controller, (which contains the electronics needed in order to allow the workstation to control the microscope and to record the image data), and the microscope [133]. A schematic representation of the microscope is given in Fig. 7. All the scanning probe microscopes operate in the same manner: a piezoelectric scanner performs high resolution raster scan in the x-y plane and a sensing and feedback system operates in the z axis, reporting and controlling the variation in height across the sample. A laser beam is focused on the upper part of the tip. The reflected beam falls on a mirror and then is again reflected to a photodetector (which contains usually four photodiodes). When the cantilever interacts with the surface of the sample, it will be deflected. Thus the reflected laser will fall on another position on the photodiodes and a differential signal between the top and the bottom photodiodes will be generated. This data will be displayed as the deflection image. At the same time, the changes in the piezo height which are needed to keep constant the cantilever deflection signal are displayed in the height image (topography image).

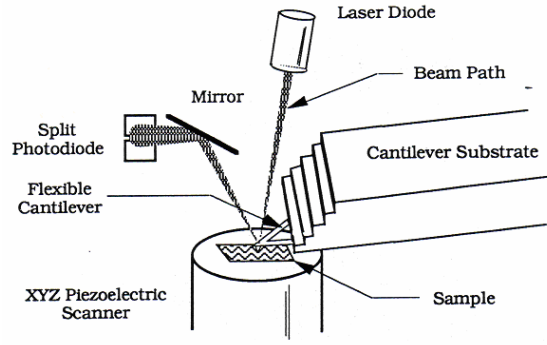


Figure 7. AFM optical sensing system from [133].

The topography of the deposited layers and the roughness were investigated with a contact mode AFM (atomic force microscopy, PicoSPM, Molecular Imaging, Phoenix, USA), using triangular cantilevers with sharpened pyramidal tip, made of silicon nitride (Olympus Corporation, Tokyo, Japan). The maximum scan size in the x-y plane that could be performed was  $6.6\mu\text{m} \times 6.6\mu\text{m}$ . Scan rates from  $0.5 - 2\text{Hz s}^{-1}$  were used. A planefit was performed off-line for the height images in order to remove the tilt or bow parts from images. The planefit calculates a single polynomial fit for the entire image and then subtracts this polynomial fit from the image.

Two surface roughness parameters of the deposited layers were calculated with the DI (Digital Instruments) software. They are based on (Eq. 22).

$$R_q = \sqrt{\frac{\sum (Z_i - Z_{ave})^2}{N}}; \quad R_a = \frac{1}{L_x L_y} \int_0^{L_y} \int_0^{L_x} |f(x, y)| dx dy \quad (\text{Eq. 22})$$

where  $R_q$  is the standard deviation of the Z values within the given area, calculated from the topography image (the height),  $Z_i$  is the current Z value,  $Z_{ave}$ - the average of Z values within the given area and N- number of points from the given area.  $R_a$  is the mean roughness,  $L_x$ ,  $L_y$  are the dimension of the surface, and  $f(x,y)$  give the relative surface to the central plane (0).

Furthermore, the DI software was used to determine the grain size and the number of the particles within a given scan size (see section III.1.3).

### II.1.4 Scanning Electron Microscopy (SEM)

Scanning Electron Microscopy is a technique for imaging surface morphology. Basically, SEM instruments consists in an electron source (electron gun), magnetic lenses

for focusing the electron beam, a detector for the secondary electrons emitted by a bombarded specimen and a monitor where the image produced by the secondary electrons is displayed. Detailed description of the SEM can be found in [134,135].

In the present study a SEM model DSM 982 Gemini from Zeiss Oberkochen, Germany, was used.

### **II.1.5 Energy Dispersive X-Ray (EDX)**

The EDX detector is usually incorporated in the SEM device, because whenever an electron beam interacts with matter, as it happens in SEM, X-rays are produced. A semi-conducting crystal, usually a silicon single crystal doped with impurities of lithium and boron, is used as detector in the EDX analysis. The X-rays hit the semi-conducting crystal and give up their energy by collision events [136]. The electrons of the semiconductor will jump from the valence band into the conduction band. Electron-hole pairs will be formed. They will be forced to migrate in opposite direction by applying a high potential on the contacts of the crystal (which are in front and in the back), thus a current pulse is formed. Each electron-hole pair has its characteristic creation energy. Thus by measuring the current pulse produced one can determine the energy of the incident X-rays and can identify the chemical element that produced them. This is possible because whenever an electronic transition occurs in one element, the energy released will be unique.

The EDX analyses were performed with an EDX model Voyager III 3200, from SUS Pioneer in order to get information about the chemical composition of the deposited layers. Usually, the EDX analyses were performed for every sample at two magnifications: 1000x and 10000x. Line analysis and mapping of the deposited layers were also performed for some representative Ni-Fe layers.

The SEM and EDX analysis were performed by Ms. Ellen Kern (TU Dresden, Institute of Physical Chemistry and Electrochemistry).

### **II.1.6 X-Ray Diffractometer (XRD)**

The X-Ray Diffractometer consists from a source of X-rays (a X-ray tube, for example), an X-ray detector, a goniometer, which provides precise mechanical motions of the tube, sample and detector, and the electronics for counting detector pulses in synchronization with

the positions of the goniometer [137].

In the following the principle of functionality of a XRD will be shortly described. From the X-ray source a beam of X-rays that are parallel and with the same wavelength will be guided through some collimators to the sample plane. A small part of the incident X-ray will be reflected on the surface plane (Fig. 8). Other part of the X-ray beam will be reflected by atoms that are in a different plane. Thus, a constructive or a destructive interference of the reflected radiation can occur, in function of the direction of the waves. Minimum and maximum of intensity will result from the interference of the waves along the different directions. The maximum intensities are obtained when the Bragg's law is fulfilled (Eq. 23, [138]).

$$n\lambda = 2d \sin\theta \quad (\text{Eq. 23})$$

where  $n$  is an integer,  $\lambda$  the wavelength of the X-ray and  $d$  is the distance between two lattice planes. If  $\lambda$  and  $n$  are known, one can calculate the interplanar spacing ( $d$ ) by measuring the  $\theta$  angles.

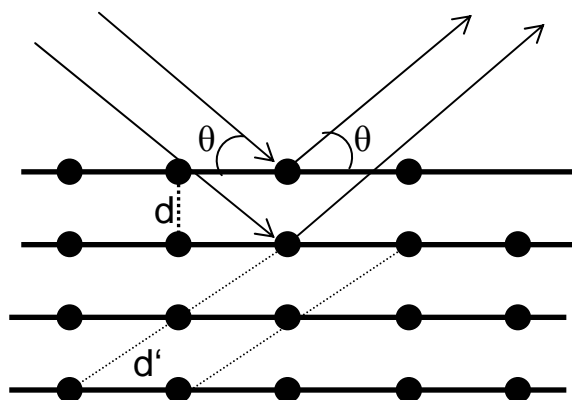


Figure 8. A schematic representation of a crystalline lattice. The arrows indicate the directions of the incident and reflected X-Ray beam.

A detector, (which can be a scintillator, silicon or germanium diodes, etc) will convert the energy of the reflected X-ray beam into voltage pulses. Detailed descriptions of the different types of detectors and their principle of operation can be found in [137,139]. Precise movements of the sample and of the detector with respect to the X-ray source are made by a goniometer. In practice it is easiest to keep the source fixed and to rotate the sample holder by an angular velocity,  $\theta$ /second. In order to detect the radiation reflected at the angle  $\theta$ , the detector must rotate by  $2\theta$ /second. The orientation of the sample, position of the detector and the counting of the reflected radiations are usually all computer controlled.

The XRD data obtained are called diffraction pattern or diffractogram and are in fact



graphics of the counts measured by the detector versus the  $2\theta$  angle. Normally, a diffraction pattern contains many distinct peaks, each corresponding to a different interplanar spacing,  $d$ . For example, for a cubic crystal with the lattice parameter  $a$ , the interplanar spacing  $d$  of different planes indexed by Miller indices  $(hkl)$  can be expressed:  $d=a/(h^2+k^2+l^2)^{1/2}$  [137]. In practice, the positions and the intensities of the peaks in a measured diffraction pattern are compared to the peaks from a standard sample or from calculation. Thus, using the Miller indices,  $(hkl)$ , the different peaks in a diffraction pattern are indexed [139].

The XRD measurements were performed by Ms. Anja Bensch (TU Dresden, Institute for Inorganic Chemistry)) at room temperature with a Siemens D500 X-Ray Diffractometer (Freiberg, Germany) in reflection mode. The X-Ray source had the wavelength  $\lambda=1.54060\text{\AA}$  (Cu  $K_\alpha$  radiation). Samples were rotated (in the maximal range) from  $10^\circ$  to  $120^\circ$  (the  $2\theta$  angle) with a step size of  $0.01$  or  $0.02^\circ$ . Long time measurements (more than 10 hours) were done with the X-Ray Diffractometer in order to get a better signal/noise ratio.

## **II.2 Experimental Set-up and Electrolytes**

The quartz crystal was placed at one end of the cell, and fixed between an o-ring (Viton, solution side) and a silicone gasket (air side). It could be fixed in the electrochemical cell vertical, parallel to the gravity force, or horizontal, perpendicular to the gravity (Fig. 9).

One gold electrode evaporated on a quartz substrate was used as the working electrode (WE). The effective area of the WE was around  $0.22\text{cm}^2$ , but after each measurement it was accurately determined from a digital photography by using an imaging software. The counter electrode was a Platinum foil of approximately  $3.7\text{cm}^2$  and  $0.2\text{mm}$  thickness or a Ni disc of  $2\text{cm}$  diameter and  $2.5\text{mm}$  thickness, placed in parallel to the working electrode. The distance between the working and the counter electrode was approximately  $1.5\text{cm}$  when the WE was horizontal and  $2\text{cm}$  when the WE was vertical. The Ni disc was used as counter electrode just for the Ni depositions from sulfamate bath. Three kinds of reference electrodes were used: a lab-made  $\text{Hg}/\text{Hg}_2\text{Cl}_2$ , a commercial “double junction”  $\text{Ag}/\text{AgCl}$  (Metrohm, Germany) and a Saturated Calomel Electrode (SCE, Sensortechnik Meinsberg GmbH, Meinsberg, Germany).

The electrochemical cells were home made from Teflon. The cell in which the WE was horizontal, was a cylindrical one ( $3.6\text{cm}$  inner diameter and  $4.2\text{cm}$  height), while the cell in which the WE was vertical, was rectangular (external dimensions:  $4\times 4\times 6\text{ cm}^3$ ).

The electrochemical experiments were made with a Potentiostat/Galvanostat Model 263A (EG&G Instruments, Princeton, NJ, USA). The whole setup was controlled by lab-made software (Microsoft Visual C++).

A water-cooled electromagnet from VEB Polytechnik, Phylatex, Chemnitz, was used to produce the magnetic field. The maximum flux density was 740mT for a gap of 46mm. The intensity of the magnetic field was measured with a Hall probe (Lake Shore, model 450).

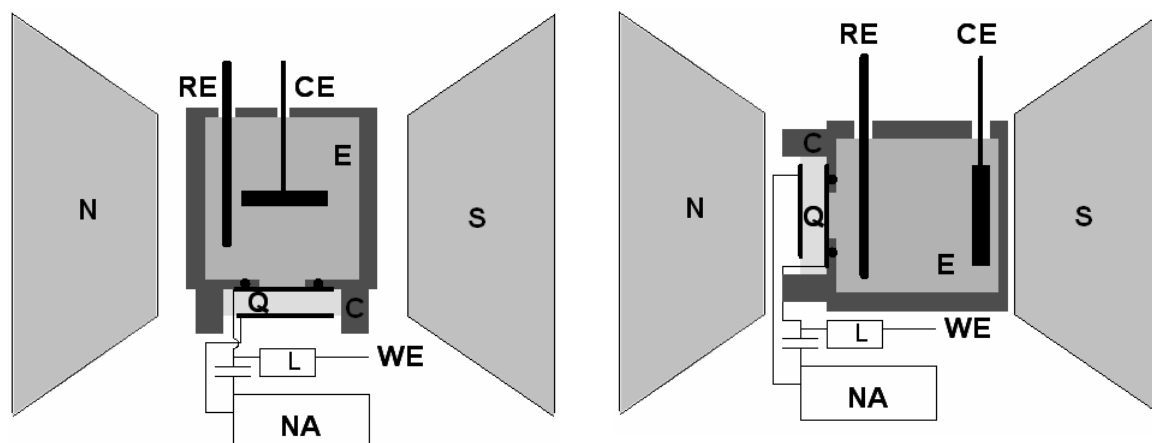


Figure 9. Schematic representation of the experimental set-up. N, S define the poles of the electromagnet, C the electrochemical cell, Q the quartz crystal, E the electrolyte, WE is the working electrode (Au), CE the counter electrode (Pt or Ni), RE the reference electrode and NA the Network Analyzer.

For the vertical working electrode, four possible orientations were studied (Fig. 10): (A) – when the Lorentz force was antiparallel to the natural convection (NC), (B)- when the Lorentz force was parallel to NC, (C) – when the magnetic field lines were antiparallel to the electric current and (D) – when the magnetic field lines were parallel to the electric current. In the case of the horizontal electrode (orientation E) the magnetic field lines were all the time perpendicular to the electric current.

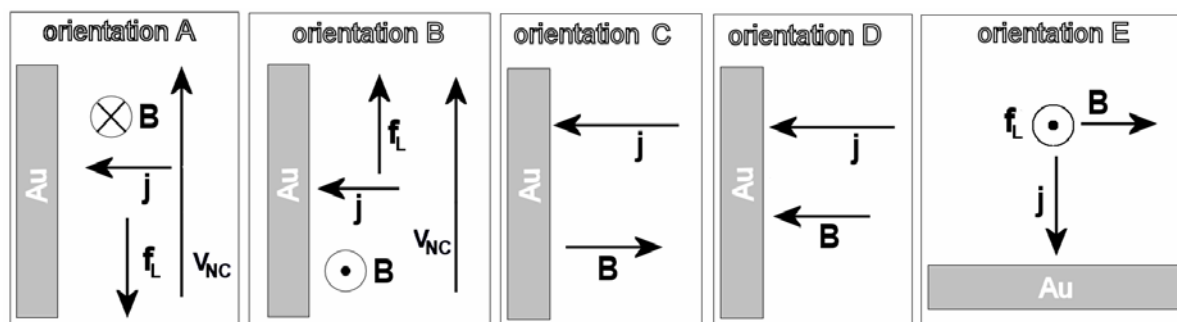


Figure 10. Possible orientations of the working electrode with regard to the magnetic field  
Most of the Ni electrodeposition experiments were performed from two types of

electrolytes:

- a sulfate bath, 0.01M NiSO<sub>4</sub>+0.1M Na<sub>2</sub>SO<sub>4</sub> pH=3, adjusted with H<sub>2</sub>SO<sub>4</sub>
- a sulfamate bath, 1.26M Ni(SO<sub>3</sub>NH<sub>2</sub>)<sub>2</sub>\*4H<sub>2</sub>O+0.32M H<sub>3</sub>BO<sub>3</sub>+0.04M NiCl<sub>2</sub>\*6H<sub>2</sub>O, pH=4.

The dilute sulfate electrolyte (0.01M NiSO<sub>4</sub>+0.1M Na<sub>2</sub>SO<sub>4</sub>) was chosen in order to work under mass transport limitation for the electroactive species and in order to study the nucleation of Ni on the gold substrate.

In the case of the sulfamate bath the pH was adjusted to 4 by adding sulfamic acid (HSO<sub>3</sub>NH<sub>2</sub>) or nickel carbonate (NiCO<sub>3</sub>), and the influence of two types of surfactants (0.52mM SDS (Na dodecylsulfate, HO<sub>3</sub>SO- (CH<sub>2</sub>)<sub>11</sub>-Na) or 0.24mM sodium 2-ethylhexyl sulfate, C<sub>8</sub>H<sub>18</sub>NaO<sub>4</sub>S, called also sulfirol 8) on the HER and on the properties of the deposited layers was studied, too. Usually SDS is used as a wetting agent in bright Ni electroplating, to reduce or eliminate pinhole formation in the Ni layers due to hydrogen bubbles [140]. Sulfirol 8 is also a wetting agent that is used in the case of strongly agitated baths, in order to reduce the foam formation which is typical for most surfactants [140].

Two other electrolytes (1M NiCl<sub>2</sub>\*6H<sub>2</sub>O+3.2M HCl, pH≈0 and 0.9M Ni<sub>2</sub>SO<sub>4</sub>\*6H<sub>2</sub>O+0.2M NiCl<sub>2</sub>\*6H<sub>2</sub>O+0.48M H<sub>3</sub>BO<sub>3</sub>) were used just for some experiments.

Table 1. The electrolytic baths used to characterize the Ni-Fe alloy co-deposition

bath	NiSO <sub>4</sub> •6H <sub>2</sub> O	FeSO <sub>4</sub> •7H <sub>2</sub> O	H <sub>3</sub> BO <sub>3</sub>	pH
1	0.5M	-	0.4M	2-3
2	-	0.07M	0.4M	2
3	0.5M	0.07M	0.4M	2
4	0.5M	0.01M	0.4M	2-3

Prior to Ni-Fe alloy co-deposition, an electrolyte containing 0.5M MgSO<sub>4</sub> and 0.4M H<sub>3</sub>BO<sub>3</sub> was used to identify the region where the HER and oxygen evolution occur: Three pH values were investigated for this bath: 4.38 (the initial value), and then its value was adjusted to the value 3 and 2 by adding concentrated H<sub>2</sub>SO<sub>4</sub>. In Table 1 are summarized the electrolytes used for the study of Ni-Fe alloys codeposition.

Furthermore, two electrolytes for the electrodeposition of the Ni-Fe alloy investigated did not provide the expected results.

- *electrolyte (A)*: 0.45M NiSO<sub>4</sub>\*6H<sub>2</sub>O + 0.13M FeSO<sub>4</sub>\*7H<sub>2</sub>O + 0.08M Na citrate + 0.6M Na<sub>2</sub>SO<sub>4</sub> + 0.5M H<sub>3</sub>BO<sub>3</sub> + 0.01M saccharin + 0.63mM SDS, pH=2.6, room

temperature [141]

- *electrolyte (B)*: 0.06M  $\text{NiSO}_4 \cdot 6\text{H}_2\text{O}$  + 0.16M  $\text{NiCl}_2 \cdot 6\text{H}_2\text{O}$  + 6.4mM  $\text{FeSO}_4 \cdot 7\text{H}_2\text{O}$  + 0.40M  $\text{H}_3\text{BO}_3$  + 5.6mM saccharin + 0.9 mM SDS, pH=2.5 [142]

The layers electrodeposited from the electrolyte (A) proved to be very non-homogenous (Fig. 11). The Fe content of the layers deposited with the same conditions varied strongly from one sample to the other and often even within the same sample (25at% in some regions and 80at% in other regions). Furthermore, due to the high internal stress, the layers cracked often. The color of the deposited layer was silver in some regions, and dark-black in others. The different composition in different points of the electrodeposited Ni-Fe layers was persisting even if an additional mechanical stirring of the electrolyte (750rpm) and external magnetic field (0.6T,  $B \perp E$ ) were superimposed.

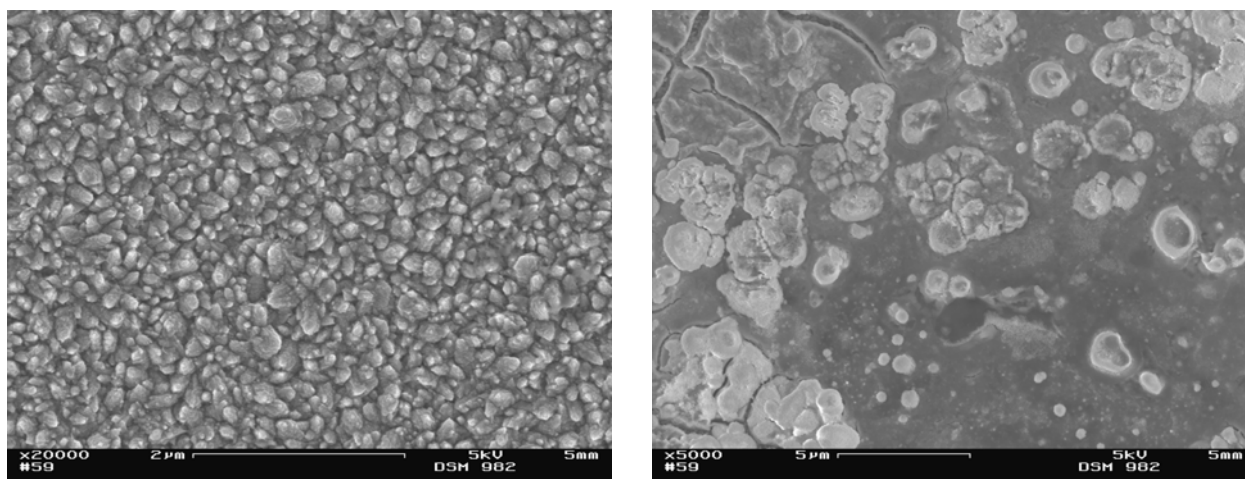


Figure 11. Examples of two layers deposited from electrolyte (A) at  $15 \text{ mA cm}^{-2}$  for 300s in  $B=0\text{T}$ .

The electrolyte (B) was made on the basis of the Ref. [142]. There, the authors claimed that they obtained with this bath a Fe-80% Ni alloy, of 705nm thickness, electrodeposited around room temperature ( $26^\circ\text{C}$ ), which had a coercive force of 0.25Oe. The current density that they used was  $15 \text{ mA cm}^{-2}$ . Using their experimental conditions, we obtained layers of just 5at%Fe. Therefore, the electrolytes (A) and (B) were abandoned for further study of the magnetic field effects in Ni-Fe alloy co-deposition.

All solutions were prepared from p.a. grade chemicals and bidistilled water. Some measurements were made at room temperature and some were performed at higher temperature ( $38^\circ\text{C}$ ,  $50^\circ\text{C}$ ), in a thermostated cell. In the case of the Ni-Fe alloy electrodeposition, the electrolytic bath was purged with Ar minimum 15 minutes before each measurement as well as during the measurements. The pH of the electrolytic baths for Ni-Fe

alloy co-deposition was adjusted by adding H<sub>2</sub>SO<sub>4</sub>.

Between three and ten samples were prepared for each experimental condition in order to assure the reproducibility.

### Calculation of the Partial Currents in Ni and Ni-Fe Alloy co-deposition.

The mass deposited on the quartz surface is given by Sauerbrey's equation (Eq. 7). From differentiating this mass deposited in time on a specific area and using the Faraday's law (Eq. 24) one can get the partial current due to Ni, respectively Ni-Fe alloy deposition.

$$\frac{dm}{dt} = \frac{M \cdot j}{zF} \quad (\text{Eq. 24})$$

In the case of the Ni-Fe alloys the molar mass for each sample was calculated based on the EDX analysis. The current density data obtained were smoothed with a second order polynomial function, using a Savitzky-Golay-like filter method. The Savitzky-Golay filter method essentially performs a local polynomial regression to determine the smoothed value for each data point. The Savitzky-Golay method was slightly modified in order to find the best smoothed value in one point, by considering five points before the point of interest and five points after it.

The partial current due to HER was obtained by subtracting the partial current of Ni (or Ni-Fe alloy) from the total current applied.

### Evaluation of the Current Efficiency

The ratio of the measured (Eq. 7) and the calculated (Eq. 24) deposition rate is called current efficiency,  $\eta$  (Eq. 25), and is an important parameter for technical applications. For obvious reasons one is interested in high current efficiencies in most cases.

$$\eta = \frac{j_{Ni}}{j_{Ni} + j_{HER}} = \frac{(dm/dt)_{meas}}{(dm/dt)_{calc}} \quad (\text{Eq. 25})$$

Equation 25 is expressed for the case of Ni electrodeposition, ( $j_{Ni}$  and  $j_{HER}$  are the partial current densities of the nickel reduction and the HER, respectively). A similar form can be written for the alloy electrodeposition.

### III. Ni Electrodeposition

This section is dedicated to Ni electrodeposition from sulfate and sulfamate baths. Nucleation and growth of Ni layers under a superimposed magnetic field will be discussed (III.1). Furthermore, the effects of a magnetic field on the current efficiency, partial current due to hydrogen evolution reaction (see III.2.2, p.69), current/potential transients (see III.1.2.a, p.48 and III.2.3, p.73), deposited mass (see III.1.2.b, p.53) and morphology of Ni layers (see III.1.3, p.61 and III.2.4, p.74) will be presented. XRD investigations (III.2.1, p.66) and the magnetic properties of the Ni layers electrodeposited from sulfamate electrolytes (III.2.5, p.84) will be also discussed.

#### **III.1 Nucleation and Growth of Ni: Bath with 0.01M Ni**

##### **III.1.1 Cyclic Voltammetry Analysis**

A set of cyclic voltammograms was performed at different scan rates: 50, 20, 5 and 1mV s<sup>-1</sup>. The Randles-Sevcik equation (Eq. 26) can be applied in order to check if the deposition is diffusion controlled. This relation predicts a linear dependence of the cathodic peak intensity to the square root of the sweep rate of the potential (Eq. 26):

$$I_p = 0.4463zFAc\sqrt{\frac{zFvD}{RT}} \quad (\text{Eq. 26})$$

where  $z$  is the number of electrons that appears in the electrochemical reaction,  $F$  is the Faraday constant,  $A$  the active area of the deposition,  $c$  the concentration,  $v$  the scan rate,  $D$  the diffusion coefficient,  $R$  the universal gas constant and  $T$  the temperature. This relation is valid for reversible systems [143], but a similar relation can be deduced for the totally irreversible processes with one-step reaction. Equation 26 was applied in the case of Ni deposition from a dilute electrolyte. In Fig. 12 the deposition rate of Ni, calculated from the EQCM data in function of the square root of the scan rate is plotted. The deposition rate was calculated from the mass vs. time curves. For every cycle of the cyclic voltammograms the slope in the region of the cathodic deposition was calculated. The average of these slopes was then calculated, and the standard error from the mean value was calculated. The procedure was repeated for some independent cyclic voltammograms executed at the same scan rate. The average value that resulted from all the measurements is shown in Fig. 12

(black points). The error bar is given by the standard error. The theoretical values (grey points in Fig. 12) predicted by the Eq. 26 are given for comparison with the experimental data obtained. The error between the experimental and the theoretical values is relatively low at small scan rates (1-5% for 1 and  $5\text{mV s}^{-1}$ ) and quite large at higher scan rates (10-40% at 20 and  $50\text{mV s}^{-1}$ ). For the following discussion the cyclic voltammograms made at  $5\text{mV s}^{-1}$  were chosen as representative.

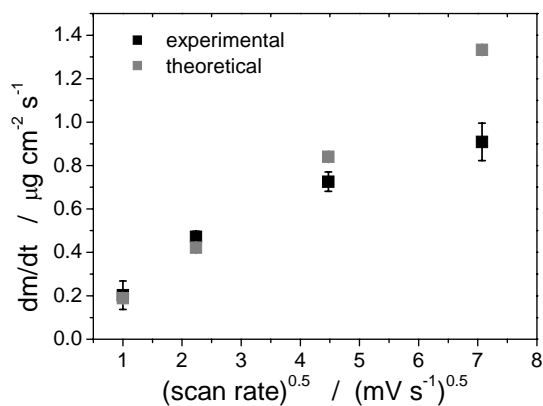


Figure 12. The deposition rate for nickel in function of the square root of the scan rate. Electrolyte used:  $0.01\text{M NiSO}_4 \cdot 6\text{H}_2\text{O} + 0.1\text{M Na}_2\text{SO}_4$ ,  $\text{pH}=3$ . Black points are the experimental data obtained in  $B=0\text{T}$  and the grey points are the theoretical ones (Eq. 26).

The cyclic voltammograms were performed in order to find the region where the Ni deposition starts. In Fig. 13 the frequency change of the quartz crystal and the corresponding deposition rate variation in function of the applied potential are plotted. In the potential range from the OCP until around  $-0.7\text{V}$  vs. SCE, the frequency increases by approximately 50-150Hz, which corresponds to an apparent decrease in mass of  $0.2 - 0.65 \mu\text{g cm}^{-2}$ . This frequency increase can be attributed to changes in the electrolyte viscosity in the vicinity of the electrode [144] or to desorption of the previously adsorbed sulfate on the gold substrate [117]. Tsionsky, Daikhin and Gileadi [144] pointed out that the viscosity changes can appear from two causes, which can be expressed on the basis of Gouy-Chapman theory. According to this theory, the field strength in the outer Helmholtz plane even if it is smaller than the field in the inner Helmholtz plane, can be still high enough to affect the structure of the solvent and change its local viscosity. On the other hand, one can calculate from the Gouy-Chapman theory the concentration of the ions near the electrode surface for an applied potential and a given bulk concentration. This calculated concentration of the active species can be one or two orders of magnitude higher than in the bulk of the solution, so that the

viscosity at the outer Helmholtz plane will change.

The nickel deposition sets in at around  $-0.9\text{V}$  vs. SCE. Not all the deposited nickel layer dissolves in the anodic scan. This can be easily seen in the frequency behaviour. The frequency does not come back to its initial value after the anodic scan. This happens because the nickel layer passivates very quickly during an anodic scan. That means that a thin passive layer (usually,  $\text{NiO}$  or  $\text{NiO}_2$ ) will be formed on the surface, which will reduce the dissolution rate (corrosion rate) of the nickel layer [16].

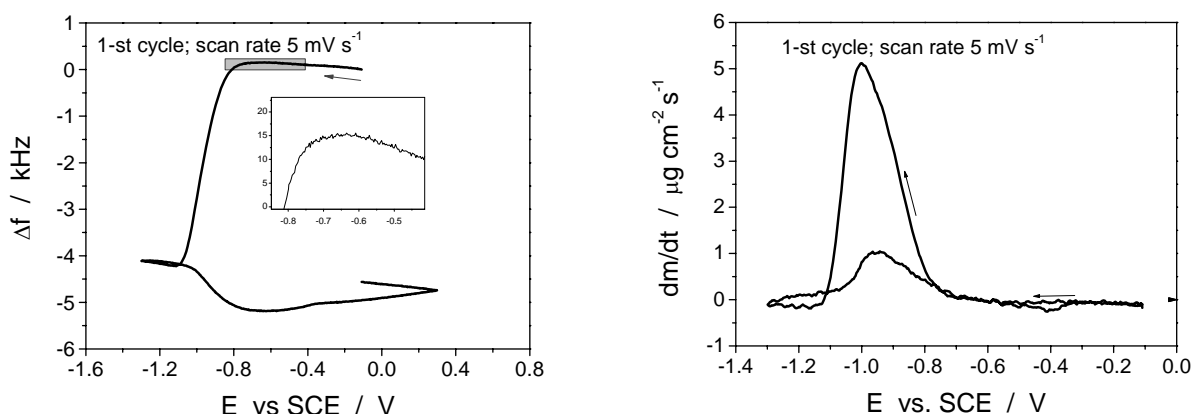


Figure 13. The frequency change of the quartz crystal and the corresponding mass variation during a cyclic voltammogram at a scan rate of  $5\text{ mV s}^{-1}$  from  $0.01\text{M NiSO}_4 \cdot 6\text{H}_2\text{O}$  +  $0.1\text{M Na}_2\text{SO}_4$ ,  $\text{pH}=3$ ,  $B=0\text{T}$ .

In Fig. 14 one can see a typical cyclic voltammogram obtained for the low concentration Ni electrolyte at a scan rate of  $5\text{ mV s}^{-1}$ . The Figs. 13 and 14 were obtained for different experiments, but with the same experimental conditions. It is obvious that after the first anodic scan, the intensity of the dissolution peak decreases significantly. In the cathodic scan two peaks can be observed: one around  $-0.7\text{V}$  vs. SCE and one at around  $-1\text{V}$  vs. SCE. The first peak appears in a potential region where hydrogen evolution occurs (this being proved easily by the mass variation in function of the applied potential diagram). It was underlined that the presence of this first peak reflects the presence of some inhibiting species [145]. The second peak is in a potential region where Ni deposition and hydrogen evolution reaction (HER) are present in parallel. In the literature this peak together with the two shoulders of the dissolution peak were considered to prove that there are two nucleation mechanisms for the Ni deposition [145,146]. According to Fleischmann and Saraby-Reintjes [146], a freshly deposited nickel layer is a mixture of its hydrogen alloys:  $\alpha\text{-Ni}$  (that represents a solid



solution of H in Ni which will dissolve at more anodic potentials) and  $\beta$ -Ni (that is an interstitial hydrogen-rich alloy with nickel, which will dissolve firstly, at more cathodic potentials). The  $\beta$ -Ni phase is very instable at normal temperature and pressures, thus it will convert easily into the  $\alpha$ -Ni phase ( $H/Ni= 0.03$ )

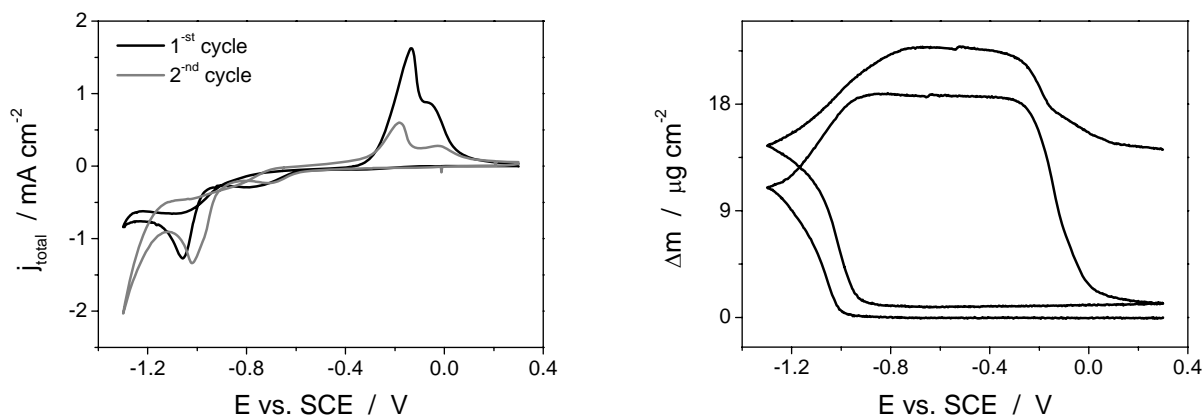


Figure 14. Left: a typical cyclic voltammogram made at a scan rate of  $5 \text{ mV s}^{-1}$ . Electrolyte used:  $0.01\text{M NiSO}_4 \cdot 6\text{H}_2\text{O} + 0.1\text{M Na}_2\text{SO}_4$ ,  $\text{pH}=3$ . No magnetic field was superimposed. Right: the deposited mass in function of the applied potential calculated from the EQCM data

At potentials more negative than  $-1.2\text{V vs. SCE}$  the water decomposition occurs. This reaction implies the occurrence of hydrogen bubbles and of the  $\text{OH}^-$  species on the cathode surface. As a consequence, metal hydroxides can be formed that can precipitate on the electrode and together with the hydrogen bubbles will block the electrode surface and inhibit further depositions [147,148]. Therefore the deposited mass will remain almost constant for some time. After more than three cycles, a decrease in mass was recorded in this potential region. As the nickel layer does not dissolve completely, the deposit will become rougher in time. After three cycles maybe the roughness of the layer is so high, that some liquid will be trapped between the clusters and it will appear in the EQCM signal as an additional mass. When the water decomposition takes place, part of this additional mass will disappear due to hydrogen bubbles that will detach, thus the frequency of the quartz crystal will increase.

Going back in the anodic direction, the deposition continues till approximately  $-0.9\text{V}$ , after which the mass decreases slowly till  $-0.3\text{V}$ . This maybe is due to desorption of some Ni complexes that can form during the cathodic scan [117,147,149]. It was reported that Ni UPD for example, arises from a complexation of Ni cations by the sulfamates adsorbed on the surface [150] and that  $\text{Ni}(\text{OH})_x\text{Cl}_y$  could be detected with Auger Spectroscopy in the Ni

layer electrodeposited from NiCl<sub>2</sub> [147].

At potentials that are cathodic enough to assure the Ni deposition could be noticed that the deposition-rate is smaller if the sweep of the potentials goes in the anodic direction compared to the cathodic one. This can be due to the presence of the oxides and hydroxides on the cathode that will inhibit further Ni deposition [147,148]. After the region where the water decomposition occurs, the probability of forming oxide inhibiting species is higher, therefore, the deposition will be a bit retarded when the sweeping of the potential is made in the anodic direction.

The Ni dissolution occurs after -0.3V, this being seen in the strong decrease in the mass. As discussed above, due to passivation, not all the nickel deposited will dissolve.

The overvoltage of the hydrogen on the gold substrate and on the (previously) deposited Ni layer was estimated following the mechanism proposed by Saubestre [151]. Thus, the potential of the working electrode expressed by the Nernst equation [Eq. 15] can be corrected for the activity and the overvoltage.

$$E = E_0 + \text{activity correction} - \text{overvoltage} = E_0 + \frac{RT}{zF} \ln a_{\text{H}^+} - \eta = 0 - 0.175 - \eta \quad (\text{Eq. 27})$$

The overpotential was estimated from the equation Eq. 27. Furthermore, the overpotential can be written in the form of the Tafel equation as  $\eta = a + b \cdot \log(j)$ . The coefficients  $a$  and  $b$  were calculated from the linear parts of the graphic of overvoltage versus the logarithm of the total current density (Fig. 15). Two linear regions were observed in the overpotential region (until 0.25V) where no deposition was indicated by the resonance frequency of the quartz crystal. In the first linear region the oxygen reduction occurs, as during these measurements the electrolyte was not purged with Ar and as it was proved by the measurements in MgSO<sub>4</sub> electrolyte (section IV.1, p.90). The second linear region is due to the hydrogen evolution reaction. It is obvious from Fig. 15 that at a scan rate of 5mV s<sup>-1</sup>, the  $b$  values slightly increase from 0.195V (on the Au substrate) to 0.221V (on previously deposited Ni) while the  $a$  values are almost constant (0.98 to 1.03V). The increase in the absolute values of  $a$  and  $b$  was also observed when the scan rates were higher. At 50mV s<sup>-1</sup>, the coefficients of the hydrogen overpotential on the Au were:  $a=0.617\text{V}$  and  $b=0.199\text{V}$ . The  $a$  was 1.027V and  $b$  was 0.243V in the case of the hydrogen overpotential on Ni. The values obtained were compared to the values reported in the literature. Saubestre [151] mentioned that  $a=0.67\text{V}$  and  $b=0.116\text{V}$  for hydrogen at 20 °C for a Watts electrolyte. Vetter [113, a] presents a graph from which one can calculate the values of  $a$  and  $b$ . Two different values were reported for the hydrogen overpotential on the Ni substrate by different authors, and

Vetter attributed these differences to the different electrolytes used. Thus,  $b=0.104\text{V}$  and  $a=0.68\text{V}$  (in  $0.1\text{N HCl}$ , respectively in  $0.006\text{N NaOH}$  solutions, at  $20^\circ\text{C}$ ), and  $b=1.06\text{V}$  and  $a=5.32\text{V}$  (in  $\text{HBr}$ ). Furthermore, according to other authors [38], on Au,  $a=0.65\text{-}0.71$  and  $b=0.10\text{-}0.14$ , while on Ni,  $a=0.55\text{-}0.72$  and  $b=0.10\text{-}0.14$  on Au.

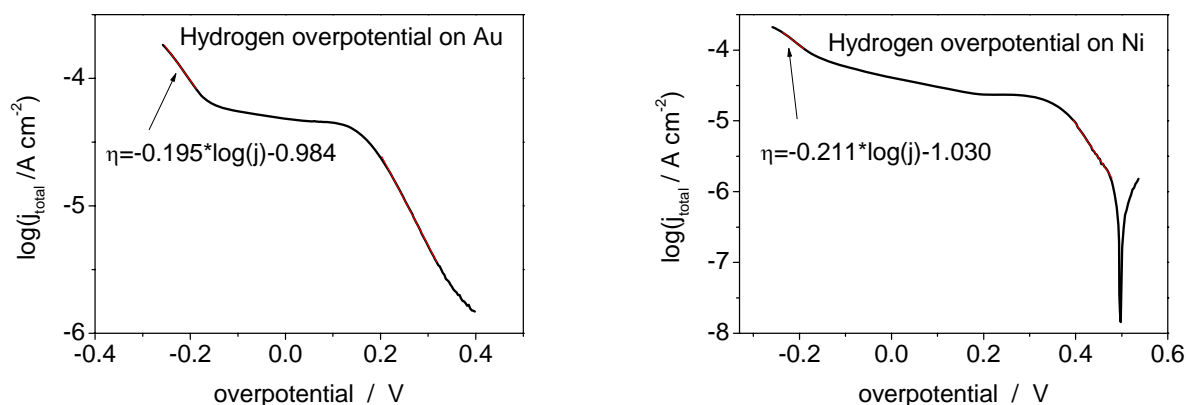


Figure 15. The hydrogen overpotential on the gold substrate calculated during the cyclic voltammograms at  $5\text{mV s}^{-1}$  from  $0.01\text{M NiSO}_4 \cdot 6\text{H}_2\text{O} + 0.1\text{M Na}_2\text{SO}_4$ ,  $\text{pH}=3$ .

The values obtained for  $b$  and  $a$  for our experimental conditions are comparable to those reported in the literature. Furthermore, as the hydrogen overpotential on Ni substrate is larger than on the Au substrate [152], the efficiency of Ni reduction process will be smaller on Au than on Ni.

### III.1.2 Potentiostatic Step Experiments

In the potential region from approximately  $-0.9\text{V vs. SCE}$  till  $-1.2\text{V vs. SCE}$ , nickel deposition takes place together with the hydrogen evolution reaction (Figs. 13 and 14). Potential step experiments were performed from  $0\text{ V vs. SCE}$  to a negative potential in the range ( $-0.9\text{V}$  to  $-1.2\text{V vs. SCE}$ ) and the EQCM signal was recorded. From these data one can get information about the onset of nickel deposition. Furthermore, from the current transient the type of nucleation can be further qualitatively identified: instantaneous or progressive. In Fig. 16 the EQCM signal for two potentials is presented. At  $-0.9\text{V vs. SCE}$ , the frequency increased for approximately 50 seconds with time. The last 10 seconds of the deposition it decreased, but this was not due to nickel deposition. The detachment of the hydrogen

bubbles that are generated on the cathode surface produces sometimes these jumps in the frequency signal [153]. Starting from around -0.95V the Ni deposition establishes despite the HER, but the resonance frequency of the quartz crystal still increased sometimes on small time scales due to the detachment of H<sub>2</sub> bubbles. Therefore, the potentials of -1V and -1.1V vs. SCE were chosen as the deposition potentials.

In Fig. 16 one can observe that the full width at half maximum (FWHM), represented by the values of  $w$ , remains almost constant during the deposition. This is a qualitative indication that the viscosity of the electrolyte is not changing dramatically during the deposition and that the deposited layer is very smooth. The last observation was proved by the AFM measurements (Table 7 and Fig.24 in section III.1.3). The deposited layers had a roughness of approximately 4-9 nm, while the pure Au substrate has a roughness of approximately 4 nm.

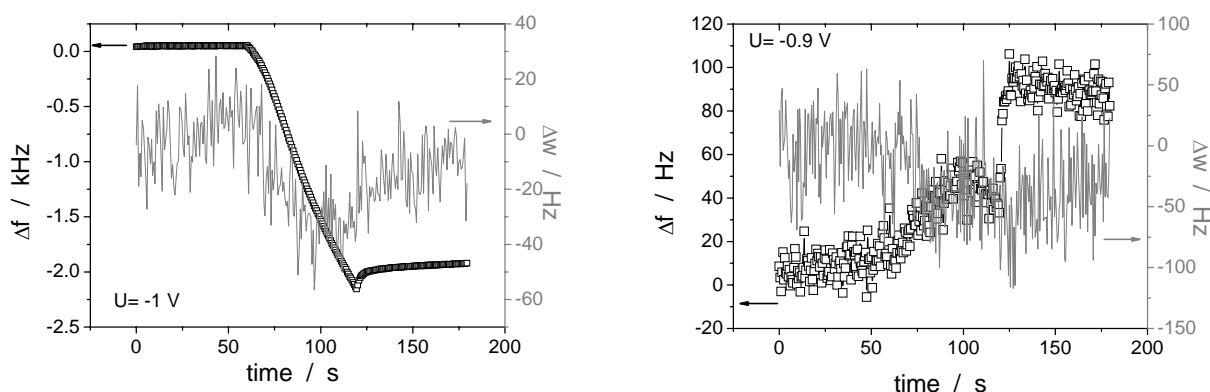


Figure 16. EQCM response during potential steps measurements from 0 V to -0.9 V and -1V vs. SCE. Electrolyte used: 0.01M NiSO<sub>4</sub>\*6H<sub>2</sub>O + 0.1M Na<sub>2</sub>SO<sub>4</sub>, pH=3. No magnetic field was superimposed.

### III.1.2.a Magnetic Field Effects on the Current Transients

In early descriptions of the nucleation process of nickel, it was reported that the current transient (in the case of potentiostatic deposition) exhibits a maximum, after which it slightly decreases and reaches a stationary plateau. The first part of the transient is explained in the same way by different authors: first, a charging current will occur that corresponds to the charging of the double layer. This happens on time scale of some  $\mu\text{s}$ . Then, the increasing part of the transients corresponds to the growth of the first nuclei. In the moment when the

crystallites begin to overlap, a maximum of the total free area of the nickel phase will be reached that will correspond to a maximum in current. Neighboring crystallites will unify. The effect of that will be a suppression of the lateral growth of crystallites that will induce a decrease in the total crystalline area [154]. Furthermore, as the hemispherical diffusion zones overlap, a linear mass-transfer will be achieved that induces a planar further growth [125]. The current then will decrease and approach a steady state value which corresponds to the linear diffusion on planar electrodes (Cottrell regime).

Another approach was taken by Abyaneh and Fleischmann [155]. They affirmed that in the beginning 2D nucleation occurs, that will induce the formation of a monolayer of Ni in parallel to the HER. The increase in the current is due to the 3D nucleation and growth. The last part of the transients is due to the overlap of growing centers, followed by a death process of some of them and the rebirth of new ones. Their model was strongly criticized by Amblard et al. [154] because, in their opinion, the physical meaning of *death* and *rebirth* is far from being evident. Some years later, Fleischmann and Saraby-Reintjes considered that the changes in the form of the transients can be attributed also to the changes of the nickel phase being deposited ( $\alpha$  or  $\beta$ , see also Fig. 14 and the discussions associated to it) due to the codeposition of hydrogen [146]. STM and EQCM investigations proved that the first Ni layer is deposited significantly faster on the pure Au surface than the later Ni layers, which will grow on top of the already deposited Ni monolayer [117]. The transition between these two stages occurs in the region of the current transients where the maximum current is reached. The decrease of the deposition rate of Ni with the time was observed in our work, too (Table 2), which is in perfect agreement with the results of Lachenwitzer and Magnussen [117]. In the present work, it was observed that the shape of the current transients is strongly influenced by the HER. If one extracts the current due to the hydrogen evolution (see section II.2, p.41), the transients look completely different (Fig. 17). In the following calculation (for comparing our experimental data with the nucleation and growth models mentioned above) just the partial current of nickel will be considered. It has to be mentioned again that these calculations were only possible by using the in-situ EQCM method and a special evaluation procedure (see sections I.5.4 and III.1.2.c).

When the depositions were done at -1V vs. SCE, it was difficult sometimes to identify the maximum in the current transients (Fig. 17). Therefore comparison between our experimental data with those predicted by the SH- or SM models was not very accurate for low deposition potentials (Fig. 22).

The maximum current density shifts towards shorter times with increasing deposition

potential. This is the typical behavior for a 3D nucleation and growth of the new phase under diffusion control [156].

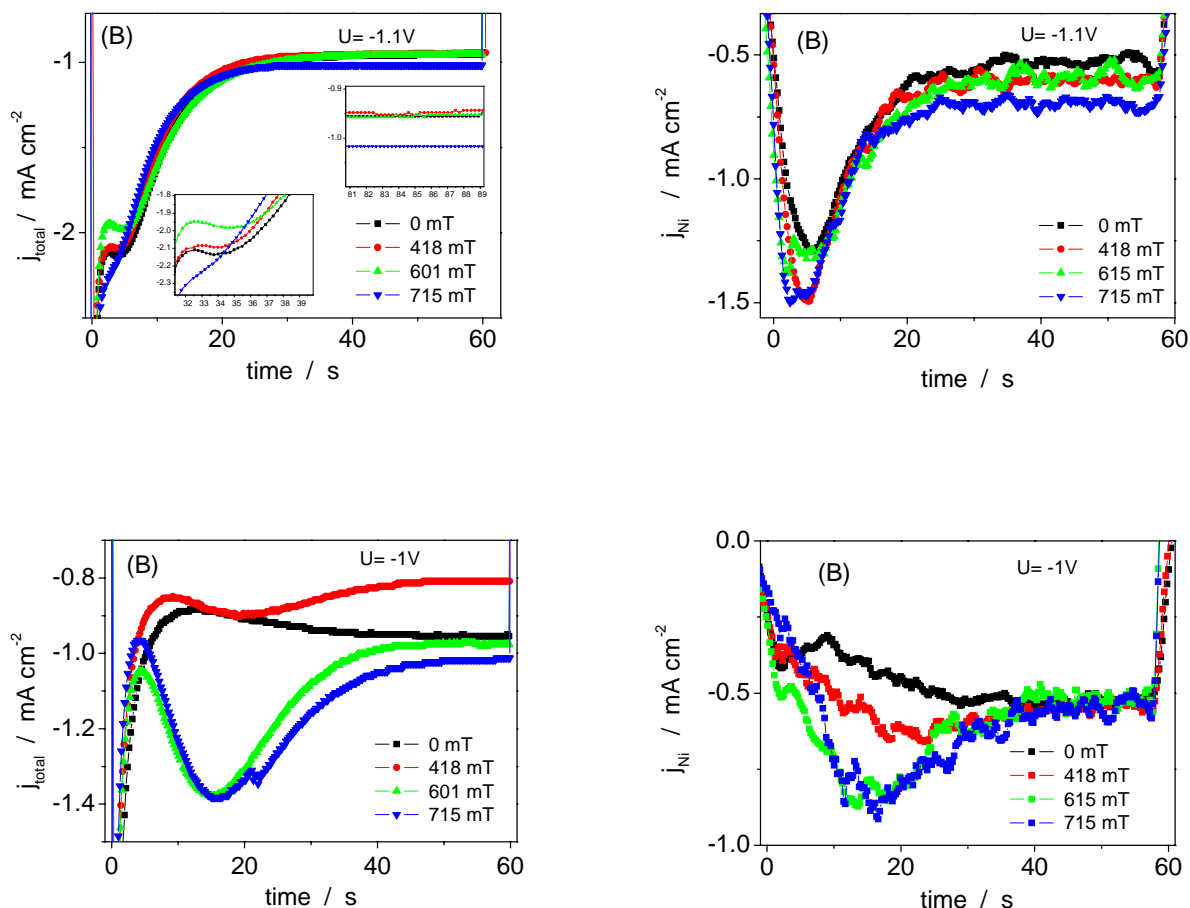


Figure 17. The current transients for the Ni electrodeposition from  $0.01M \text{ NiSO}_4 \cdot 6\text{H}_2\text{O} + 0.1M \text{ Na}_2\text{SO}_4$ ,  $\text{pH}=3$ , in the orientation (B). Right: the transient due just to the Nickel deposition; left, the transient due to the total current. Depositions were lead at a constant potential: up,  $U = -1.1V$  vs. SCE and down,  $U = -1V$  vs. SCE.

Typical current transients for the orientations (A) and (B) (see Fig. 10, p.38) can be seen in Figs. 17 and 18. In both cases the Lorentz force should be active. However, the interplay between the natural convection (NC) and the additional convection imposed by the Lorentz force can be clearly seen comparing the two graphs. When both forces act in the same direction (orientation B), an increase of the limiting total current, as well as of the pure nickel current, is obtained. This happens because the hydrogen as well as the nickel is mass transport controlled in the potential range chosen; therefore the primary effect of the additional convection of the electrolyte is to increase the limiting current density. For

smaller potentials, the effect on the partial current of Ni can be seen just for short deposition times, while at higher potentials it can be noticed during all the deposition. This can be correlated with the higher depositions rates of Ni in the beginning of the deposition compared to the last part of the deposition (Table 2, orientation (B)). At very short times, it seems that the hydrogen evolution reaction is inhibited by the magnetic field. HER and Ni deposition occur in parallel. It seems that in the beginning the additional convection favors the mass transport of the Ni species in comparison to the hydrogen. This can be due to the fact that the hydrogen is a diamagnetic species, while the Ni is paramagnetic. It can happen that for small times hydrogen species will be repelled from the electrode, while the Ni ions will travel to the electrode under the influence of the magnetic field gradient forces [see section I.3.1, p.11].

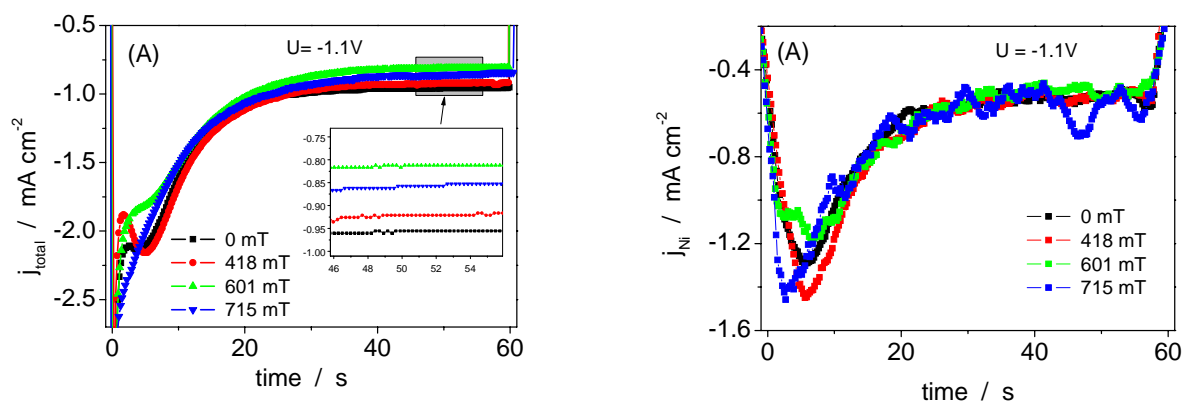


Figure 18. The current transients for the orientation (A). Same electrolyte as in Figure 17.

For the orientation (A), the natural convection has an opposite direction compared to the Lorentz force. The differences in the current transients are obvious compared to those obtained for the orientation (B). With increasing the magnetic field, the total limiting current decreases. The partial current of nickel is affected just at short times, during the formation of the first layers. The effect of the B field is a positive one for the initial Ni growth, similar to what was observed for the orientation (B). However, the further growth was not influenced. Similar behavior was obtained in the case when Ni was deposited at -1V vs. SCE.

One should take into account that the natural convection occurs only after some tens of seconds [143]. Thus, the increase of the current density of Ni with the magnetic field that could be observed in both orientations (A and B) is due just to the MHD convection during the first seconds of deposition. After 20 seconds of deposition, when the natural convection is for sure active, one can see that the Ni current density increases in the orientation B, while

in orientation A it is not any longer influenced. This proves the interplay of the natural and MHD convections.

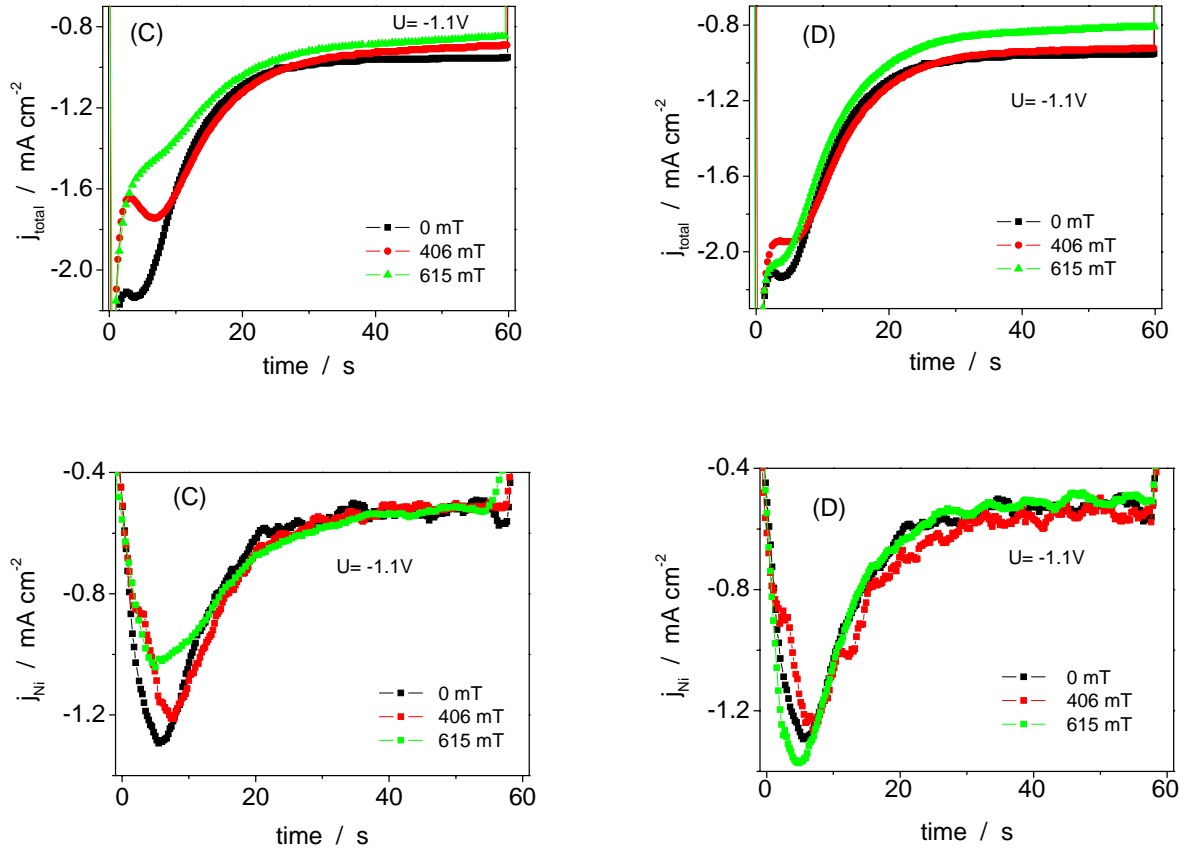


Figure 19. The current transients for the orientations (C) and (D). Same electrolyte as in Figure 17.

In Fig. 19 are presented the current transients obtained in the case when no macroscopic Lorentz force should be present. The absence of the Lorentz force is due to the fact that the magnetic field ( $B$ ) direction is parallel to that of the electric field ( $E$ ). Thus, the vectorial product of  $B$  and  $E$  should be zero (Eq. 10). One can easily see that the total current decreases in the presence of the magnetic field. The decrease of partial current of nickel with the magnetic field is observable during the first seconds of deposition, like it was obtained for the orientations (A) and (B), too. The decrease in the current can be correlated with the action of the paramagnetic force,  $F_{\nabla c}$ .  $F_{\nabla c}$  arises from the variation in the paramagnetic susceptibility of the diffusion layer due to the concentration gradient of the cations there [157].  $F_{\nabla c}$  acts in the direction of the gradient of concentration, parallel to the



thermodynamic driving force for diffusion ( $RT\text{grad}(c)$ ) [see section I.3.1]. As this force depends just on the intensity of the magnetic field and not on its direction, the changes of the current transients with the magnetic field were the same for both orientations ((C) and (D)).

### III.1.2.b Magnetic Field Effects on the Deposited Mass

Two linear regions could be distinguished in the mass transients (Fig. 20). The mass increases more strongly during the first ten seconds of the deposition, in comparison to the further growth. The changes in the slope of the mass transients can be associated to the point when the current densities reach their maximum values (Figs. 17-19).

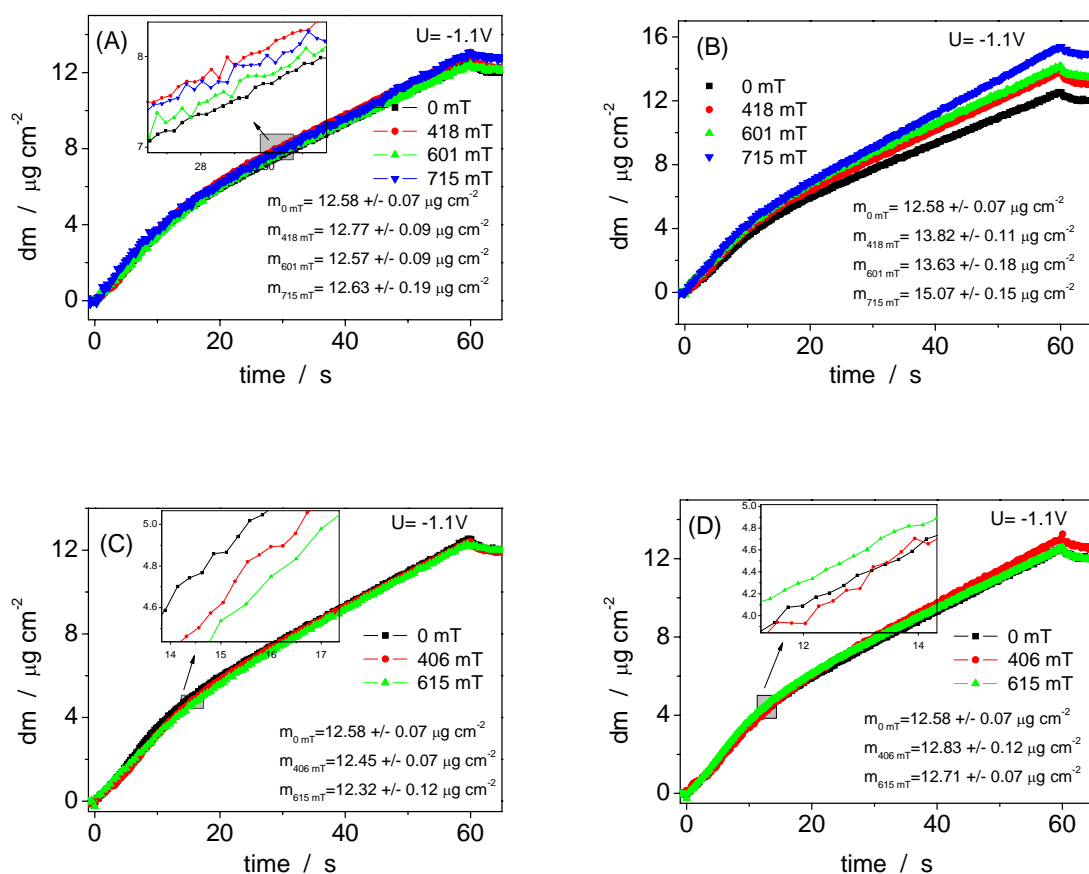


Figure 20. Mass transients for the potentiostatic electrodeposition at  $-1.1\text{V}$  vs. SCE of the Ni from  $0.01\text{M NiSO}_4 \cdot 6\text{H}_2\text{O} + 0.1\text{M Na}_2\text{SO}_4$ ,  $\text{pH}=3$ . (A), (B), (C) and (D) describe the different orientations analysed.

The average values (from a series of measurements) of the total mass electrodeposited for a given condition are presented in the legends of the Fig. 20. One can see that the total deposited mass is almost the same in the orientations (A), (C) and (D). It increases

significantly in a magnetic field just for the orientation (B). This is another evidence of the MHD effect on the mass transport processes and proves once again how important the direction of the forces is. Just in the case when Lorentz force and natural convection force act in the same direction one can observe the increase in the deposited mass.

The deposition rates were calculated from the slopes of the mass transients, in the two linear parts observed (Fig.20). The results are summarized in the following table (Table 2).

Table 2. Slopes of the linear part of the plots $m(t)$ . The units of the deposition rates reported here are $\text{ng cm}^{-2} \text{s}^{-1}$ . (A), (B), (C) and (D) represent the different orientations of the cell with regard to the direction of the magnetic field (Fig. 10, p.38).					
<b>E [V] vs. SCE</b>	<b>B= 0 T</b>	<b>(A) 0.7 T</b>	<b>(B) 0.7 T</b>	<b>(C) 0.6 T</b>	<b>(D) 0.6 T</b>
<b>-1 (first10s)</b>	113±1	111±5	227±9	112±5	114±8
<b>-1 (last30s)</b>	160±3	163±1	174±1	162±1	163±3
<b>-1.1 (first10s)</b>	370±4	407±9	433±10	315±11	354±15
<b>-1.1 (last30)</b>	161±2	171±5	211±3	162±1	163±2

Different behaviors for the deposition rate were obtained for the two deposition potentials. At more cathodic potentials, the Ni deposition rate is higher in the beginning of the deposition and decreases significantly at the end, while for less cathodic potentials, (except the orientation B), it seems that the deposition rate of Ni increases at the end of the deposition. This can be due to the competition for reduction between the Ni and hydrogen species. At lower potentials, the HER occurs preferentially and blocks initially the surface for Ni deposition. After some growth centers of nickel are formed, it seems that further metal growth is favored in spite of the HER. At higher potentials, the HER will reach its limiting plateau more quickly and the Ni deposition will follow its deposition kinetics already mentioned in literature [116,117]: first Ni monolayer grows more quickly than the following layers.

From Table 2 one can see that a superimposed magnetic field influences the deposition rates, too. For the orientations (A) and (B) the MHD effect induces an increase of the

deposition rate. The effect becomes visible at higher potentials for the orientation (A) and it is observable all the time for the orientation (B). This difference in function of the time scale observed for the two orientations proves once again the interplay between the natural and MHD induced convections. For the orientations (C) and (D) the deposition rates seem not to be influenced by the presence of the magnetic field. Paramagnetic forces and the forces due to the gradient of the magnetic field are present for these orientations, but they do not influence the mass transport. A slight decrease is observable for the orientation (C) in the first seconds of deposition at high potentials. This can be correlated to the micro-MHD turbulences that occur on the electrodes and that seem to induce a slight inhibition of the deposition when the electric field and the magnetic field have opposite directions (see the Aogaki's model, section I.3.1, p.11).

### **III.1.2.c Magnetic Field Effects on the Nucleation and Growth**

When a magnetic field was applied, a change of the shape of the current transients could be noticed during the first seconds (Fig. 19) that could be induced by changes in the nucleation mechanism. In order to identify the type of nucleation that occurs for different values of the magnetic field, our experimental data were compared to some theoretical functions, which were mentioned in section I.5.4, p.26.

Analysis of our experimental transients was done with a fitting procedure based on the Levenberg-Marquardt algorithm (following the ideas from [121]), with the nucleation site density and the nucleation rate as fitting parameters (see Appendix, p.135). The Levenberg-Marquardt algorithm determines the best fit parameters by finding the minimum of the merit function in a number of iterations [158]. Between ten and one hundred iterations were performed for our data sets. The Dawson's integral and the Levenberg-Marquardt algorithms were implemented in C++ and the fitting function was introduced in Origin.

Before discussing the results obtained by fitting the experimental data with different theoretical models, it has to be noted that the current density considered in all the fittings is in fact just the partial current of Ni deposition. This current was obtained from the EQCM data, by derivate the deposited mass in time.

#### ***III.1.2.c.1 Scharifker-Hills Model***

In Fig. 21 the results obtained by comparing the dimensionless transient curves, obtained

in the case that the deposition was done at  $-1.1\text{V}$  vs. SCE, with the functions predicted by the SH model, are presented. The comparison is acceptable for potentials like  $-1.1\text{V}$  vs. SCE, but it is not so accurate for lower potentials (Fig.22). For most of the transients, the nucleation seems to be an instantaneous one before the current reaches its maximum and then it becomes slowly progressive (Table 3).

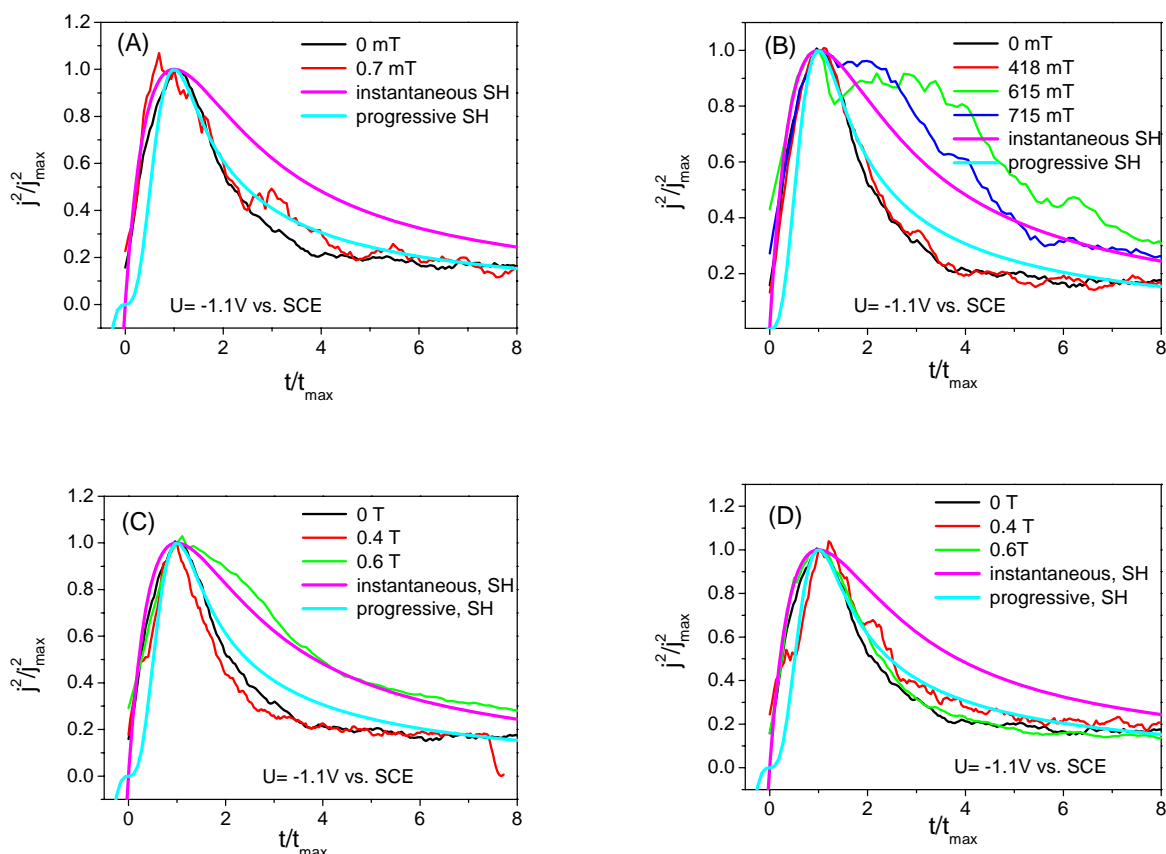


Figure 21. Comparison between the experimental transient curve obtained for Ni deposition from  $0.01\text{M NiSO}_4 \cdot 6\text{H}_2\text{O} + 0.1\text{M Na}_2\text{SO}_4$ ,  $\text{pH}=3$  to those predicted by the SH model (instantaneous and progressive nucleation). In this example, just the Nickel current transient was considered in calculations. Orientations investigated: (A), (B), (C), (D). Deposition was done at  $-1.1\text{V}$ .

Thus, it was observed that the magnetic field influences besides the partial current of Ni also the type of nucleation. This influence is more obvious in the case of the orientation B: at higher magnetic fields, the nucleation remains instantaneous even after the maximum. For this orientation, the Lorentz force acts in the same direction as the natural convection, therefore, one expects that the additional convection induced in the electrolyte to be

maximal. From the results obtained it is obvious that the simultaneous action of a magnetic field with the natural convection is to favor the instantaneous nucleation. For the orientation (C), the nucleation (which is instantaneous before the maximum current density) continues to be instantaneous at higher values of B field, even after the current reached its maximum. At low intensities of the magnetic field, the nucleation in the orientation (C) is progressive (Table 3). These effects can be due to the micro MHD turbulences that interfere with the growth centers.

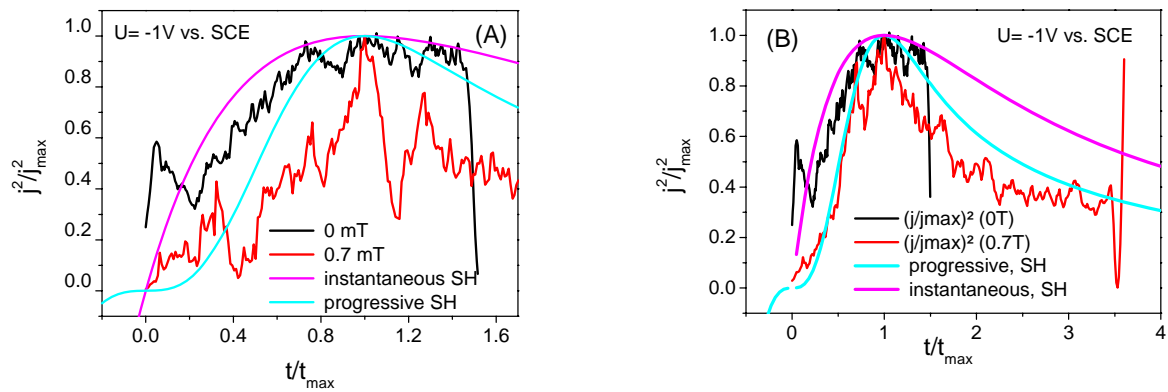


Figure 22. The experimental curves obtained in the case that the deposition was done at -1V vs. SCE, in orientation (A) and (B) and the theoretical curves predicted by the SH model. Same electrolyte as in Figure 21.

The experimental data seem to show that the instantaneous nucleation is favored when the direction of the electric field and the magnetic field are antiparallel. When they are parallel, it seems that that the progressive nucleation dominates after the current reaches its maximum value. The mechanism that induces these effects could not be fully clarified.

Table 3. Nucleation type, according to the SH model, for the different orientations of the working electrode with regard to the direction of the magnetic field. Deposition potential - 1.1V vs. SCE.					
	<b>B= 0 T</b>	<b>(A) 0.7 T</b>	<b>(B) 0.7 T</b>	<b>(C) 0.6 T</b>	<b>(D) 0.6 T</b>
<b>before <math>j_{\max}</math></b>	instantaneous	instantaneous	instantaneous	instantaneous	instantaneous
<b>after <math>j_{\max}</math></b>	progressive	progressive	instantaneous	instantaneous	progressive

One weak point of the SH model is that it can not predict accurately the changes that occur at the transition from one nucleation type into the other. It can describe just the limiting

cases of instantaneous and progressive nucleation. However, the transition between the two types of nucleation is not unusual. For example, some experimental results described a transition from progressive to instantaneous nucleation for electrodeposition of mercury onto vitreous carbon [125] or for electrodeposition of Co on a Pt/Si(100) substrate [126].

### III.1.2.c.2 Scharifker-Mostany Model

Equation 20 was the merit function which was used in fitting the experimental data according to the SM model. The parameters  $A$  and  $N_0$  were determined by successive iterations based on the Levenberg-Marquardt algorithm. The results obtained are presented in Table 4. One can see that fitting the data with the SM model gives similar results for the nucleation site density and nucleation rate constant in the magnetic field and without magnetic field, for different orientations. This behavior of  $A$  and  $N_0$  was unexpected, based on the previous observations (Table 3). However, it was underlined [127] that the SM model can predict for different set of  $A$  and  $N_0$  values similar current transients. One can deduce that during the fitting procedure, the computer finds a set of fitting values ( $A$  and  $N_0$ ) that gives the minimum of the merit function but that are not the unique solutions for obtaining this minimum. The values obtained depend on the initial values of the fitting parameter that are suggested to the computer. Our conclusion was that the Levenberg-Marquardt algorithm applied for SM model is not suitable for fitting our experimental data.

Table 4. Nucleation site density ( $N_0$ ) and nucleation rate constant ( $A$ ) according to SM model, for the different orientations of the working electrode with regard to the direction of the magnetic field. Here the deposition potential was -1.1V vs. SCE. In the fitting the experimental data between 2 and 150 seconds were taken into account.

<b>B (T)</b>	<b>A (s<sup>-1</sup>)</b>	<b>N<sub>0</sub> * 10<sup>-9</sup>(cm<sup>-2</sup>)</b>
<b>0</b>	0.82±0.01	5.6±0.1
<b>0.7-A</b>	0.85±0.02	8.3±0.2
<b>0.7-B</b>	0.83±0.02	9.9±0.4
<b>0.6-C</b>	0.69±0.01	3.6±0.1
<b>0.6-D</b>	0.85±0.02	7.3±0.2

### III.1.2.c.3 Heerman-Tarallo Model

In Fig. 23 are plotted the values of the nucleation site density ( $N_0$ ) and nucleation rate constant ( $A$ ) versus the values of the magnetic field applied, for the different orientations (A, B, C, D). The fitting was done for the potentiostatic depositions at -1.1V vs. SCE. Only the part of the current transients between 8 seconds and 50 seconds was selected for calculating  $N_0$  and  $A$  (Fig. 23). Fitting of the first part of the current transients gave usually relatively high errors, which were even higher than the determined value itself (Table 5).

The average values of  $N_0$  and  $A$  were calculated from a series of identical measurements. These values are plotted in Fig. 23. The error bar represents the standard error of the measurements.

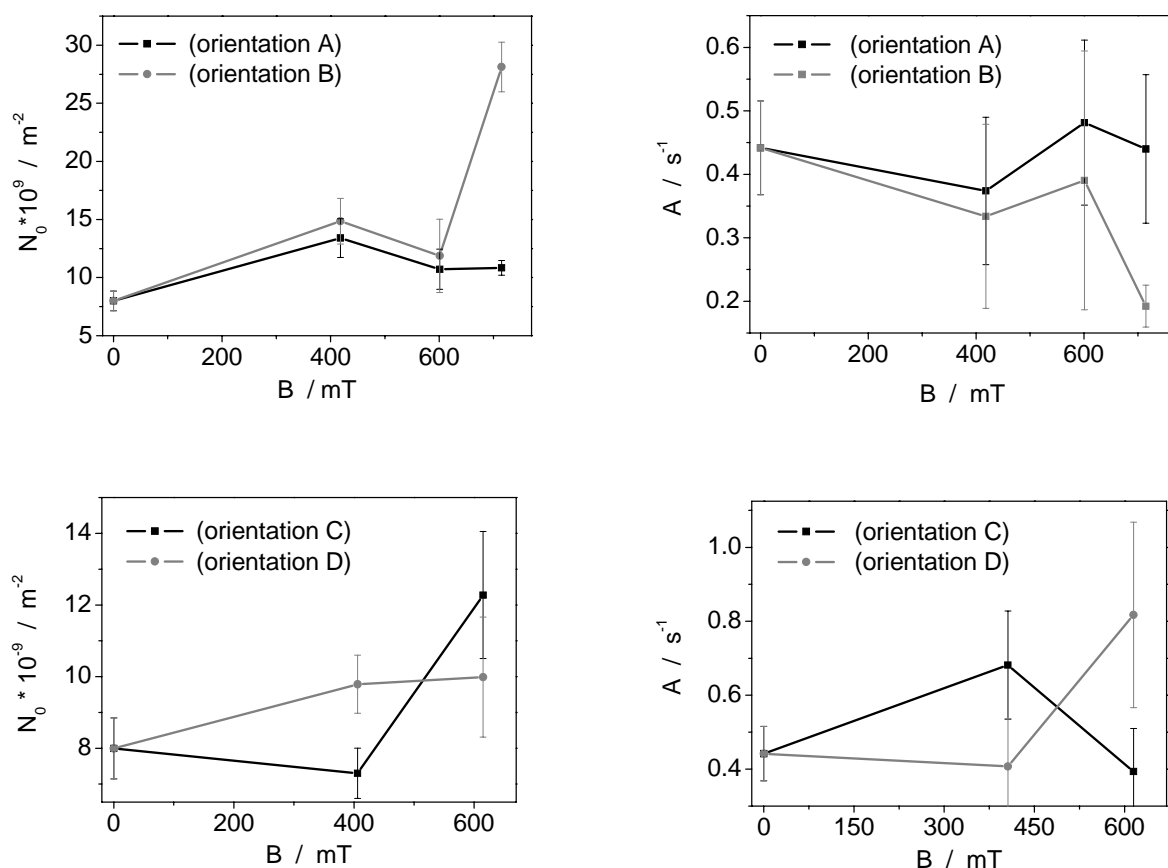


Figure 23. Nucleation site density ( $N_0$ ) and nucleation rate constant ( $A$ ) for the different orientation of the WE with regard to the external magnetic field applied, as a function of the magnetic flux density. The depositions were done at -1.1V vs. SCE. Same electrolyte as in Figure 21.

Instantaneous nucleation implies a high growth rate of the new phase and a small number of formed active nucleation sites, while the progressive nucleation implies a slow growth rate and a large number of new nuclei formed. In the literature, the calculated values of  $N_0$  for different systems (Cu, Ag, Ni, Hg, etc) were between  $10^4\text{cm}^{-2}$  and  $10^{10}\text{cm}^{-2}$  [121]. These large differences can be explained by the different experimental conditions, like different pretreatment of the electrode, the presence of additives or different potentials used for electrodeposition [121]. Usually, if  $A \ll 1$  then the progressive nucleation occurs, while  $A \gg 1$  is specific for the instantaneous nucleation [127].

The  $N_0$  values obtained for our experimental conditions are around  $10^9\text{cm}^{-2}$ , and the  $A$  values are smaller than unity (1) for the part of the current transients recorded after 8 seconds. These  $A$  values should correspond to a typical progressive nucleation. Furthermore, one can notice that the values of  $A$  decrease with the magnetic field for the orientations B and C, while the  $N_0$  values increase (Fig. 23). These facts indicate that under the influence of a magnetic field the nucleation is progressive for the orientations B and C ( $A \ll 1$  for high  $B$  values), for the part of current transients recorded after  $j_{\text{max}}$ . This observation is in contradiction to the results obtained from the SH model (Table 3). However, one should take into account the differences between the SH and HT models, expressed in the way the authors considered the changes in the current density with time.

The most remarkable effect induced by the magnetic field was noticed for the orientation B: the number of nucleation sites increased strongly in a magnetic field. A slight increase of  $N_0$  was observable for the orientation C, too, while for the orientations A and D no significant effects could be noticed (Fig. 23). As mentioned before, the  $N_0$  values are the most sensible to changes of the experimental conditions. Therefore, the strong additional convection induced in orientation B will give the most remarkable results. The decrease of the  $A$  values (from  $0.07 \pm 0.007$  to  $0.02 \pm 0.004$ ) and the increase of the  $N_0$  (from  $(1.38 \pm 0.8) \cdot 10^9$  to  $(13.53 \pm 2.7) \cdot 10^9$ ) was observed for the orientation B when the deposition was made at -1V, too.

The values of  $A$  and  $N_0$  for the first seconds of the deposition at -1.1V are presented in Table 5. One can notice that  $A$  values are higher than the unity, which is specific for an instantaneous nucleation. Unfortunately, due to the high errors obtained, one can not speculate about the mechanism which could describe the effects induced by a magnetic field on the values of  $A$  and  $N_0$  during the first seconds of deposition.



Table 5. Nucleation site density ( $N_0$ ) and nucleation rate constant ( $A$ ) according to HT model, for the different orientations of the working electrode with regard to the direction of the magnetic field. Here the deposition potential was  $-1.1V$  vs. SCE. In the fitting of the experimental data just the first 8-10 deposition seconds were taken into account.

B (T)	A ( $s^{-1}$ )	$N_0 * 10^{-9}(cm^{-2})$
0	$5 \pm 2$	$4.6 \pm 0.1$
0.6-A	$31 \pm 32$	$5.9 \pm 0.6$
0.6-B	$32 \pm 20$	$6.0 \pm 0.5$
0.6-C	$30 \pm 24$	$7.4 \pm 2.0$
0.6-D	$13 \pm 3$	$6.7 \pm 1.0$

### III.1.3 AFM Investigations on the Topography, Roughness and Grain Size of Deposited Ni Layers

In Fig. 24 the AFM height images corresponding to the Ni deposition from  $0.01M$   $NiSO_4 \cdot 6H_2O + 0.1M$   $Na_2SO_4$ ,  $pH=3$  are presented. One can see that the uniformity of the deposited layers increases in the orientations (A) and (B) with the magnetic field.

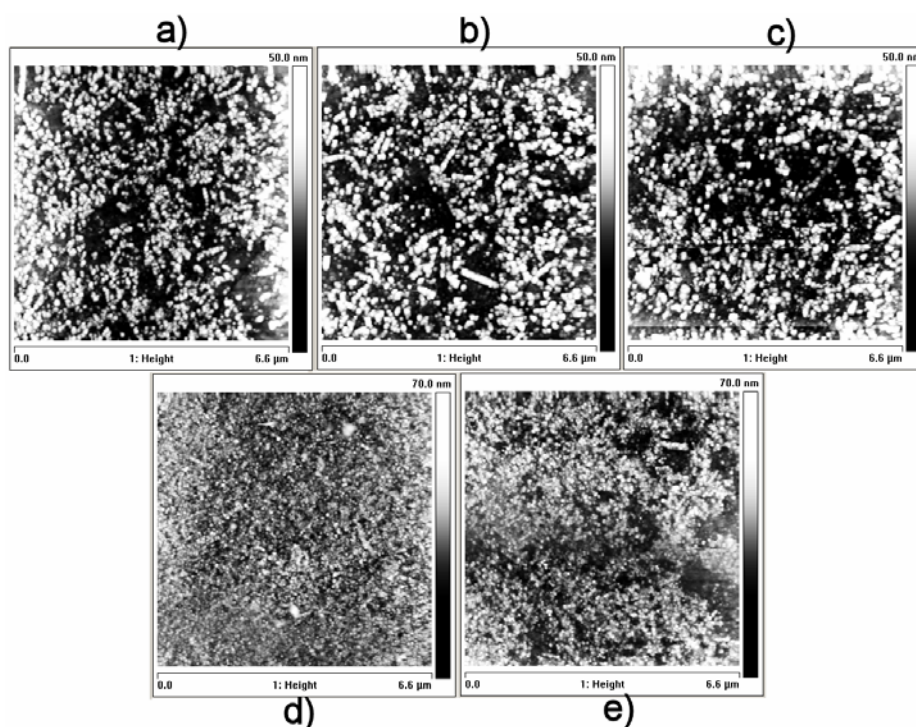


Figure 24. Height images of the Ni layers deposited at  $-1.1V$  vs. SCE from  $0.01M$   $NiSO_4 \cdot 6H_2O + 0.1M$   $Na_2SO_4$ ,  $pH=3$ . a)  $B=0T$ ; b)  $B=0.6T$ -orientation C; c)  $B=0.6T$ -orientation D; d)  $B=0.7T$ -orientation B; e)  $B=0.7T$ -orientation A.

Using the AFM software, one can determine the total number of grains in the scanned area ( $6.6\mu\text{m} * 6.6\mu\text{m}$ ) (Table 6). There are two types of values reported: one refers to the whole scanned area and one refers to a selected area. The selected area is chosen by the AFM software based on similarities of more neighbouring grains (like similar dimensions). The minimum dimensions of the grains counted were 14 nm in diameter and 18 nm in length and width.

The number of grains deposited in orientation (B) in a magnetic field is much higher in comparison to the other orientations and to the case of no magnetic field (Table 6). Furthermore, for the orientations (A) and (B) more grains were counted over the whole scanned area in comparison to the orientations (C) and (D). This can be explained by the MHD effect. For the orientation C the number of grains counted by the software is smallest, while for the orientation D it is slightly higher than that obtained in no magnetic field. The results prove the importance of the orientation of the magnetic field with regard to the electric current and the direction of natural convection.

Table 6. Number of grains and the grain size mean for the Ni layers deposited at -1.1V vs. SCE for different orientations.

<b>B (T) - orientation</b>	<b>Number of grains</b>		<b>Grain size mean (nm<sup>2</sup>)</b>	
	area selected	whole area	area selected	whole area
<b>0</b>	48	235	366	27508
<b>0.7-A</b>	68	445	218	8120
<b>0.7-B</b>	312	1021	439	8365
<b>0.6-C</b>	29	150	255	6556
<b>0.6-D</b>	85	371	505	19214

The magnetic field does not influence significantly the mean grain size of the Ni layers deposited 60 seconds at -1.1V vs. SCE from 0.01M NiSO<sub>4</sub>\*6H<sub>2</sub>O + 0.1M Na<sub>2</sub>SO<sub>4</sub>, pH=3 (Table 6). However, the mean grain size (as well as the total number of grains) increased with increasing the deposition potential. Thus, the mean grain size of a group of grains with similar dimensions deposited at -1V vs. SCE was 287 nm<sup>2</sup>, 366 nm<sup>2</sup> at -1.1V and 982 nm<sup>2</sup> at -1.2V. If one compares the results given by the AFM software (Table 6) with those obtained from fitting the experimental curves with different nucleation models, one can see that the HT model is in accordance with the experimental data. This can be easily observed in the

case of the orientation (B): both the AFM information and the  $N_0$  values obtained from HT model indicate a strong increase of the number of nuclei with the magnetic field.

The roughness of the deposited layers was calculated from the height images (see section II.1.3). The results are presented in Table 7. One can see that the roughness increases with increasing deposition potential (due to more Ni deposited), but seems not to be influenced by the intensity and direction of the magnetic field.

		-1V	-1.1V
		$R_q \pm \text{s.e.}$	$R_q \pm \text{s.e.}$
<b>gold substrate</b>		3.86 ± 0.83	
0mT		5.18 ± 0.02	7.10 ± 0.10
<b>Orientation (A)</b>	418mT	4.81 ± 0.2	5.24 ± 0.55
	601mT	3.56 ± 0.12	3.95 ± 0.20
	715mT	4.17 ± 0.25	6.62 ± 0.44
<b>Orientation (B)</b>	418mT	3.60 ± 0.93	7.39 ± 0.71
	601mT	5.27 ± 0.35	4.33 ± 1.17
	715mT	4.10 ± 0.80	6.08 ± 0.53
<b>Orientation (C)</b>	406mT	5.63 ± 1.87	6.78 ± 0.15
	615mT	3.54 ± 0.02	9.58 ± 2.22
<b>Orientation (D)</b>	406mT	4.36 ± 1.8	6.78 ± 0.17
	615mT	3.93 ± 0.34	7.82 ± 0.48

### III.2 Ni Electrodeposition from a Sulfamate Bath

The cyclic voltammograms obtained from sulfamate and sulfate baths were alike at a first glance (Fig.14, Fig. 25). However, in the sulfamate bath, the deposition of Ni begins at more anodic potentials (around -0.65V vs. SCE compared to -0.9V vs. SCE in the sulfate bath). It was pointed out that the cathodic current increases at a more negative potential in absence of boric acid [159]. This observation together with the higher Ni concentration in the electrolyte can explain the differences in the deposition potential between the sulfate and the sulfamate bath.

Another characteristic is that the current curve during the anodic sweep lies more cathodic than the current obtained in the cathodic scan for the potential region between -0.6 and -0.9V vs. SCE. This was not obtained for the sulfate bath. In the case of Ni deposition on glassy carbon substrate [160] this behaviour of the current was attributed to the Ni nucleation on foreign substrate together with the effect of the substrate on the rate of HER. However, in our case, the increase in the roughness of the deposited layer, which will induce a change of the active area, is considered to be responsible for the observed behaviour of the current. It can not be just the hydrogen overvoltage on different substrates, as for the sulfate bath, as well as for the sulfamate bath, the overpotential of hydrogen on Ni is higher than on Au substrate.

In the anodic scan, two dissolution peaks could be observed, like in the case of sulfate baths. The dissolution peaks shift to more anodic potential with time, and, at the same time, the proportion of  $\alpha$ -Ni (solid solution of hydrogen in Ni,  $H/Ni \approx 0.03$ ) increased in comparison to  $\beta$ -Ni ( $H/Ni > 0.6$ ) [see section III.1.1]. From the slopes of the mass density (calculated from the EQCM data) versus charge density, the molar mass was calculated according to Faraday's law. The molar mass values ( $M$ ) were between 56 and 57 g/mol for the pure sulfamate bath and between 47 and 54 for the sulfamate bath with SDS. As these values are not very far from the tabulated molar mass of Ni (58.69g/mol), we can assume that the incorporation of complexes (see discussions on p.45, [117,147,149]) in the deposited layer during the cyclic voltammograms is limited.

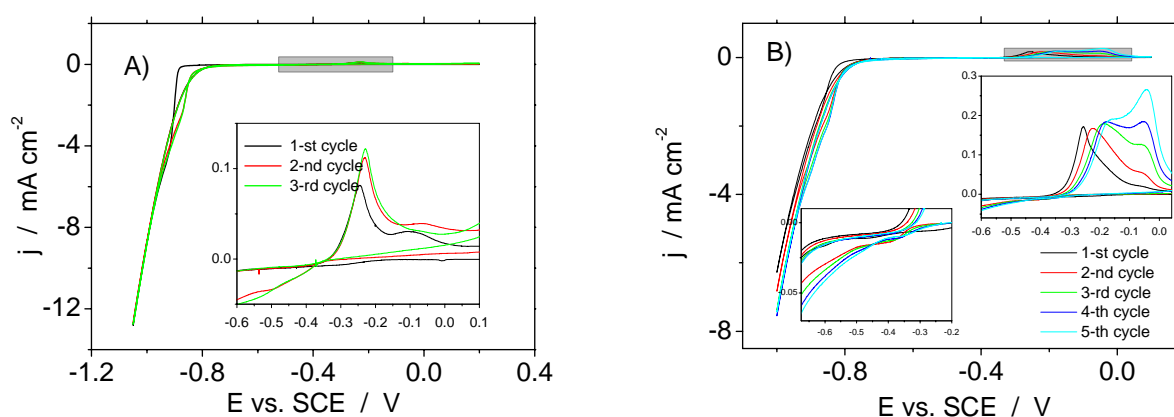


Figure 25. Cyclic Voltammograms at  $1\text{mV s}^{-1}$  in  $B=0\text{T}$ . A) pure sulfamate bath ( $1.26\text{M Ni}(\text{SO}_3\text{NH}_2)_2 \cdot 4\text{H}_2\text{O} + 0.32\text{M H}_3\text{BO}_3 + 0.04\text{M NiCl}_2 \cdot 6\text{H}_2\text{O}$ ,  $\text{pH}=4.$ ); B) Ni sulfamate bath  $+0.52\text{mM SDS}$ .

The presence of a surfactant affects the Ni deposition process as well as the dissolution process (Figs. 25,26). Thus, in the cathodic scan, in the presence of SDS the current, respectively the deposited mass, increase at less cathodic potentials (80-100mV vs. SCE less than in the pure Ni sulfamate bath) (Fig. 26). However, at higher cathodic potentials the current and the deposited mass are smaller for the bath with surfactants (Fig. 26), probably due to the inhibition of the active sites by the SDS. At the same time, the anodic dissolution peak is slightly higher in the presence of SDS, which indicates that the Ni dissolution is not inhibited by the surfactant.

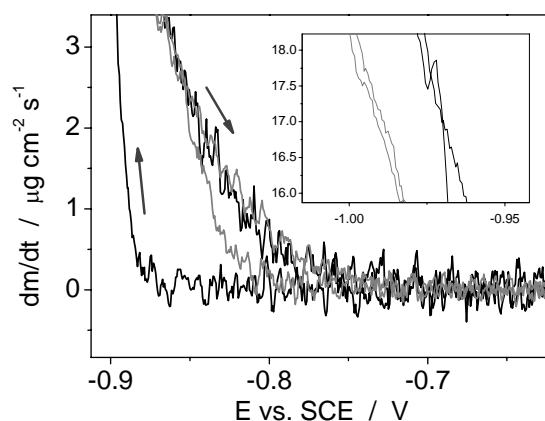


Figure 26. Deposition rates calculated from the first cycles of the CV at  $1\text{mV s}^{-1}$  from a Ni sulfamate bath without surfactants (black curve) and a Ni sulfamate bath with  $0.52\text{mM}$  SDS (grey curve).

As in the case of the sulfate bath, not all the Ni is dissolved during the anodic scan, due to the passivation of the Ni layer.

It is known that surfactants can form easily aggregates, such as micelles, if their concentration in the electrolyte is higher than the critical micelle concentration, cmc [161]. These aggregates can be adsorbed on the electrode surface and can influence the rate of electrodeposition. The mechanism that induces the changes of the electrodeposition rate is not fully understood. One possible explanation is that the surfactant aggregates would act as a bridge mediating the electron transfer reaction or that they could form complexes with the ions that will be plated [161]. Therefore, the cyclic voltammograms obtained in the presence of surfactants were different than those obtained in absence of the surfactants.

### III.2.1 XRD Investigations

Unlike the Ni deposited from a Watts bath, the texture of Ni from sulfamate bath, as a function pH and additives, has not been intensively studied. Recently, the texture of Ni layers as a function of the applied current density and temperature was discussed for a Ni sulfamate bath with SDS but without NiCl<sub>2</sub> [162,163] or for a sulfamate bath free of surfactants [164]. The effects of a magnetic field on the deposited Ni texture were mostly investigated for the case when Watts baths (containing NiCl<sub>2</sub>, NiSO<sub>4</sub> and H<sub>3</sub>BO<sub>3</sub>), chloride or pure sulfate baths were used. The present investigations were made for the Ni layers deposited from a sulfamate bath.

In the beginning, XRD measurements were done on the substrate (quartz crystal with Au electrodes) used in this study. In Fig. 27 one can see a zoom-in of the XRD pattern obtained for such a blank working electrode. We noticed that the highest intensity corresponds to Au (111) (approximately 40000counts/s) and quartz (101) (approximately 7000counts/s). The reflections from the chromium layer were very weak, due to the fact that it has a thickness of just 5nm. One can conclude that the strongest diffraction peaks corresponding to the substrate are expected at small angles ( $2\theta$  less than  $40^\circ$ ).

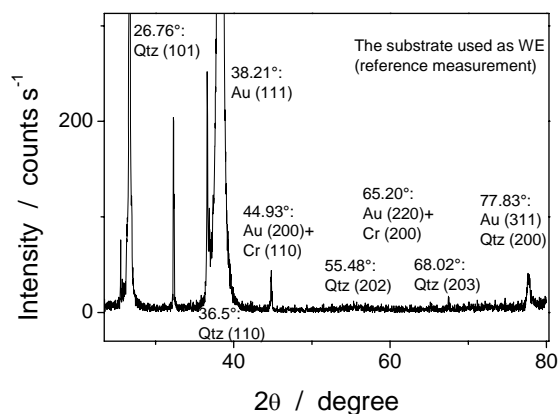


Figure 27. XRD pattern for the blank working electrode, which is a quartz crystal with Au electrodes evaporated on its parallel faces, onto a thin Cr layer.

Two cases were studied: one time the total charge that passed was  $1.5\text{C cm}^{-2}$  and the thickness of the layers was approximately  $0.5\mu\text{m}$  (Fig. 28A) and in the other case, the corresponding charge that passed was  $17.5\text{C cm}^{-2}$ , giving a layer of approximately  $5.4\mu\text{m}$  (Fig. 28B). For the Ni samples the magnetic field was applied perpendicular to the electric

current, in orientation E (see Fig. 10, p.38).

One can see clearly (Fig. 28A and B) that the intensity of the peak corresponding to the texture Ni(111) increases in a magnetic field. The other peaks (corresponding to Ni (200) and Ni (220)) are not affected by the presence of the magnetic field in the case of the thin layers (Fig. 28A), but for the thick layers, the intensity corresponding to the plane (220) seems to increase in a magnetic field (Fig. 28B). The increase in the intensity of the peaks in a magnetic field can be attributed to MHD effect [10]. The magnetic field increases the partial current of hydrogen. Thus the inhibiting species ( $H_{ads}$  and  $Ni(OH)_2$ ) become more numerous, and this will influence the preferred crystalline orientation ([98,101], see section I.4, p.18). However, we have to mention that EDX analyses made on the nickel layers did not prove the presence of the hydroxide species. Furthermore, the current efficiency calculated from the EQCM data was less than 100%. This is another indication that in the case of the bath used in the present study the hydroxides species are not incorporated in the deposited layer.

In the case of Ni layers, the maximum intensities appear at the same angle. This indicates that there is no deformation of the crystalline cell induced by the magnetic field and thus no stress anisotropy.

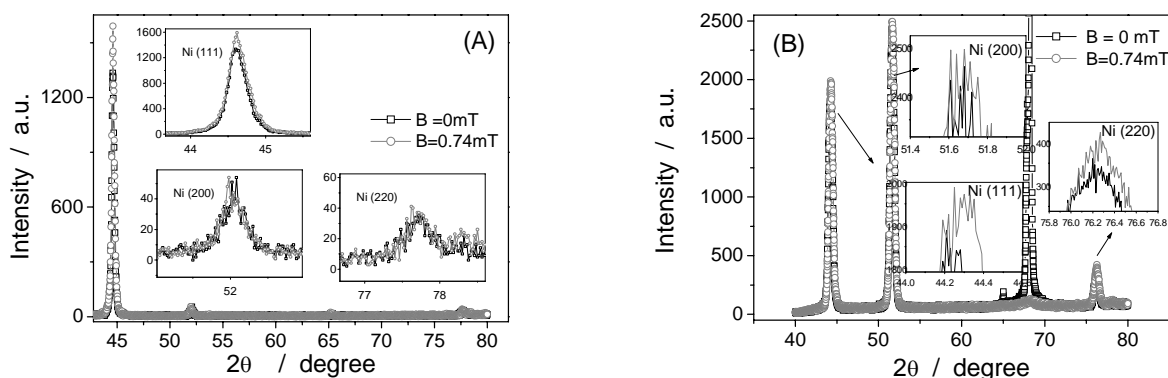


Figure 28. XRD pattern for the Ni layer. Electrolyte used consisted in 1.26M Ni-Sulfamate, 0.04M  $NiCl_2 \cdot 6H_2O$ , 0.32M  $H_3BO_3$ , pH=4. Layers were plated at room temperature and a constant current density,  $j = -5 \text{ mA cm}^{-2}$ , in orientation E. Case (A): total charge imposed was  $1.5 \text{ C cm}^{-2}$ ; case (B): total charge imposed was  $17.5 \text{ C cm}^{-2}$ .

The preferred crystalline orientation index was calculated according to Eq. 14. The preferential plane for Ni growth is (111) for the thin layers. The results obtained in the case of the thick layers are presented in the Table 8.

It can be easily noticed that the preferred plane for thick Ni layers is the (200), followed by the (111) and (220) planes. No effect of the magnetic field on the orientation index could be noticed in the case of the electrodeposited Ni thick layers.

Finch [165] noticed that the deposited layers of a series of metals (Cu, Au, Fe, Ni, Co, Cr, etc) with a thickness less than 1000Å grow epitaxially. In the case of deposited Ni layers the influence of the substrate (Au, Fe, Cu, etc) could be noticed even for higher thicknesses.

Table 8. The orientation index for Ni thick layers electrodeposited from a bath consisting in 1.26M Ni-Sulfamate, 0.04M NiCl<sub>2</sub>\*6H<sub>2</sub>O, 0.32M H<sub>3</sub>BO<sub>3</sub>, pH=4 at charge density, Q= 17.5 C cm<sup>-2</sup>. The magnetic field was imposed perpendicular to the electric current, orientation E (Fig. 10).

<b>B (mT)</b>	<b>M(111)</b>	<b>M(200)</b>	<b>M(220)</b>
<b>0</b>	0.64	2.14	0.43
<b>740</b>	0.67	2.01	0.50

The gold electrode used as substrate in this study has the (111) preferred crystalline orientation (Fig. 27). Therefore, the Ni thin layers grow under the influence of the texture of the substrate (epitaxial growth). For thicker Ni layers, the growth does not depend any more on the substrate texture, but just on the plating conditions, and therefore, the preferred plane for growing becomes the (200) plane. Finch proposed a model that described a transition between stages when the deposit exhibits a perfect epitaxial growth to the state where the texture is independent on the substrate texture. The intermediate state was seen as a mixed state, in which a very fine grain size and random oriented grains co-exist (Finch model) [165-167]. According to Amblard et al. [154], this transition does not exist. They observed in cross section analysis of Ni layers that even on the substrate one can identify atomic clusters that have a different texture than the substrate. Therefore, their model of texture evolution describes a permanent competition between the epitaxial growth and the substrate independent nucleation. This competition should appear in a stage of growth that follows the stage of coalescence. The growth competition should be governed by adsorption of various inhibitors.

In function of the cathode potential and the pH of the solution [98], atomic clusters will form with a specific preferred crystalline orientation that is independent from the substrate orientation. For our experimental conditions, it seems that this preferred orientation is parallel to the (200) plane, that is in agreement with other results reported in the literature



[164]. Therefore, further growth of these crystallites will govern the texture of the whole deposit.

### III.2.2 Magnetic Field Effects on HER and Current Efficiency

The reports about the dependence of the current efficiency of Ni reduction on a magnetic field are also controversial, and usually no explanations for this finding are given. For nickel depositions from a Watts bath Chiba et al. [11] reported an increase of 5 to 10% (conditions  $T=50 \pm 2^\circ\text{C}$ ,  $B=0-0.15\text{T}$ , applied parallel to the electric field), whereas Devos et al. [10] observed a decrease of the current efficiency of some percent (conditions  $T=30^\circ\text{C}$ ,  $B$  up to  $1\text{T}$ , applied perpendicular to the electric field). Saubestre [151] pointed out that the temperature should have a minor effect on current efficiency in comparison to additional convection of the electrolyte.

The HER during metal deposition from aqueous solutions is of special interest in electrochemical reactions [159,168,169]. One of the reasons for this interest is the risk of hydrogen embrittlement that degrades the mechanical properties of metals [170].

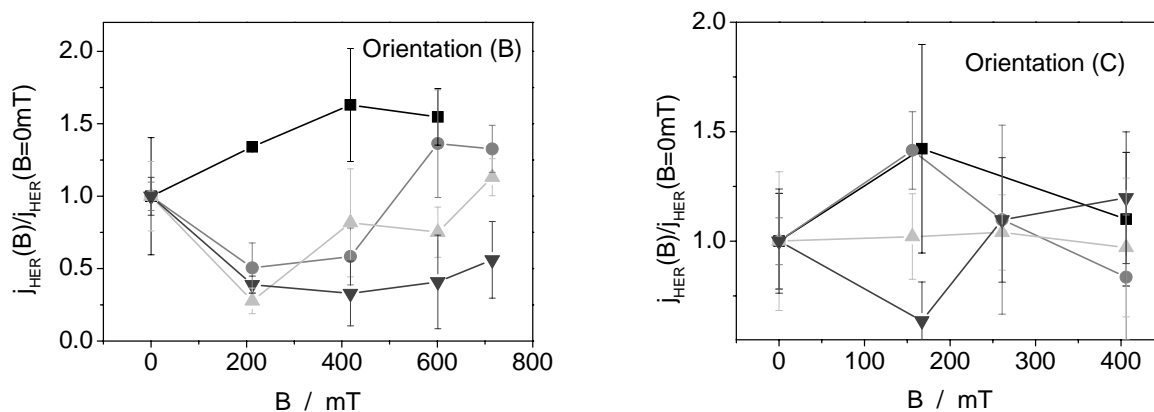


Figure 29. Relative partial current density of HER as function of the applied magnetic field for the electrolytic bath  $1.26\text{M Ni-Sulfamate}$ ,  $0.04\text{M NiCl}_2 \cdot 6\text{H}_2\text{O}$ ,  $0.32\text{M H}_3\text{BO}_3$ ,  $\text{pH}=4$ . Here are presented the cases of depositions in orientations (B) and (C) at different current densities and room temperature. The total charge that passed was  $4.5 \text{ C cm}^{-2}$  ( $- \square -$ :  $j_{\text{total}} = -1 \text{ mA cm}^{-2}$ ;  $- \circ -$ :  $-5 \text{ mA cm}^{-2}$ ;  $- \Delta -$ :  $-15 \text{ mA cm}^{-2}$ ;  $- \nabla -$ :  $-50 \text{ mA cm}^{-2}$ ).

In Fig. 29 the HER for a Ni-sulfamate bath free of surfactants as a function of the applied magnetic field is presented. One can see that the partial current of HER increases with the magnetic field at small current densities ( $1\text{-}5\text{ mA cm}^{-2}$ ) when B and j lines are perpendicular to each other (orientation B), whereas at higher current densities ( $50\text{ mA cm}^{-2}$ ), the partial current of HER seems to decrease slightly with the magnetic field. The HER is mass transport controlled, therefore, the additional convection (natural convection together with the MHD convection) induced in the orientation (B) will increase the rate of HER (see section I.3). The different behaviours of the HER as a function of the applied magnetic field observed at small, respectively high current densities will be described in the following (discussions for Fig. 31). When the magnetic field lines and the electric current are parallel to each other (orientation C), the HER was not be influenced by the magnetic field (Fig. 29).

Nickel was deposited from a sulfamate electrolyte free of surfactant and with surfactant at a relatively small current density in order to check how the surfactant affects the behaviour of the hydrogen evolution in a magnetic field.

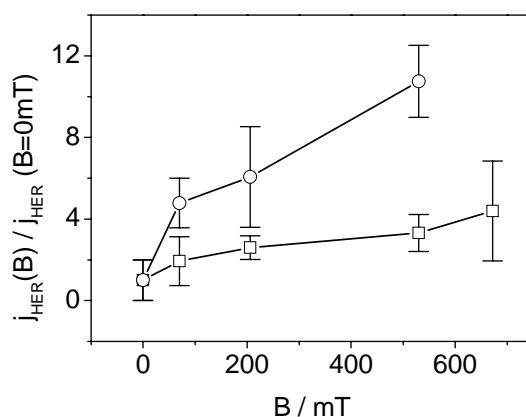


Figure 30. Hydrogen evolution during galvanostatic deposition ( $j_{\text{total}} = -0.5\text{ mA cm}^{-2}$  for 3000 s) from Nickel sulfamate bath (1.26M Ni-Sulfamate, 0.04M  $\text{NiCl}_2 \cdot 6\text{H}_2\text{O}$ , 0.32M  $\text{H}_3\text{BO}_3$ , pH=4) with sulfirol 8 (-○-) and without surfactant (-□-), in orientation E.

The partial current density of the HER increased with the magnetic flux density (Fig. 30). So, the influence of the magnetic field is virtually the same as in the absence of the surfactant (Fig. 29, orientation B). However, when one looks at the absolute values one sees that in the presence of the surfactant the HER increases more strongly. This can be explained with the reduced surface tension in the presence of the surfactant. Bubbles formed at the cathode can detach more easily from the electrode and make space for new bubbles. As a result the partial current density of the HER will increase. The error bars in Figs. 30 and 31

reflect the standard error of the mean, calculated from the ratio between the standard deviation and the square root from the number of measurements, and each data point is the average of four measurements.

Further investigations tried to determine the effect on an external applied magnetic field during Ni deposition from an electrolyte with surfactants, at different current densities. The quartz crystal was fixed perpendicular to the gravitational field for these measurements. The results obtained were similar for both surfactants analysed, therefore just the results for SDS will be discussed.

For a total current density of  $-0.1 \text{ mA cm}^{-2}$  the partial current of the HER increased with increasing magnetic flux density whereas it slightly decreased for a total current density of  $-50 \text{ mA cm}^{-2}$  (Fig. 31).

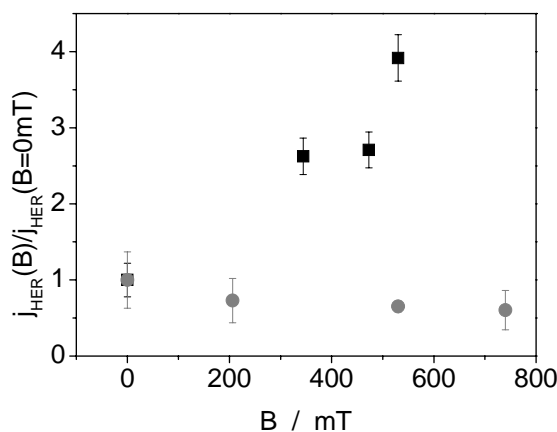


Figure 31. Dependence of the partial current density of the HER,  $j_{\text{HER}}$ , on the magnetic flux density during Ni deposition from a sulfamate bath with surfactant, in orientation E. ( $\square$ :  $j_{\text{total}} = -0.1 \text{ mA cm}^{-2}$ ;  $\circ$ :  $j_{\text{total}} = -50 \text{ mA cm}^{-2}$ )

We proposed a model, which explains the different influence of a magnetic field on the current efficiency at small and large current densities, respectively [171]. It has been shown that the current efficiency of the nickel deposition increases with increasing current density [172,173]. This is because the HER is usually limited by mass transport, whereas the nickel reduction is activation (or mixed) controlled. Therefore, making the potential more negative will result in an increase  $j_{\text{Ni}}$ , while  $j_{\text{HER}}$  remains constant. As a result the current efficiency of nickel reduction increases (Eq. 25).

Under the influence of a magnetic field, both limiting current densities will increase due to the magnetohydrodynamic stirring. The increase will depend on several parameters, such as the magnetic flux density and the concentration [54,174]. As the concentration of nickel

ions is much larger than the proton concentration, we can assume that the nickel deposition is influenced more strongly by the magnetic field (see Fig. 32 for a schematic representation). Because of the activation control the absolute value of the nickel current increases strongly with the overvoltage (or with the total current density in a galvanostatic experiment under steady state conditions). For a potential close to the equilibrium potential of nickel ( $E_1$  in Fig. 32) the MHD effect increases  $j_{\text{HER}}$  more strongly than  $j_{\text{Ni}}$  as seen in Fig. 31 for a  $j_{\text{total}}$  of  $-0.1 \text{ mA cm}^{-2}$ . At a higher polarization ( $E_2$  in Fig. 32)  $j_{\text{HER}}$  and  $j_{\text{Ni}}$  are both under transport control and the effect of the magnetic field is to increase both. In a galvanostatic experiment, where  $j_{\text{Ni}} + j_{\text{HER}}$  must be constant,  $j_{\text{HER}}$  will not change considerably with  $B$  as seen in Fig. 31 for  $j_{\text{total}}$  of  $-50 \text{ mA cm}^{-2}$ .

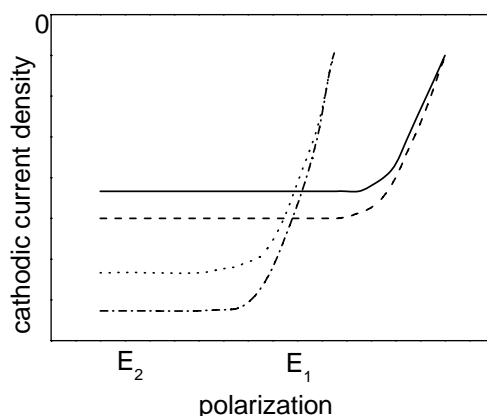


Figure 32. Schematic representation of the effect of a magnetic field on the partial current densities of the Ni reduction,  $j_{\text{Ni}}$ , and the HER,  $j_{\text{HER}}$ . (—) HER without magnetic field, (---) HER in magnetic field, (...) Ni reduction without magnetic field, (-·-·-) Ni reduction in magnetic field. Results published in [171].

As the current efficiency was determined by EQCM one should keep in mind the systematic errors which could be introduced by that measuring technique. First, there could be mass changes which are not related to the electric current. The deposition of  $\text{Ni}(\text{OH})_2$  due to pH changes at the electrode has been reported [10]. The effect can occur at high current densities and will lead to systematically too high values of  $j_{\text{Ni}}$ . However, the effect of a magnetic field on this deposition reaction should be negligible and the ratio  $j_{\text{Ni}}(B)/j_{\text{Ni}}(B=0)$  will not be affected.

Furthermore there are frequency shifts, which are not related to mass changes, such as viscosity [175], surface roughness [176] and temperature effects [177]. The changes of the viscosity will be small and the resulting frequency shifts will be in the order of maximum some ten Hz. It has been shown that the HER can cause a decrease of the electrolyte

temperature near the electrode. Dash reported a decrease of  $1^{\circ}\text{C}$  under a magnetic field of 1.14 T, in the case of chromium electrodes [178]. The quartzes, which were used in this study, had a small temperature coefficient around room temperature and thus temperature effects can be ruled out, too. As will be shown in section III.2.4, there is an influence of the magnetic field on the surface roughness, which manifests itself as an increase of the damping of the quartz. But the damping changes,  $\Delta w$ , are in the order of some kHz while the frequency shift,  $\Delta f$ , is in the order of 100 kHz. It has been shown [179], that the mass calculated from the frequency shift with the Sauebrey equation (Eq. 7, p. 8) is correct as long as  $\Delta w \ll \Delta f$ .

### III.2.3 Magnetic Field Effects on the Potential Transients

When a magnetic field is superimposed during Ni deposition in orientation (E) a Lorentz force will occur in the plane of the working electrode. This force density leads to a gentle stirring of the electrolyte in front of the quartz. When Ni was deposited from a bath with sulfirol 8, a decrease in the polarization concentration was observed [171,180], (Fig. 33). Thus, for a relatively small current density of  $-0.1\text{ mA cm}^{-2}$ , the deposition potential shifted from  $-0.74\text{ V}$  at  $0\text{ T}$  to  $-0.67\text{ V}$  vs. Ag|AgCl at  $0.7\text{ T}$ . At  $-50\text{ mA cm}^{-2}$  a shift from  $-1.46\text{ V}$  (at  $0\text{ T}$ ) to  $-1.40\text{ V}$  vs. Ag|AgCl (at  $0.7\text{ T}$ ) was observed (Fig. 33).

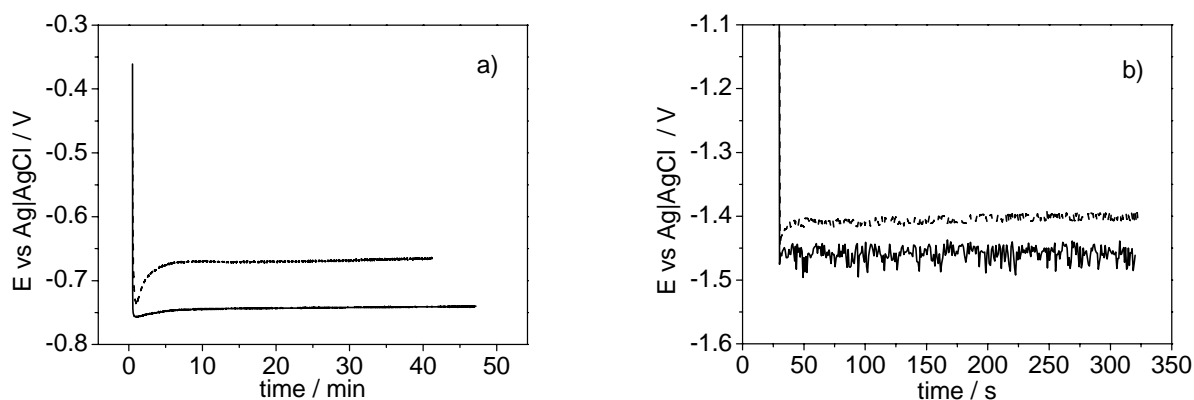


Figure 33. Influence of the magnetic field on the deposition potential during galvanostatic nickel depositions from a Ni sulfamate bath with sulfirol 8, in orientation E. a)  $j = -0.1\text{ mA cm}^{-2}$ , (—)  $0\text{ T}$ , (---)  $740\text{ mT}$ ; b)  $j = -50\text{ mA cm}^{-2}$ , (—)  $0\text{ T}$ , (---)  $740\text{ mT}$

However, when the deposition was carried out from a Ni sulfamate bath free of surfactants as well as from an electrolyte with SDS, the deposition potential shifted to more

negative values in the presence of a magnetic field. Thus, for Ni deposition at  $-0.5 \text{ mA cm}^{-2}$  in orientation E, the potential shifted from  $-0.76 \text{ V vs. Ag|AgCl (0T)}$  to  $-0.80 \text{ V vs. Ag|AgCl (0.7T)}$  for the electrolyte without surfactants and from  $-0.76 \text{ V vs. Ag|AgCl (0T)}$  to  $-0.82 \text{ V vs. Ag|AgCl (0.7T)}$  for a Ni sulfamate bath with SDS. This negative jump of the deposition potential with the magnetic field in orientation E was observed also in the case of Ni-Fe alloy deposition (see section IV.2.1, p.93) and it was attributed to the simultaneous action of the Lorentz force and natural convection. The shift of the deposition potential in anodic direction, which was observed in a magnetic field for Ni sulfamate bath with sulfirol 8, may be caused by the higher incorporation of the surfactant in the deposit. This explanation is supported by the drastic changes in the roughness (section III.2.4) and morphology (Fig. 38) of these layers.

### III.2.4 Morphology Aspects

In Fig. 34 one can see the evolution of the geometrical shape of the nickel crystallites in function of the thickness of the layer. The changes in morphology can be attributed to the changes of the preferred crystalline orientation of the deposits. It was shown that the thin Ni layers grown parallel to the (111) plane, that represented the preferred orientation of the Au substrate [see section III.2.1]. Thus, one can see that the Ni clusters have initially the same morphology as the substrate (Figs. 34b, 35). Pyramidal shape deposit can be observed when the Ni layer becomes thicker (Fig. 34c). XRD analysis proved that these layers were preferentially oriented parallel to the crystallographic plane (200).

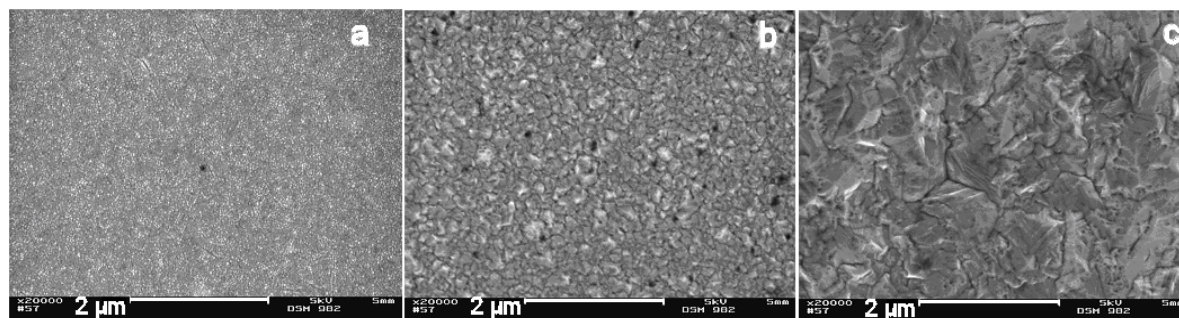


Figure 34. SEM images. a) the morphology of the Au electrode used as the substrate; b) thin Ni layer ( $0.5 \mu\text{m}$ ); c) thicker Ni layer ( $6 \mu\text{m}$ ). Ni deposition was done at room temperature, in  $B=0\text{T}$  and at a constant current density,  $j = -5 \text{ mA cm}^{-2}$ , from  $1.26 \text{ M Ni-Sulfamate}$ ,  $0.04 \text{ M NiCl}_2 \cdot 6\text{H}_2\text{O}$ ,  $0.32 \text{ M H}_3\text{BO}_3$ ,  $\text{pH}=4$ , in Orientation E.

According to Amblard et al. [154], the growth of Ni layers involves four processes that

are in permanent competition:

- a) layer-by-layer growth, that will generate an epitaxial layer
- b) pyramidal growth, induced by screw dislocations (these are defects in the crystal structure that will facilitate a spiral type growth)
- c) pyramidal growth on micro-twins (they observed that usually ten or twenty tetrahedral crystals grow together, making a twinned structure in which every crystal tries to preserve its initial symmetry)
- d) poly-crystalline non-epitaxial growth induced by independent nucleation.

In function of the crystalline orientation of the substrate, a specific type of growth can be found. For the (111) oriented substrate, they predict that the “c” type of growth can overwhelm rapidly the epitaxial growth. Our experimental results are in good agreement with their model. Thus, thicker Ni layers had a pyramidal shape in comparison to thin epitaxial layers, grown on (111) oriented Au electrode (Fig. 34).

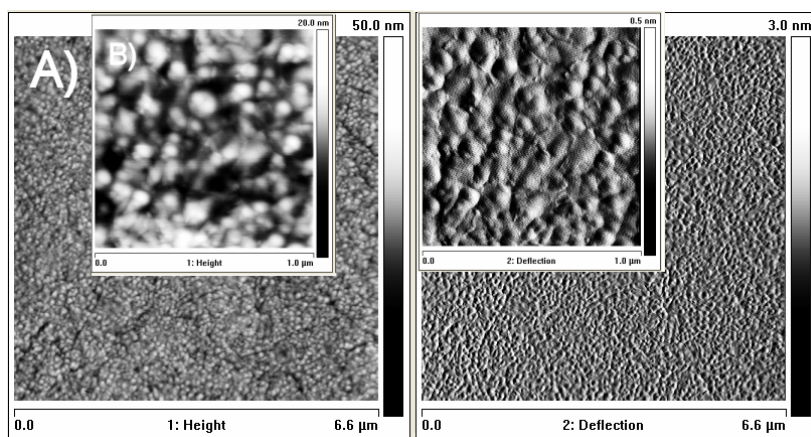


Figure 35. AFM images of the Au substrate. A) scan size  $6.6\mu\text{m} \times 6.6\mu\text{m}$ ; B) scan size  $1\mu\text{m} \times 1\mu\text{m}$ . In the left is the height image and to the right, the deflection image

It is well known that the surfactants are adsorbed at the cathode during the deposition [181-183], thus they can block the active sites and modify the crystal growth mode and the morphology of the deposited layers [182]. In the Fig. 36, the topography of Ni layers electrodeposited from a sulfamate bath free of surfactants and with surfactants is presented. The layers deposited in the presence of SDS look similar to those deposited without any surfactant, when no magnetic field was superimposed (Fig. 36a,c). The last remark is in perfect agreements with other data reported in the literature: the SDS surface coverage for different SDS concentrations in the electrolyte was found to be very small in the case of Zn deposition in comparison to surface coverage of other additives [182].

Ni layers deposited from a sulfamate bath with sulfirol 8 present larger crystallites in comparison to those deposited from a pure sulfamate bath or from the sulfamate bath with

SDS (Fig. 36).

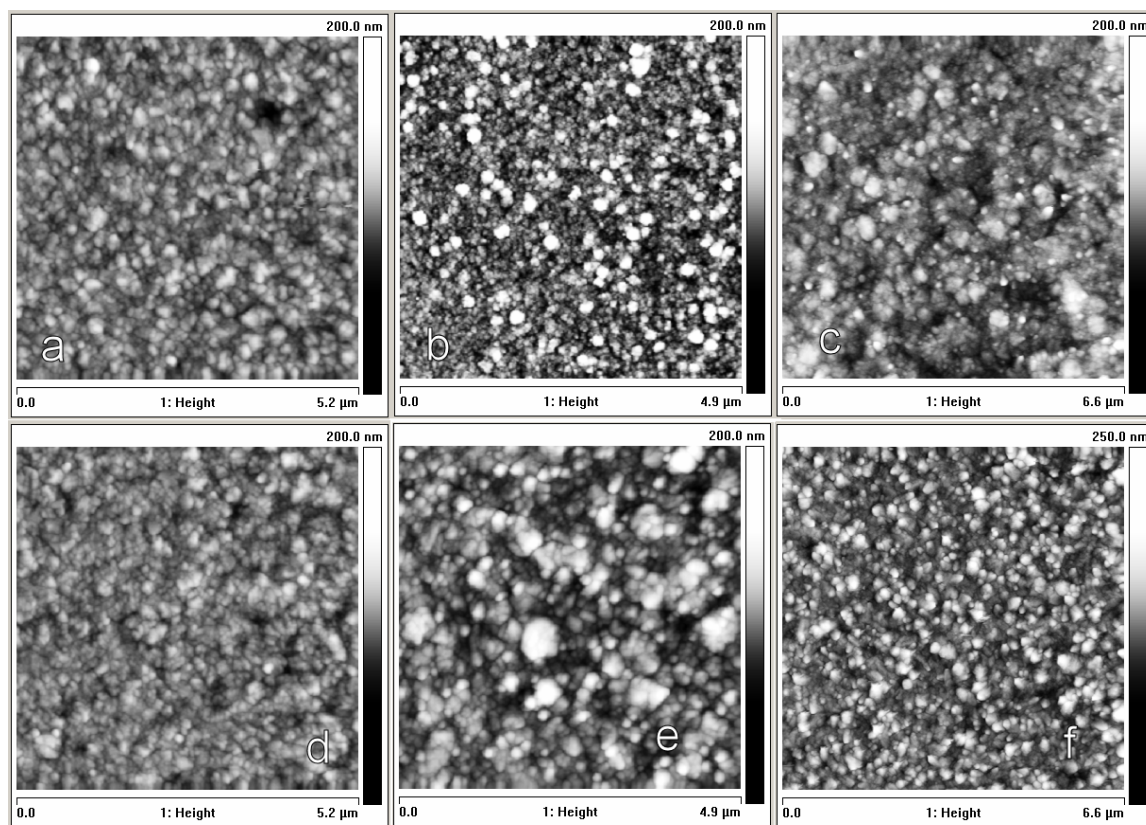


Figure 36. AFM height images for Ni layers deposited 3000s at  $j = 0.5 \text{ mA cm}^{-2}$  from Ni sulfamate bath (1.26M Ni-Sulfamate, 0.04M  $\text{NiCl}_2 \cdot 6\text{H}_2\text{O}$ , 0.32M  $\text{H}_3\text{BO}_3$ , pH=4), in Orientation E. (a,d), bath free of surfactants, (b,e) bath with sulfirol 8, (c,f) bath with SDS. (a,b,c) describe layers deposited in  $B=0\text{T}$ , and (d,e,f) the layers deposited in  $0.7\text{T}$ .

EDX analysis did not prove the existence of sulfate or oxygen atoms in the Ni deposited layers from the sulfamate bath with surfactants. The only elements identified were Ni (more than 99 at %) and Au (0.4-1 at%). The surface coverage with the surfactants can be calculated according to the mechanism proposed by Madore and Landolt [184] during potentiostatic depositions. As all the depositions that we performed were done in the galvanostatic mode, and because the electrochemical cell is not a linear system (if one doubles the potential the current will not be double), the mechanism proposed by Madore and Landolt can not be applied. One just can suppose that the surface coverage of the cathode with sulfirol 8 is higher in comparison to that of the SDS.

The potential differences obtained for a galvanostatic deposition at  $-0.5 \text{ mA cm}^{-2}$  from a Ni sulfamate bath free of surfactants and with surfactants were very small. For example, the potentials for a pure Ni sulfamate bath lies around 754-765mV vs.  $\text{Ag|AgCl}$ , while for a bath with sulfirol 8 lies between 762-771mV vs.  $\text{Ag|AgCl}$  and between 765-768mV vs.  $\text{Ag|AgCl}$



for a bath with SDS.

#### Magnetic Field Effects on Morphology and Roughness of the Layers

It was shown that the partial current of hydrogen in Ni electrodeposition from a sulfamate bath increases with the magnetic flux density when the deposition is made at low current densities and slightly decreases at higher current densities (Figs. 29,31). The hydrogen bubbles can stay on the electrode surface long enough to influence also the morphology of the deposits. Higher current densities induce higher Lorentz forces and thus stronger convection when the electrochemical cell has the orientation E, which can influence the roughness more strongly and the structure of the layers. Therefore, the Ni morphology obtained in the case of electrodeposition at low and high current densities will be treated in the following separately.

##### a) case of low current densities

The morphology of Ni layers electrodeposited at relatively low current densities ( $-0.5\text{mA cm}^{-2}$ ) in a magnetic field, from Ni sulfamate bath free of surfactants or with surfactants is presented in Fig. 36 d,e,f. One can see that the magnetic field does not change the morphology of the layers deposited from a bath free of surfactants (Fig. 36 a, d), at low current densities. The layers deposited from a bath with surfactant seem to present some coarser grains when they were deposited in a magnetic field (Fig. 36 b,e; c,f), and this effect seems to be more strong in the case when sulfirol 8 was used. More uniform layers were obtained in the case when SDS was used in comparison to the layers deposited from a bath with sulfirol 8.

The number of grains and the mean grain size of the Ni layers deposited from a bath with or without surfactants were calculated with the software from Digital Instruments (Table 9). The number of grains identified by the DI software for the Ni layers deposited from a sulfamate bath free of surfactants increases slightly in a magnetic field. The same increasing tendency with the magnetic field of the number of grains can be noticed when the Ni sulfamate bath with SDS was used. As a consequence, the mean grain size decreases in a magnetic field for these two baths. When sulfirol 8 was used, the number of grains of the layers deposited in a magnetic field is much smaller than that obtained in absence of a magnetic field. The mean grain size of the Ni layers deposited from a bath with sulfirol 8 does not vary significantly with the magnetic field.

With the particle analyse function of the DI software a histogram can be obtained, that shows the distribution of the particles in function of their height and diameter, which allows to verify the dimensions (area) of the particles counted. In B=0T, most of the particles (36) of the Ni layers deposited from a sulfamate bath with sulfirol 8 had a diameter of 10.7nm, a length of 13.4nm and a width of 13.4 nm. In B=0.7T, the diameter of the most frequently counted particles was 28.3nm, the length between 34.2 and 42.4 nm and the width between 13.4 and 24.3. These dimensions give an area of 89.8nm<sup>2</sup> for the most particle counted in B=0T and an area between 270.2 and 630.5 nm<sup>2</sup> for the particles counted in B=0.7T. The later observation certifies that coarser layers were obtained in a magnetic field for the Ni layers deposited from a sulfamate bath with sulfirol 8.

Table 9. Number of grains and the mean grain size for the Ni layers deposited from a Ni sulfamate bath with or without surfactants at  $j=-0.5\text{mA cm}^{-2}$ , in function of the magnetic flux density, in orientation E (corresponding to Fig. 36).  $R_q$  represents the standard deviation of the height values and characterizes the surface roughness.

bath	B (T)	Number grains		Grain size mean (nm <sup>2</sup> )		$R_q$ (nm)
		area selected	whole area	area selected	whole area	
<b>sulfamate</b>	<b>0</b>	63	146	885	36451	9.6
<b>sulfamate</b>	<b>0.7</b>	71	161	610	20944	9.2
<b>+ sulfirol 8</b>	<b>0</b>	21	106	595	7863	8.5
<b>+ sulfirol 8</b>	<b>0.7</b>	5	51	648	7203	16.3
<b>+SDS</b>	<b>0</b>	85	243	644	30442	12.2
<b>+SDS</b>	<b>0.7</b>	105	291	497	18416	17.6

The roughness of the deposited layers increased in a magnetic field when a surfactant was used, and this effect was stronger for the electrolytic bath with sulfirol 8 (Table 9). No significant changes of the roughness were observed for a sulfamate bath free of surfactant (Table 9, Fig. 37).

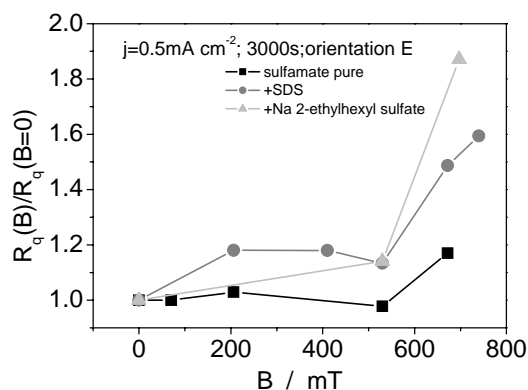


Figure 37. The relative change of the roughness of the Ni layers electrodeposited from a sulfamate bath with or without surfactants. The depositions were made in the galvanostatic mode, at  $j = -0.5 \text{ mA cm}^{-2}$  for 3000s, in the orientation E. The roughness values plotted here are average values obtained from at least three independent samples and at each layer, three determinations at different locations at the surface were made.

b) case of higher current densities

Figure 38 presents the morphology of Ni layers obtained from a sulfamate bath where a surfactant (sulfirol 8) was used.

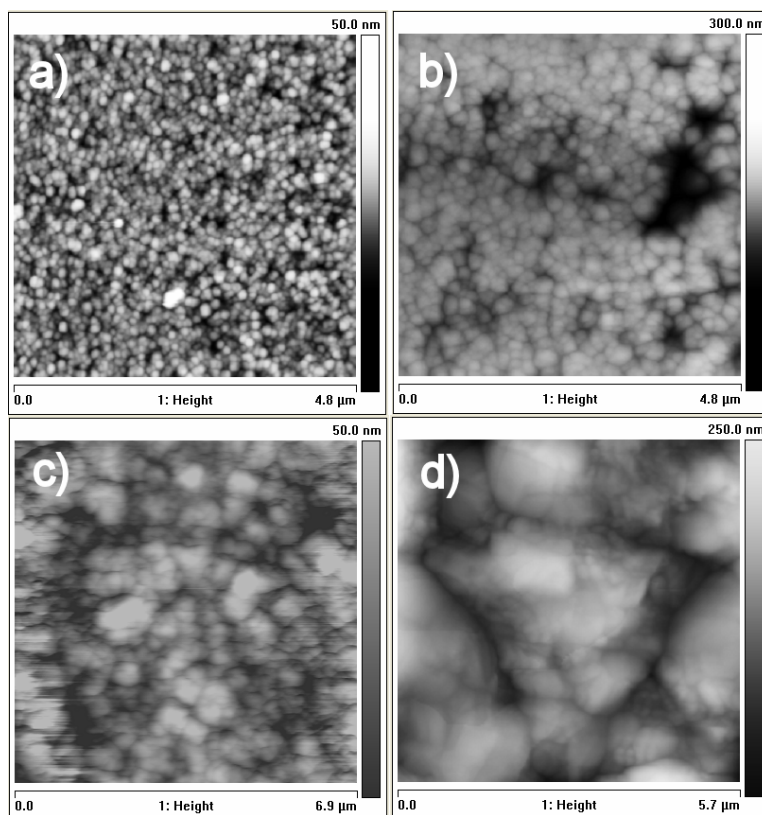


Figure 38. Ni layer deposited from a bath containing 1.26M Ni-Sulfamate, 0.04M  $\text{NiCl}_2 \cdot 6\text{H}_2\text{O}$ , 0.32M  $\text{H}_3\text{BO}_3$ , 0.24 mM sulfirol 8, pH=4. Deposition was done at  $j = -50 \text{ mA cm}^{-2}$ , and the corresponding charge density was  $0.5 \text{ C cm}^{-2}$  (for a,b,

thickness around 0.2 $\mu\text{m}$ ) and 15C cm<sup>-2</sup>(for c,d, thickness around 5 $\mu\text{m}$ ). (a,c) layers deposited in B=0mT; (b,d) layers deposited in B= 0.74mT. Orientation E.

One can see in Figure 38 that in the case of thin layers of 0.2  $\mu\text{m}$  thickness, the deposited particles present an almost hemispherical geometrical shape, while the thicker layers (with a thickness of 5  $\mu\text{m}$ ) start to develop a pyramidal shape. It seems that the presence of surfactants does not dramatically influence the evolution of the geometrical shape of the deposited layers with the thickness. However, it has to be mentioned that the superposition of a magnetic field influences significantly the size of the deposited grains. This aspect will be discussed in more detail in the following (Table 10).

Table 10. Number of grains and the grain size mean for the Ni layers deposited from a Ni sulfamate bath with 0.24 mM sulfirol 8 at  $j=-50\text{mA cm}^{-2}$ , in function of the magnetic flux density, in orientation E.  $R_q$  represents the standard deviation of the height values and characterizes the surface roughness. Data were calculated for layers in Fig. 38.

Thickness ( $\mu\text{m}$ )	B (T)	Number grains		Grain size mean ( $\text{nm}^2$ )		$R_q$ (nm)
		area selected	whole area	area selected	whole area	
0.2	0	9 $\pm$ 2	163 $\pm$ 45	751 $\pm$ 182	11053 $\pm$ 1214	5.5 $\pm$ 1.5
0.2	0.7	4 $\pm$ 1	58 $\pm$ 7	1502 $\pm$ 77	13699 $\pm$ 1004	13.9 $\pm$ 0.5
5	0	5 $\pm$ 1	23 $\pm$ 1	535 $\pm$ 206	39645 $\pm$ 24408	13.6 $\pm$ 1.5
5	0.7	3 $\pm$ 1	21 $\pm$ 1	1440 $\pm$ 986	85717 $\pm$ 49306	34.5 $\pm$ 2.3

As mentioned before (see Table 9 and corresponding discussion), the number of grains decreases in a magnetic field and at the same time their area increases when the deposition is carried out from a sulfamate bath with sulfirol 8, in orientation E. These effects are stronger at higher current densities than at low current densities (Figs. 36,38).

At higher current densities the roughness of the layers increases strongly with the magnetic flux density in orientation E (Table 10). Each  $R_q$  value from Table 10 is the average of four independent layers, and at each layer, four determinations at different locations at the surface were made.  $R_q$  was calculated from the AFM height data as the standard deviation of the Z values for a scan size of 6.5 $\times$ 6.5  $\mu\text{m}^2$ .

However, one should take into account that the surface morphology, roughness and the grain size of the deposits depend strongly on the electrolyte composition and on condition of deposition [8,13]. Previously, Bund et al. [185] investigated the effect of a static magnetic

field up to 1T (parallel to the electrode) on the grain size of potentiostatically deposited Ni layers. It was found that a larger amount of fine grained material was formed in the presence of the magnetic field. Furthermore, a general correlation of the grain size with surface roughness is difficult [186,187]. For copper electrodeposition Hu and Wu [187] showed that an increase of the mean grain size does not necessary induce an increase of the roughness of the deposit.

It has been shown that the surface roughness of the layers,  $R_q$ , increases with the scan size and approaches a limiting value [188,189]. In a separate series of measurements we made sure that our scan size ( $6.5 \times 6.5 \mu\text{m}^2$ ) is large enough to obtain the saturation value of  $R_q$ .

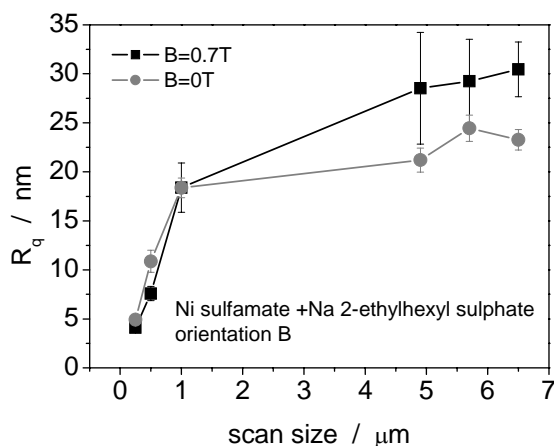


Figure 39. Dependence of the roughness of Ni layers,  $R_q$ , on the scan size. The deposition was carried out from a Ni sulfamate bath with sulfirol 8 at  $j = -50 \text{ mA cm}^{-2}$ , for 300s, in orientation B.

The roughness depends on the length scale on which it is observed (Fig. 39). The imaging of the samples was done mainly for a  $6.5 \mu\text{m} \times 6.5 \mu\text{m}$  scan size.

It was pointed out that the roughness of the layers depends strongly on the electrolyte composition. The following graphs present the roughness evolution in function of the magnetic flux density values for Ni layers obtained in a galvanostatic deposition at different current densities from a sulfamate bath free of surfactants (Fig. 40).

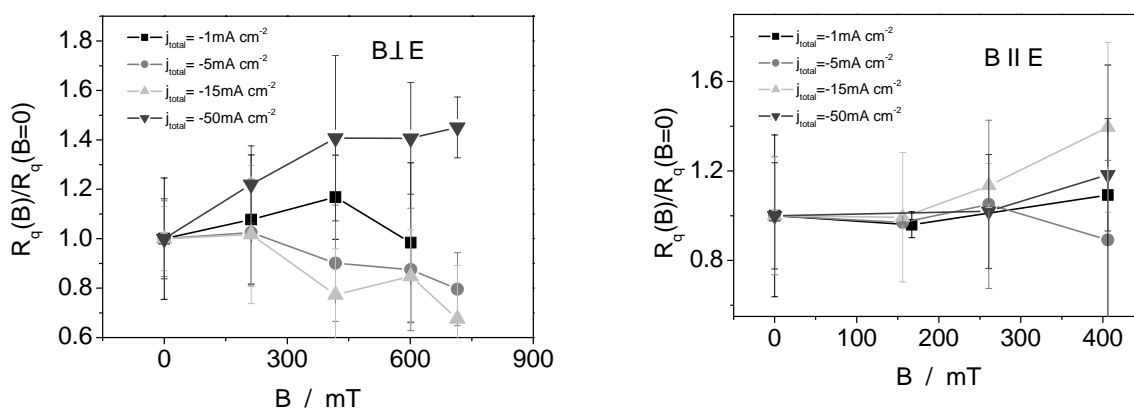


Figure 40. Roughness evolution of Ni layer deposited from a bath containing 1.26M Ni-Sulfamate, 0.04M  $\text{NiCl}_2 \cdot 6\text{H}_2\text{O}$ , 0.32M  $\text{H}_3\text{BO}_3$ , pH=4, in function of the magnetic field. Depositions were done at different current densities, but with a constant charge density of  $4.5 \text{ C cm}^{-2}$ . Orientations investigated here are B (left graph) and C (right graph).

It was shown that the roughness of Ni layers electrodeposited from a sulfamate bath with sulfirol 8 increases with the magnetic field, when the magnetic field is applied perpendicular to electric current (Figs. 36,38, [190]). However, in the case of a sulfamate bath free of surfactants, no strong changes in the roughness values were noticed under these conditions (Fig. 40, orientation B). For the layers deposited at higher current densities an increasing tendency of the roughness with the magnetic field was observed. When the depositions were made at low current density, a decreasing tendency of the roughness with the magnetic field is observed. When comparing the results obtained from the sulfamate bath free of surfactants with the results from the sulfamate bath with sulfirol 8 in the case that the magnetic field was applied perpendicular to the electric current, one should take into account the different orientation of the working electrode. Thus, in one case, the Lorentz force and the natural convection act in the same direction, inducing a stronger convection of the electrolyte (orientation B), while in the other case the Lorentz force is in the plane of the electrode and the natural convection acts perpendicular to the electrode (orientation E). Different flow profiles will be induced in the two orientations, which will influence the morphology and roughness of the deposited layers. Furthermore, the possibility of the surfactants to be adsorbed on the cathode should be taken into account, which will induce changes in the morphology and roughness of the deposits.

When the magnetic field lines were parallel to the electric current (Fig. 40, orientation C), the roughness values did not change with the magnetic field. This proves once more the

statement that the Lorentz force is the main force that influences the deposition process.

A decrease in the absolute values of the roughness with increasing the current density was observed for the Ni layers obtained from a sulfamate bath free of surfactants. This tendency was independent of the intensity or orientation of the magnetic field for a vertical working electrode. Thus, the roughness  $R_q$  lies around  $23.2 \pm 0.7$  nm for the Ni layers deposited at  $-1 \text{ mA cm}^{-2}$  in  $B=0$  T and around  $9.4 \pm 0.5$  nm for the layers deposited at  $-50 \text{ mA cm}^{-2}$ . This decrease in roughness with increasing current density was observed in the case of Ni-Fe alloy deposition, too (see section IV.4, p.103), for current density between  $-1$  and  $-25 \text{ mA cm}^{-2}$ , in the case that a vertical working electrode was used.

In [171] a mechanism was proposed that can explain the correlation of the surface roughness and the magnetic flux density. It is based on the interplay of magnetohydrodynamic convection with the concentration profiles and the hydrogen bubbles. In general, surface roughness develops due to uneven nucleation and crystal growth [111]. Chen and Jorne applied the Mullins-Sekerka morphological stability theory to identify the major factors that influence the evolution of surface roughness [191]. According to them, one of the most important factors that favour morphological instabilities (and thus a high surface roughness) is the increase of the concentration gradient at the electrode|electrolyte interface. Because the MHD effect increases the concentration gradient, the presence of a magnetic field (perpendicular to electric field) can increase the surface roughness. From our results, we saw that when surfactants are used, the roughness of the deposited layers increases stronger with the magnetic field than in the bath without surfactants. Another interesting fact is that the roughness of the layers deposited from a bath free of surfactants increases just at higher current density ( $-50 \text{ mA cm}^{-2}$ ). This can be due to the fact that the Lorentz force increases at higher current density, inducing a stronger effect.

The presence of the hydrogen bubbles was mentioned to induce changes in the roughness and in morphology. This effect is especially obvious in orientation E, when the bubbles can stay on the electrode surface long enough, inducing rougher layers. Furthermore, the interplay between the Lorentz force and the natural convection proved to have an important role in the morphology and roughness of the electrodeposited Ni layers.

Qualitative in situ information about the surface roughness can be taken from the EQCM data (see section I.2, p.8 and [48-50]). Some typical damping information of the quartz crystal is presented in Fig. 41. Figure 41a represents the changes in the full width at half maximum ( $\Delta w$ ) of the resonance curve of the quartz for a deposition current of  $-50 \text{ mA cm}^{-2}$ . In the early stages of the deposition process, the damping becomes negative. This finding

can be explained with a smoothing of the surface. For the relatively small current density of  $-0.1 \text{ mA cm}^{-2}$ , the damping increases continuously (Fig. 41b). Note that Fig. 41b presents the damping increase as the change of the motional resistance of the quartz crystal. For both current densities the damping increases with the deposition time (i.e. layer thickness). The effect of a magnetic field (applied perpendicular to electric field) is to increase the damping more strongly. The damping increase indicates that the surface becomes rougher, which is in perfect agreement with the ex-situ AFM information (Fig. 38). The reason for the spikes in the damping (obtained just in orientation E) will be discussed in more detail in the section IV.4, p.102.

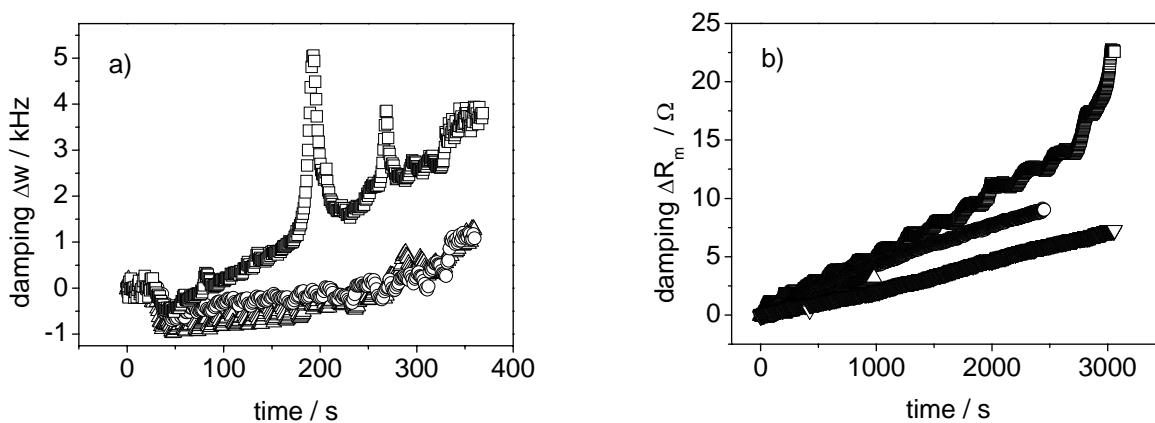


Figure 41. Change of the damping of the EQCM (a: represented as the full width at half maximum,  $\Delta w$ ) during Ni deposition at  $-50 \text{ mA cm}^{-2}$  for different magnetic flux densities ( $\triangle$ ) 0 mT, ( $\circ$ ) 206 mT, ( $\square$ ) 740mT. (b: represented as the motional resistance,  $\Delta R_m$ ) during Ni deposition at  $-0.1 \text{ mA cm}^{-2}$  for different magnetic flux densities ( $\nabla$ ) 0 mT; ( $\triangle$ ) 206 mT; ( $\circ$ ) 410 mT; ( $\square$ ) 530 mT. Depositions were done in orientation E, from a Ni sulfamate bath with sulfirol 8.

### III.2.5 Magnetic Properties of Electrodeposited Ni Layers

The nickel ions in the electrolyte are paramagnetic species. Once they are reduced to metallic nickel they begin to form a ferromagnetic layer with a certain magnetization, even in the absence of an external magnetic field. The orientation of this magnetization is the result of the energy balance between the exchange energy, the dipolar energy, the magneto-crystalline energy and the magnetoelastic energy (see section I.3, p.11). An external magnetic field which is applied during the deposition of the layer might induce some



magnetic anisotropy. In the following we shortly discuss which terms might cause a magnetic anisotropy in the case of nickel layers.

The dipolar energy leads to a shape anisotropy that favours a magnetization along the larger dimension of a ferromagnetic body. The magneto-crystalline anisotropy favors a magnetization along the easy axis of magnetization. Nickel has a fcc crystalline structure and its easy axis is [111] and the hard axis is [100]. In the case of nickel, this anisotropy can be neglected, especially if the orientation of the grains is isotropic. The magneto-elastic energy is induced by the deformation of the crystalline cell and can result in stress anisotropy. X-ray diffractograms (Fig. 28) did not show any shift of the reflections of nickel if the layers were deposited in a magnetic field. Therefore, we can rule out this source of anisotropy.

From all the terms that may be a source of anisotropic magnetic properties, the most important in our case is the dipolar one. Hysteresis curves (Fig. 42B) showed no in-plane anisotropy for nickel layers, deposited in a magnetic field and no relevant dependence of the coercive field,  $H_c$ , on the degree of rotation in the plane of growth was found (Fig. 42A). The higher values of  $H_c$  seen in Fig. 42 for the sample prepared in the magnetic field are due to a higher layer thickness. The slope of the magnetization curve at the coercive field  $(dM/dH)H_c$  (differential susceptibility) measured in the vertical plane also showed no anisotropy. In conclusion it can be stated that no anisotropy of the magnetic properties was found.

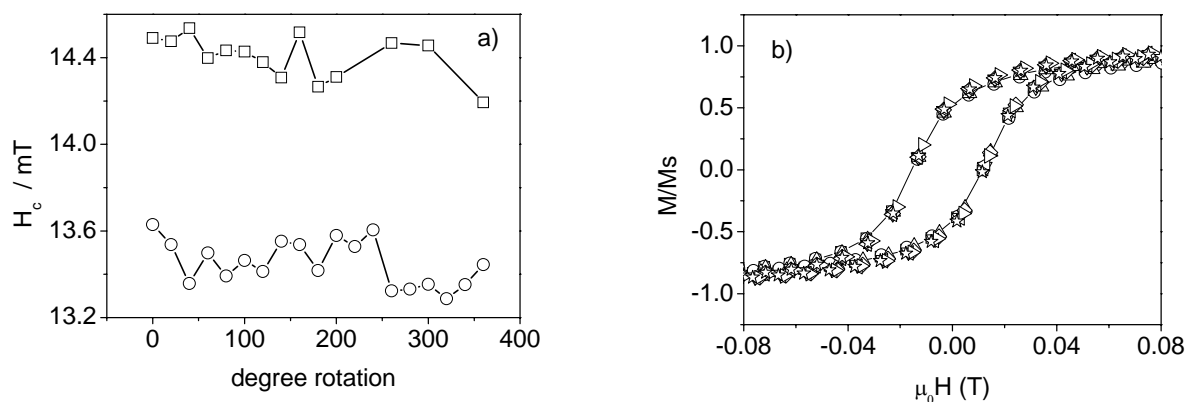


Figure 42. a) Coercive field strength for Ni layers deposited at  $-3.5 \text{ mA cm}^{-2}$  in absence of a magnetic field (○, total charge  $Q=7.2 \text{ C cm}^{-2}$ ) and at 740 mT, (□,  $Q=10.4 \text{ C cm}^{-2}$ ), respectively. b) Reduced magnetization in the case of nickel layer deposited with an external superimposed magnetic field, 0.7 T. (□) 0 degree; (○) 20 degree; (▲) 40 degree; (▼) 60 degree; (◇) 80 degree; (◄) 100 degree; (►) 120 degree; (☆) 140 degree. The magnetization values were corrected for the contribution of the VSM holder and of the copper substrate on which the Ni layer was deposited. Depositions were done in orientation E from a Ni sulfamate bath with sulfirol 8. Measurements of the magnetic properties were made at room temperature.

Table 11. Dependence of some selected magnetic properties of nickel layers on the magnetic flux density applied during the electrodeposition.				
angle between sample and H field	Magnetic field (B) superimposed during deposition /mT	Slope at $H_c$ /( $\mu\text{A m}^2 \text{T}^{-1}$ )	$M_s$ /( $\mu\text{A m}^{-2}$ )	$M_r$ /( $\mu\text{A m}^{-2}$ )
0°	0	22.4	46.3	22.3
	740	16.6	34.0	16.9
90°	0	23.0	50.7	23.2
	740	14.9	35.6	14.9

However, the absolute values of  $(dM/dH)H_c$ , the magnetization of saturation,  $M_s$  and the residual magnetization (retentivity),  $M_r$ , decreased by approximately 10% for the sample deposited in a field of 740 mT (Table 11). It is known that changes in morphology of a layer will induce changes in the magnetic properties [192-194]. In our case, the magnetic field changes the surface roughness (see III.2.d) of the deposited nickel (and maybe slightly the layer thickness via the influence on the current efficiency), thus inducing slight changes of the coercive field, the saturation magnetization and the residual magnetization.

## IV. Ni-Fe Alloy codeposition in a Magnetic Field

The following section is dedicated to Ni-Fe alloy codeposition. In the beginning, the initial stages that occur in Ni-Fe codeposition are presented (IV.1). In a galvanostatic deposition experiment, the variation of the total current induces changes of the content of the alloys. These effects will be presented for two Ni-Fe alloys, with different Fe content (IV.2.1, p.93). The effects induced by an external magnetic field on the alloy composition (see IV.2.2, p.97), HER (see IV.3, p.100), morphology and roughness of the deposited layers (IV.4, p.103) will be discussed. Finally, the dependence of the preferred crystalline orientation with the intensity of a magnetic field or of an applied current density/potential will be presented (IV.5, p.107).

### IV.1 Initial Stages of Ni-Fe Alloys codeposition

Cyclic voltammograms with a scan rate of  $1 \text{ mV s}^{-1}$  and  $10 \text{ mV s}^{-1}$  were performed in Ni sulfate or Fe sulfate baths, in order to determine the region where the HER and the single metal deposition occurs (Fig. 43). Then a cyclic voltammogram in an electrolyte that contains both Fe and Ni ions was performed.

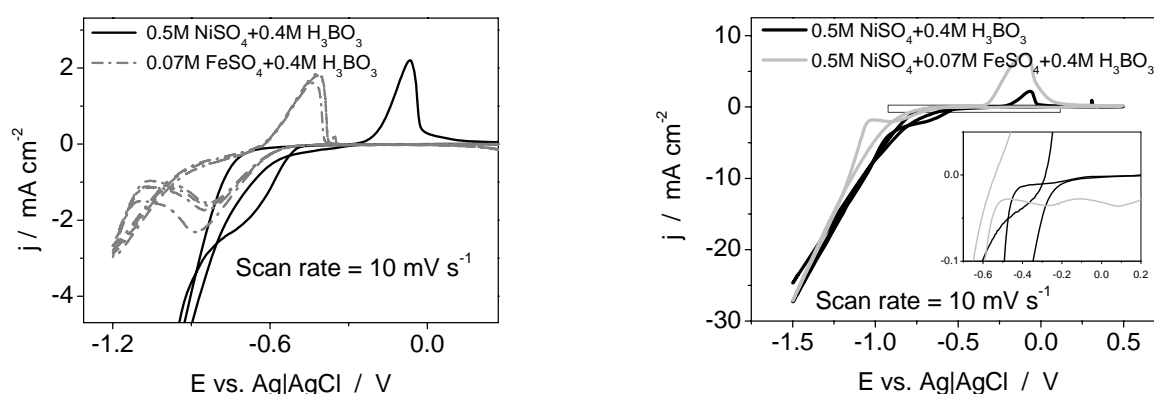


Figure 43. Cyclic Voltammograms ( $10 \text{ mV s}^{-1}$ ) for orientation E in absence of a superimposed magnetic field. Baths 1, 2 and 3 at the pH 2.0 used were used here (composition of the electrolytes is described in Table 1, p.39).

As one can see in Fig. 43, the cyclic voltammograms obtained for electrodeposition of Ni

and Ni-Fe alloy look similar. Ni deposition starts around -0.9V vs. Ag/AgCl and Ni-Fe alloy codeposition begins at -1V vs. Ag/AgCl. The dissolution peaks occur at -0.06V for Ni and -0.09V for Ni-Fe, but the current density corresponding to the dissolution of Ni-Fe alloys reaches higher values than that of Ni dissolution ( $j=2.2 \text{ mA cm}^{-2}$  for Ni and  $7.4 \text{ mA cm}^{-2}$  for Ni-Fe). The cyclic voltammogram obtained in the electrolyte 2 (see Table 1, p.39) were different than those observed for electrolytes 1 or 3 (see Table 1, p.39). Iron deposition starts at -1.12V vs. Ag/AgCl, while the Fe dissolution peak appears at -0.4V. The values of the Fe dissolution current density are around  $1.7 \text{ mA cm}^{-2}$  (Fig. 43).

The partial current due to hydrogen evolution was calculated as the difference between the total current density and the partial current due to metal or alloy deposition. The later was estimated from differentiating the mass density data, obtained by the EQCM (Eq. 7, p.8 and Eq. 24, p.41). The cyclic voltammograms taken at  $1 \text{ mV s}^{-1}$  were considered for the evaluation of the partial current of the HER (Fig. 44).

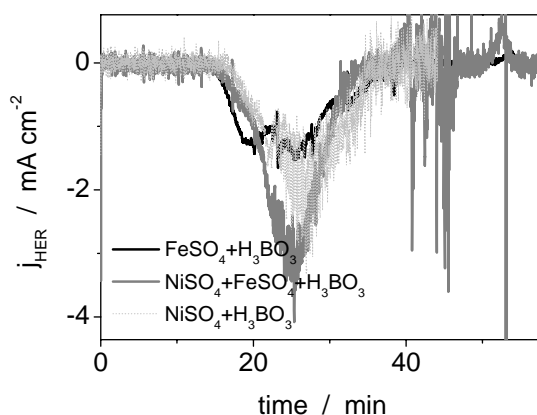


Figure 44. Partial current of the HER calculated from the cyclic voltammograms ( $1 \text{ mV s}^{-1}$ ) from different electrolytes (bath 1, 2 and 3, pH=2, see Table 1, p.39). The cell had the orientation E. The most cathodic potential applied during the cyclic voltammograms was -1.2V vs. Ag/AgCl.

The derivative of a graph is taken by averaging the slopes of two adjacent data points, according to the expression  $\frac{1}{2}[(y_{i+1}-y_i)/(x_{i+1}-x_i) + (y_i-y_{i-1})/(x_i-x_{i-1})]$ . Normally, the derivative of a graph produces more noisy data in comparison to the original graph. This is due to the fact that no filter and no smoothing of the data are made after the differentiating procedure. A strong noise level can be seen in Fig. 44, which corresponds to the partial current of the HER calculated for the Ni-Fe alloys electrodeposition. Ni-Fe alloys present a high internal stress, which induced often the exfoliation of the deposited layer (after it reached a specific

thickness). The detaching of the Ni-Fe layers from the working electrode induces strong variation in the resonance frequency of the quartz crystal and thus, strong changes of the additional mass on the quartz crystal. As a final effect, the partial currents obtained by differentiating the mass became very noisy when the exfoliation of the deposits occurred.

Horkans underlined that the hydrogen overpotential is lower on Fe than on Ni in the pH range from 2-3 [195]. Therefore, slightly higher hydrogen current is observed in the baths containing  $\text{FeSO}_4$ . One can see in Fig. 44 that our results confirm the previous observations of Horkans. The partial current due to HER is bigger for the electrolyte that contained both Ni and Fe species, in comparison to the electrolytes that contained just Ni or just Fe ions. The smallest partial current of HER was obtained in the pure  $\text{FeSO}_4$  electrolyte. This can be due to the low concentration of this electrolyte in comparison to the other bath investigated.

Figure 45 presents the mass changes that correspond to the cyclic voltammograms described in Fig. 43. One can see that the Fe layer is very thin: the variation of mass is just  $6 \mu\text{g cm}^{-2}$ . The Fe deposit dissolves completely in the anodic scan which is contrast to the Ni or Ni-Fe alloy layers. The Ni layer passivates quickly, which results in a small dissolution peak, while the Ni-Fe alloy dissolves to a larger extent compared to the pure Ni layer before it passivates. The decreasing tendency of the mass in the case of Fe electrodeposition, which leads even to negative values, can be ascribed to hydrogen bubbles trapped on the electrode surface, that will induce an increase of the resonance frequency of the quartz crystal and thus an apparent decrease of the mass (see also Fig. 47).

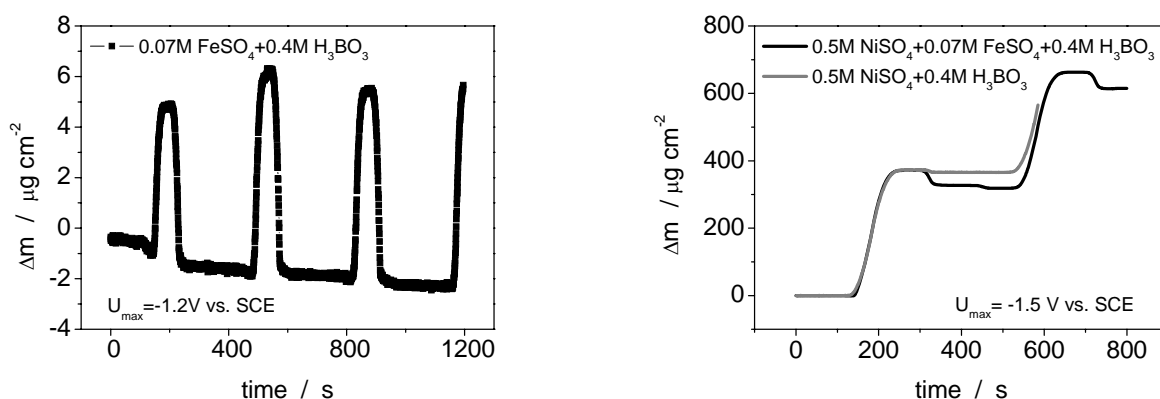


Figure 45. Mass transients during cyclic voltammograms at  $10 \text{ mV s}^{-1}$  in orientation E and in absence of a superimposed magnetic field for different electrolytes.

For all the electrolytes used (bath 1, 2 and 3, see Table 1, p.39), a small peak was

obtained at approximately  $-0.2\text{V}$  vs. Ag/AgCl. In order to identify its origin, a set of measurements in a  $0.5\text{M MgSO}_4+0.4\text{M H}_3\text{BO}_3$  electrolyte were performed. No metal deposition occurs from this electrolyte in the potential range used in the present study, thus the potential region where the HER occurs can be easily identified (Fig. 46A). The initial pH value of the  $\text{MgSO}_4$  electrolyte was 4.38. The pH value was further adjusted to 2.0 and 3.0 by adding concentrated  $\text{H}_2\text{SO}_4$ . One can notice that there is a peak in the cathodic scan which occurs at  $-0.8\text{V}$  vs. Ag/AgCl for an electrolyte with pH 2.0, and at  $-0.68\text{V}$  vs. Ag/AgCl for an electrolyte with pH 3.0 (Fig. 46A). Furthermore the peak current decreases with increasing pH and disappears at higher pH values, like 4.4. Therefore, this peak can be ascribed to the diffusion controlled proton reduction [196].

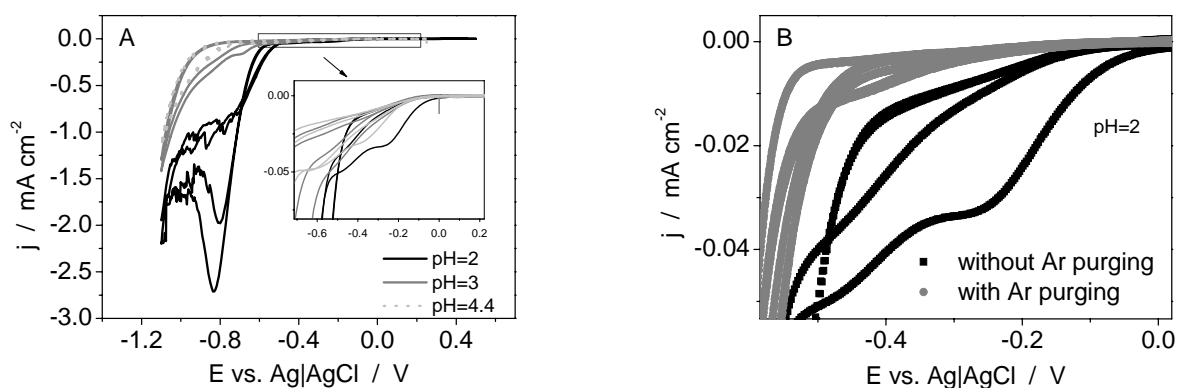


Figure 46. Cyclic Voltammograms in a  $0.5\text{M MgSO}_4+0.4\text{M H}_3\text{BO}_3$  electrolyte at different pH values. Measurements were done in orientation E and in absence of a superimposed magnetic field. Scan rate was  $5\text{ mV s}^{-1}$ .

The small peak that occurs at  $-0.2\text{V}$  vs. Ag/AgCl during the first cathodic scan in the electrolytes with Ni or Fe ions, was present also in the electrolyte with Mg ions. However, it disappears when the solution was purged at least 15 minutes before the sweep with Argon (Fig. 46B). After this, 5 minutes Ar was let to flow over the electrolyte, in order to form an Ar blanket. The disappearing of the peak at  $-0.2\text{V}$  vs. Ag/AgCl with purging indicates that this peak is due to oxygen reduction.

The frequency shift during the cyclic voltammograms in the  $\text{MgSO}_4$  electrolyte showed a periodic oscillation (Fig. 47). As no oscillations could be observed in the damping signal, we assumed that these oscillations are associated with oxide formation and reduction. The increasing tendency of the frequency in time (and the simultaneous decreasing of the damping) can be explained by the hydrogen bubble formation that do not detach from the

electrode surface (orientation of the cell was E).

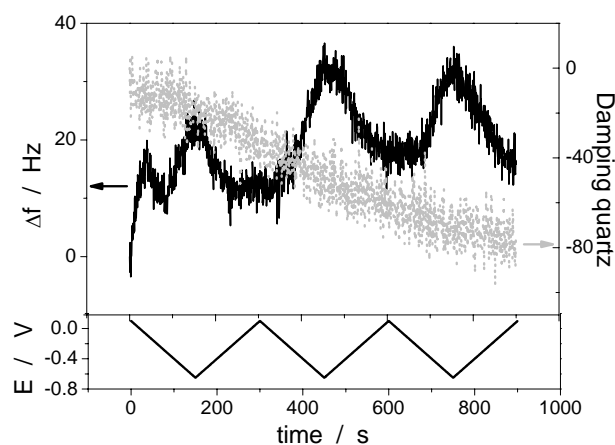


Figure 47. Frequency and damping shift corresponding to the cyclic voltammogram described in the previous figure, Fig. 46B, in the case that the electrolyte was purged with Ar (upper panel). The corresponding potential variation as a function of time is represented in the lower panel.

Potentiostatic step experiments were performed for the 0.5M  $\text{MgSO}_4$  + 0.4M  $\text{H}_3\text{BO}_3$  electrolyte (of all three pH values) from 0.5V vs. Ag/AgCl to a negative potential and then back to the 0.5V. The range of potential investigated was from -0.2V vs. Ag/AgCl to -1V vs. Ag/AgCl. The frequency and the damping shifts were monitored. The frequency continuously increased when the potential was stepped from 0.5V vs. Ag/AgCl to a negative value (<-0.2V).

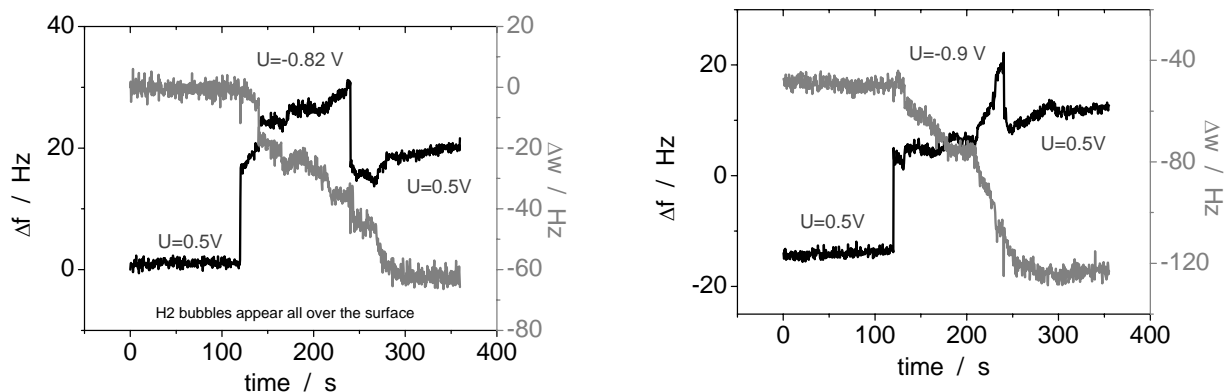


Figure 48. Resonance frequency shifts and damping shifts of the quartz crystal during potentiostatic step experiments. A 0.5M  $\text{MgSO}_4$ +0.4M  $\text{H}_3\text{BO}_3$  (pH 2.0) electrolyte was used. Investigations were carried out in orientation E and without an applied magnetic field.

In the case of the  $\text{MgSO}_4$  electrolyte of pH 2.0 (Fig. 48) hydrogen bubbles appeared at the rim of the Au electrode starting from  $-0.65\text{V}$ . When the potential reaches  $-0.8\text{V}$  vs. Ag/AgCl, the whole electrode surface was covered with hydrogen bubbles. The decrease of the resonant frequency of the quartz crystal (visible at more cathodic potentials, see Fig. 48) can be explained by the detaching of the bubbles from the electrode surface. Thus, after potential of the working electrode is kept at very cathodic values for enough time, the hydrogen bubbles become so large that the buoyancy forces will detach them.

The effect induced by superimposing a magnetic field during the cyclic voltammograms in the electrolyte 3 (see Table 1, p.39) will be discussed in the following. For these experiments, cyclic voltammetric measurements (five cycles,  $5\text{ mV s}^{-1}$ ) were carried out from the open circuit potential to  $-1.1\text{ V}$ , going first in the cathodic direction. As discussed already in connection with Fig. 46A, in the potential region from  $-0.4$  to  $-0.7\text{ V}$  the HER is the dominating reaction for a pH value of 3.0 (Fig. 49). Note that for the following experiments the potential is referred vs. SCE, while before (Fig. 46) it was measured vs. Ag/AgCl. From the time derivative of the EQCM data which corresponds to the partial current of the alloy deposition (Fig. 49b) it can be proved that the current in the potential range from  $-0.4$  to  $-0.7\text{V}$  is due to the HER. In this potential range the resonance frequency of the quartz crystal increases by approximately  $50\text{-}150\text{Hz}$ , which corresponds to an apparent decrease in mass of  $0.2\text{ -}0.65\text{ }\mu\text{g cm}^{-2}$  [197]. The possible origin for the increase of the resonance frequency of the quartz crystal with the potential was discussed before (see Fig. 13, p.44 and the corresponding discussions). The increase of the resonance frequency proves that no deposition occurs in the potential region from  $-0.4$  to  $-0.7\text{V}$ .

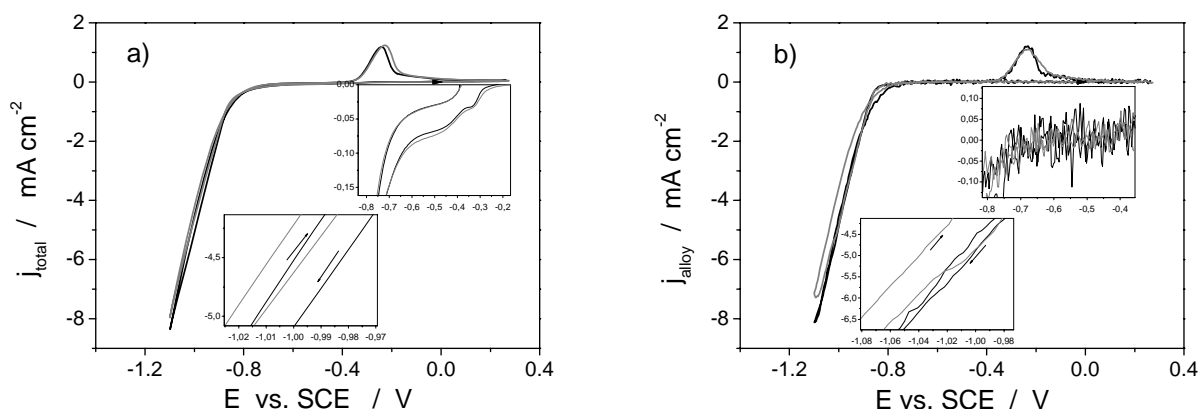


Figure 49. (a) Typical cyclic voltammogram (4<sup>th</sup> cycle,  $5\text{ mV s}^{-1}$ , orientation E) and (b) time derivative of the EQCM signal in  $0.5\text{ M NiSO}_4\cdot 6\text{H}_2\text{O}$ ,  $0.01\text{ M FeSO}_4\cdot 7\text{H}_2\text{O}$ ,  $0.4\text{ M H}_3\text{BO}_3$  (pH 3, 298 K). Black curves: no magnetic field, grey curves:  $B=0.7\text{ T}$ .



The HER increases in the presence of the magnetic field because it is limited by mass transport and the MHD stirring decreases the diffusion layer thickness of the hydrogen ions. At around -0.75 V the alloy deposition starts. EDX analyses for the layers deposited at this potential yield a composition of 8 at-% Fe and 92 at-% Ni. Interestingly the partial current of the alloy deposition decreases in the magnetic field. This inhibition is visible in both the total current (Fig. 49a) and the EQCM data (Fig. 49b), and it occurred for both orientations of the working electrode (parallel to gravity and perpendicular to gravity). The dissolution peak is not affected by the magnetic field.

Because of the high Ni concentration one can assume that the Ni reduction is over a wide potential range mixed controlled while the Fe reduction is diffusion controlled. Therefore, one can expect a stronger magnetic field effect in the case of Fe. As the iron reduction current increases the surface concentration of intermediate Fe (I) species increases. According to the model of Matlosz [22] these Fe(I) species inhibit the Ni reduction and the net effect would be decrease of the total current density which is in perfect agreement with the experimental data.

## ***IV.2 Effects Induced by Variations in the Total Current and by the Presence of a Magnetic Field in the Properties of Ni-Fe Alloys***

### **IV.2.1 Effect of the Total Current Density on the Alloy Composition**

It has been reported that the iron content increases at low current densities, reaches a maximum and then decreases again. Several explanations are given for this behaviour. Brenner assumed that the codeposition before the maximum is of normal type, which means that the proportion of the less noble metal in the deposit increases with increasing the current density. At sufficiently high current densities, the deposition of the less noble species should tend downwards, as the deposition is diffusion controlled [19]. Thus, after a specific current density, the iron reduction reaction will be reduced in relation to the nickel reduction and as a consequence, the iron content of the deposited layer will decrease. Horkans [30], who assumed that the alloy deposition occurs via the hydroxide formation (like in the model proposed by Dahms and Croll [20]), explained the decrease in the iron content via the slow

ionic diffusion of the hydroxides at higher current densities. Matlosz [22] pointed out that the inhibition of the nickel appears at a specific potential, at which the competition between the adsorption rates of the intermediate ions,  $\text{Fe(I)}_{\text{ads}}$  and  $\text{Ni(I)}_{\text{ads}}$  becomes important. The maximum of the iron content corresponds to the state of maximum inhibition. With decreasing potential the inhibition of Ni will disappear, and as the iron reaches its limiting current, the surface concentration and consequently the surface coverage with iron ions will decrease.

#### IV.2.1.a Ni-Fe alloy containing less than 10 at% Fe

First, the changes in the alloy composition in function of the total current density were investigated in the absence of an external magnetic field. Between three and eight samples were prepared for a variety of current densities in the range  $-1$  to  $-60 \text{ mA cm}^{-2}$  (Fig. 50) (constant total charge density of  $4.5 \text{ C cm}^{-2}$  was fixed). The data in Fig. 50 represent the averaged values of each set of measurements. The standard error (shown as the error bar in Fig. 50) of the mean value was evaluated from the ratio between the standard deviation and the square root of the number of measurements.

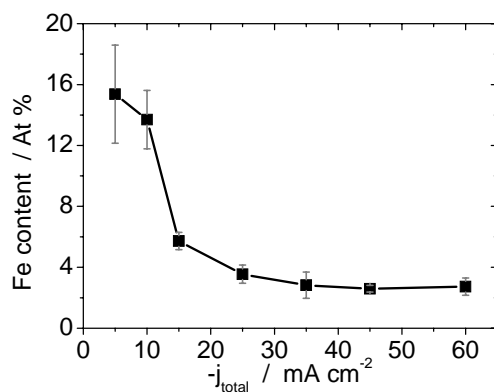


Figure 50. Iron content of the deposited alloy as a function of the total current density (orientation B, 0mT). The electrolyte was  $0.5 \text{ M NiSO}_4 \cdot 6\text{H}_2\text{O}$ ,  $0.01 \text{ M FeSO}_4 \cdot 7\text{H}_2\text{O}$ ,  $0.4 \text{ M H}_3\text{BO}_3$  (pH 3, 298 K) [198]

In the low current density range ( $-5$  to  $-10 \text{ mA cm}^{-2}$ ) the Fe/Ni ratio in the alloy (ca. 14:86 in terms of molar ratio for a current density of  $-10 \text{ mA cm}^{-2}$ ) is higher than in the electrolyte (2:98). At higher current densities ( $-15$  to  $-40 \text{ mA cm}^{-2}$ ) the Fe/Ni ratio in the alloy decreases significantly (ca. 5:95 for a current density of  $-25 \text{ mA cm}^{-2}$ ), but it is still higher than in the electrolyte. In passing we note that this is the expected behaviour for a

system showing anomalous co-deposition (Fe is the less noble, Ni the more noble metal).

The expected maximum of the Fe content [30,33,199] was not observed in the present study. This is because our current densities are beyond the current density where the maximum occurs.

As mentioned before, several explanations have been given for the decrease of the Fe content at high current densities [19,20,22,30,200]. The simplest one is that both Ni and Fe reach their limiting currents. For the electrolyte composition and the current densities used in this study the limiting current density of iron is much smaller than the total current density. The partial current of the iron reduction can be obtained from partial current of the alloy deposition (obtained from the EQCM data) and the known dependence of the alloy composition on the current density (Fig. 50). Using these data we find that at higher potentials the partial current of the iron reduction levels off well below 1 mA cm<sup>-2</sup> (around 0.3 mA cm<sup>-2</sup>) (Fig. 51).

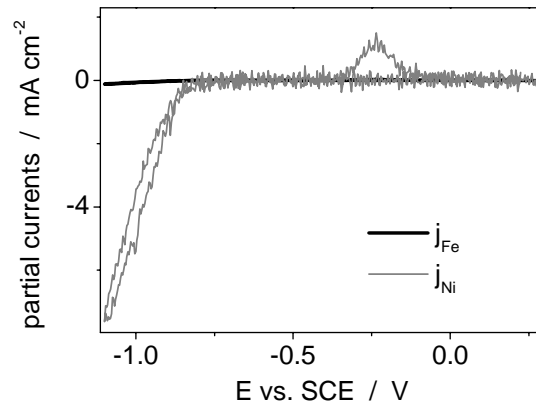


Figure 51. Partial currents of Ni and Fe during cyclic voltammograms (at 5 mV s<sup>-1</sup>) from 0.5M NiSO<sub>4</sub>\*6H<sub>2</sub>O, 0.01M FeSO<sub>4</sub>\*7H<sub>2</sub>O, 0.4M H<sub>3</sub>BO<sub>3</sub>, pH 3.

In order to obtain the Fig. 51, the following formulas were used (Eq. 28):

$$j_{Fe} = \frac{dm_{Fe}}{dt} \frac{1}{A} \frac{z_{Fe} F}{M_{Fe}}; m_{Fe} = w(Fe) * m_{total}; \quad (\text{Eq. 28})$$

where  $w(Fe)$  is the content in Fe of the alloys. The  $w(Fe)$  values were determined from EDX analysis for different current densities. Using Fig. 50, the Fe content of the alloys in function of the current density was approximated to be given by different functions. For example, in the current range from -1 to -5 mA cm<sup>-2</sup> and from -15 to -40 mA cm<sup>-2</sup>, the Fe content of the alloys as a function of the total current density applied can be described by an exponential

decay function ( $w(\text{Fe})=A_1*\exp(-j/A_2)+A_3$ ). From -5 to -15mA cm<sup>-2</sup> a sigmoidal fit was done, according to the Boltzmann model. The function implemented is now  $w(\text{Fe})=A_2+(A_1-A_2)/(1+\exp((j-j_0)/dj))$ . After determining the relations of  $w(\text{Fe})$  as a function of the total current density applied, one can determine the mass of Fe which is deposited at different current densities (Eq. 28). The later can be used to calculate the partial current of Fe, as described in (Eq. 28). The partial current of Ni can calculated in a similar way to the Fe partial current. The results obtained can be plotted vs. the potential applied (Fig. 51).

#### IV.2.1.b Ni-Fe alloy containing approximately 20 at% Fe

At a given current density, the Fe content of the Ni-Fe alloy increases with increasing concentration of Fe in the electrolyte (Fig. 50, Table 12). As already described in the previous section (IV.2.1.a), increasing the total current density induces a decrease in the Fe content of the Ni-Fe alloy (Table 12).

Table 12. Fe content of the electrodeposited Ni-Fe alloys from 0.5M NiSO <sub>4</sub> *6H <sub>2</sub> O, 0.07M FeSO <sub>4</sub> *7H <sub>2</sub> O, 0.4M H <sub>3</sub> BO <sub>3</sub> , pH=2, at a total charge density of 4.5 C cm <sup>-2</sup> in orientation E and B=0T.								
<b>j<sub>total</sub> (mA cm<sup>-2</sup>)</b>	-15	-25	-35	-45	-65	-95	-105	-110
<b>Fe (at%)</b>	49	47	39	21	18	16÷22	14÷21	9÷12

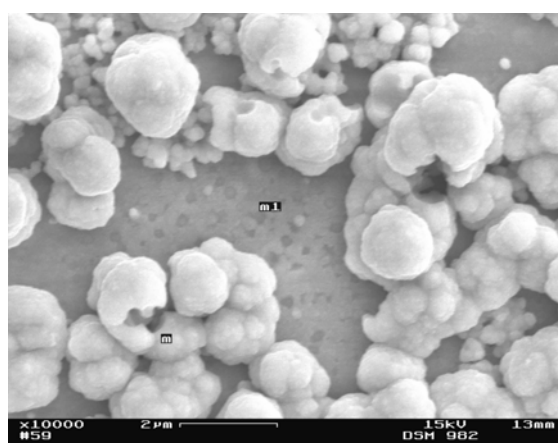


Figure 52. Ni-Fe layer deposited at -105 mA cm<sup>-2</sup> from 0.5M NiSO<sub>4</sub>\*6H<sub>2</sub>O, 0.07M FeSO<sub>4</sub>\*7H<sub>2</sub>O, 0.4M H<sub>3</sub>BO<sub>3</sub>, pH=2, at a total charge density of 4.5 C cm<sup>-2</sup> in orientation E and B=0T. The EDX analysis showed that the deposited Ni-Fe layer contains 16 at% Fe in the region *m<sub>1</sub>* and 20at% in the region *m*.

At higher current densities (-95 to -110 mA cm<sup>-2</sup>) the deposited layers become

inhomogeneous (Fig. 52) and sometimes exfoliated from the Au substrate. Thus, often on the electrode surface could be found regions where the Au electrode was not covered or specific surface features, which revealed a different composition than the surrounding areas (Fig. 52).

## IV.2.2 Effect of a Superimposed Magnetic Field on the Alloy Composition

The magnetic field effects on the electrodeposition of Ni-Fe alloy from 0.5 M  $\text{NiSO}_4 \cdot 6\text{H}_2\text{O}$ , 0.01 M  $\text{FeSO}_4 \cdot 7\text{H}_2\text{O}$ , 0.4 M  $\text{H}_3\text{BO}_3$  (pH 3 and 2) will be presented just for two current densities (-25 and  $-60 \text{ mA cm}^{-2}$ ) [198]. A constant total charge density of  $4.5 \text{ C cm}^{-2}$  was used, which corresponds to a layer thickness of  $1.5 \mu\text{m}$ .

Four values of the current density were chosen to investigate the effects induced by superimposing a magnetic field during Ni-Fe electrodeposition from 0.5M  $\text{NiSO}_4 \cdot 6\text{H}_2\text{O}$ , 0.07M  $\text{FeSO}_4 \cdot 7\text{H}_2\text{O}$ , 0.4M  $\text{H}_3\text{BO}_3$ , pH=2. These were -30, -50, -70 and  $-90 \text{ mA cm}^{-2}$  and the total charge density was again  $4.5 \text{ C cm}^{-2}$ .

In all the measurements, the electrolyte was purged with Argon fifteen minutes before each investigation.

### IV.2.2.a Ni-Fe alloys containing less than 10 at% Fe

The potential transients for  $j_{\text{total}} = -25 \text{ mA cm}^{-2}$  are presented in Fig. 53.

In the absence of a magnetic field the deposition potential,  $E_{\text{dep}}$ , is  $-1.48 \pm 0.02 \text{ V vs. SCE}$  and the Fe content is  $4.8 \pm 0.2 \text{ at-\%}$ . If B is applied in orientation E,  $E_{\text{dep}}$  becomes more cathodic (Fig. 53a) and the Fe content remains virtually the same (Table 13). If B is applied in orientation B, the polarization decreases ( $E_{\text{dep}}$  becomes more anodic, Fig. 53b), and the Fe content increases to  $5.4 \pm 0.2 \text{ at-\%}$  (Table 13). A qualitatively similar behaviour is observed in the current density range from  $-25 \text{ mA cm}^{-2}$  to  $-60 \text{ mA cm}^{-2}$ . Looking at the data in Table 13 one might argue that the layers deposited in orientation E contained slightly more iron than those prepared in orientation B and this "effect" would be more pronounced for the smaller current densities. Notice however, that the accuracy of the EDX data is not sufficient to speculate about a possible mechanism. In the following an explanation about the significant changes of the polarization and the increase of the Fe content in orientation B is given.

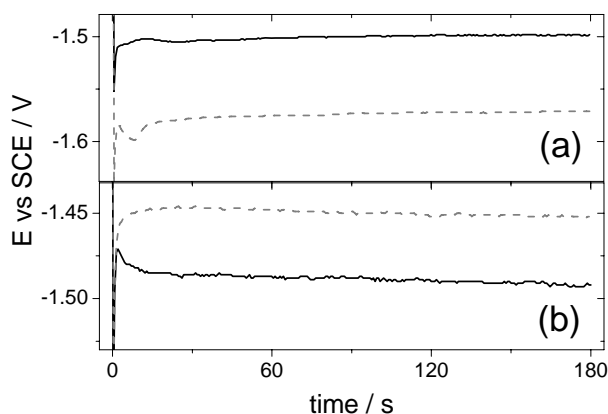


Figure 53. Transients of the deposition potential for the orientation E (a), and for the orientation B (b). The black solid curves correspond to  $B=0\text{mT}$ , and the grey dashed curves stand for  $B=740\text{mT}$  (a) or  $715\text{mT}$  (b). The total current density was  $j_{\text{total}} = -25\text{ mA cm}^{-2}$ . Experiments were carried out from  $0.5\text{M NiSO}_4 \cdot 6\text{H}_2\text{SO}_4 + 0.01\text{M FeSO}_4 \cdot 7\text{H}_2\text{O} + 0.4\text{M H}_3\text{BO}_3$ ,  $\text{pH}=3$ .

Table 13. The iron content in atomic percents of the deposited alloys in function of the direction of the external magnetic field and the total current density applied. Electrolyte used consisted in  $0.5\text{M NiSO}_4 \cdot 6\text{H}_2\text{SO}_4 + 0.01\text{M FeSO}_4 \cdot 7\text{H}_2\text{O} + 0.4\text{M H}_3\text{BO}_3$ ,  $\text{pH}=3$ .

$j_{\text{total}}$ ( $\text{mA cm}^{-2}$ )	<b>B=0T</b> orientation E	<b>B=0.7T</b> orientation E	<b>B=0T</b> orientation B	<b>B=0.7 T</b> orientation B	<b>B=0.6T</b> orientation C
<b>-25</b>	$4.8 \pm 0.2$	$4.5 \pm 0.4$	$4.1 \pm 0.3$	$5.4 \pm 0.2$	$4.4 \pm 1.2$
<b>-60</b>	$2.8 \pm 0.1$	$2.2 \pm 0.3$	$2.9 \pm 0.6$	$3.1 \pm 0.3$	$3.0 \pm 0.8$

In order to understand the effect of the magnetic field (and its orientation) on the polarization one must take into consideration the natural convection in the cell (see section I.3).

In the presence of a B field magnetic forces will be active which induce magnetohydrodynamic convection. The latter will interact with the flow profile of the natural convection. As a result the transport of electroactive species towards the electrode is modified and in a galvanostatic experiment the potential will shift [77,201]. When the working electrode is arranged parallel to the gravitational field, the mass transfer is expected to be enhanced because of additional convection induced by density gradients [61,202]. As a rule of thumb it can be stated that increased mass transport will decrease the polarization ( $E_{\text{dep}}$  becomes more anodic) and decreased mass transport will increase the polarization ( $E_{\text{dep}}$  becomes more cathodic). As has been outlined in the section IV.2.1, p.93, the composition of

the alloy will depend on the deposition potential [30,195,199] and we can expect changes of the composition, too.

In orientation E, the MHD convection is perpendicular to the natural convection and without numerical simulations it is hard to judge if the mass transport towards the electrode increases or decreases. According the potential data the mass transport should decrease because the polarization increases. In orientation B, the MHD convection is parallel to the natural convection and we can expect an increase of the mass transport which is in perfect agreement with the data in Fig. 53 (polarization decreases when B is on).

Actually any discussion of the force balance should also consider the concentration gradient force,  $f_{\nabla c}$  (Eq. 11). In an electrodeposition reaction involving paramagnetic species it has the same direction as the concentration gradient ( $\chi_m > 0$ ) and thus tends to move volume elements with high susceptibility away from the working electrode. It has been shown that  $f_{\nabla c}$  can counterbalance the natural convection [61]. In orientation E it has the opposite direction as the vector NC and indeed seems to counterbalance it partly (polarization increases when B is on). In orientation B the  $f_{\nabla c}$  vector points away from the electrode and is perpendicular to NC and MHD. Again the flow profile resulting from this interaction is hard to predict but from the polarization data we can conclude that it increases the mass transport.

For orientation C there will be no macroscopic MHD convection because  $j$  and  $B$  are parallel. The steady state deposition potentials varied just by 4 mV to 10 mV, and no clear tendency was found. Thus it is not astonishing that the iron content remained constant within the limit of error (Table 13). Notice that in orientations E and B  $E_{\text{dep}}$  varied by more than 60 mV (Fig. 53).

#### **IV.2.2.b Ni-Fe alloys containing approximately 20 at% Fe**

The influence of the different orientations of a magnetic field (with regard to the electric field and gravity) on the composition of the electrodeposited alloys is illustrated in the Fig. 54.

When the Lorentz force and the natural convection act in the same direction, an increase of the iron content of the alloys was obtained. This result is valid for the case that the working electrode is parallel to the gravity. For both electrolytes (baths 3 and 4, see Table 1, p.39) and for different current densities used for electrodeposition, similar results were obtained [197,198]. The increase of the Fe content with the magnetic flux density is attributed to the MHD effect and it is based on the fact that Fe deposition is mass transport

controlled (see also section IV.2.1, p.95). No significant changes the iron content of the alloys were observed when the magnetic field was applied parallel to the electric current. This can be explained by the absence of the macro-MHD effect (MHD effect which occurs on macroscales) and is based on the importance of Lorentz force in relation to the gradient forces in electrochemical reactions.

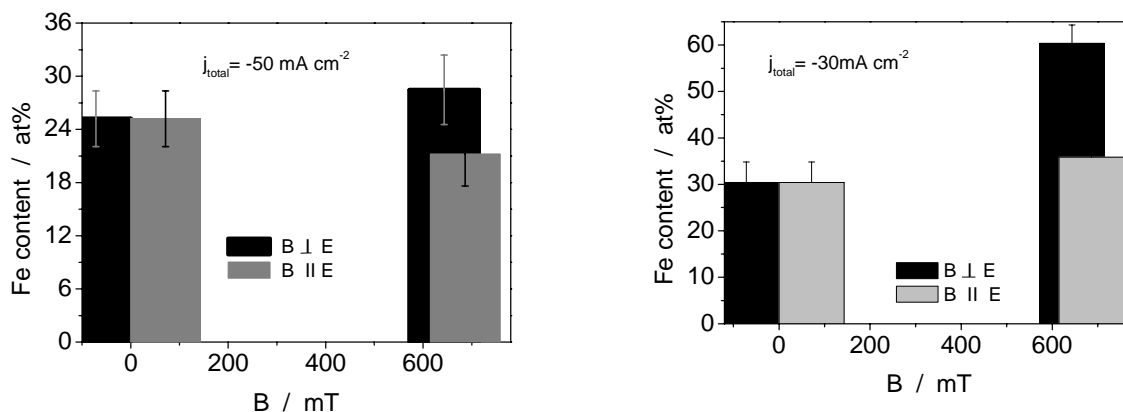


Figure 54. Iron content of the alloy obtained from the EDX analysis. The working electrode was fixed vertical in the cell for all these measurements. Magnetic field could be applied parallel (orientation C) or perpendicular to the electric current (orientation B). Deposition was done from the electrolyte 3, pH 2.0, (Table 1, p.39), at a total current density of  $-50 \text{ mA cm}^{-2}$  or  $-30 \text{ mA cm}^{-2}$ . Just the results obtained in 0T and for the maximum magnetic flux possible in orientations B and C are represented here.

### IV.3 HER during Ni-Fe alloy codeposition

The EQCM was used to determine the partial current of the HER,  $j_{\text{HER}}$ , during the alloy deposition (see section II.2, p.41). In orientation B  $j_{\text{HER}}$  increased with the magnetic field (Fig. 55). This increase can be explained on the basis of the mechanisms that govern the reduction reactions [171]. The alloy deposition is (mostly) activation controlled, while the HER is mass transport controlled. A superimposed magnetic field perpendicular to the electric field decreases the diffusion layer thickness and thus increases the mass transfer. Therefore, the primary effect of the magnetic field is to facilitate the hydrogen evolution reaction, (see also the current-potential curves, p. 98).



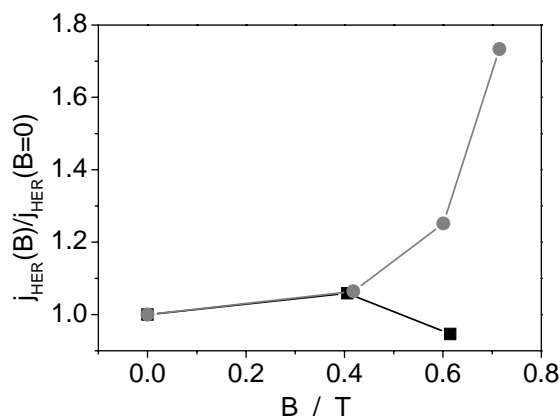


Figure 55. Normalized partial current density of the hydrogen evolution,  $j_{\text{HER}}$ , in orientation B (●) and orientation C (■) for a total current density of  $-60 \text{ mA cm}^{-2}$  as a function of the magnetic flux density. The data have been normalized with respect to the value of  $j_{\text{HER}}$  in absence of a magnetic field. Electrolyte 4 (Table 1, p.39), at pH=3 was used.

No significant effect on  $j_{\text{HER}}$  was observed when the magnetic field was applied parallel to the electric current (Fig. 55). In this case, no (macroscopic) Lorentz forces appear, and the mass transfer process is not influenced. A macroscopic Lorentz force is one that acts on macroscopic scales.

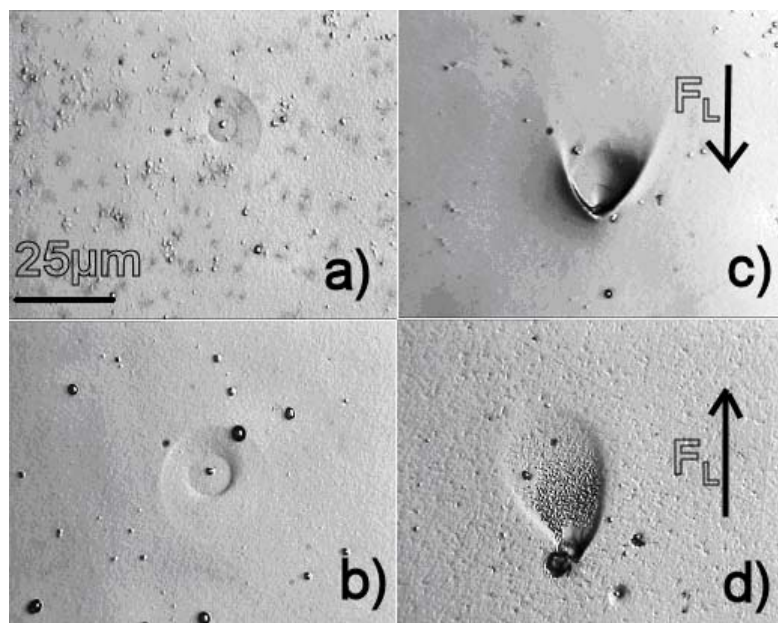


Figure 56. Optical microscope images of the layers deposited at  $j_{\text{total}} = -25 \text{ mA cm}^{-2}$ , with the shapes of hydrogen bubbles. (a and d are for orientation (B), b is for orientation (C) and c is for the orientation (E)). (a)  $B=0$ , (b)  $B=615 \text{ mT}$ , (c)  $B=740 \text{ mT}$ , (d)  $715 \text{ mT}$ . The electrolyte 4 (pH 3.0) was used (Table 1, p.39).

Optical micrographs taken after the deposition showed traces of the hydrogen bubbles, some of them being quite large (approximately 50  $\mu\text{m}$ ). They have circular shapes if no MHD convection was present, i.e. for  $B=0$  and for magnetic field applied in orientation C. For the orientation B they have a typical “tail” indicative for the MHD flow around the bubble (Fig. 56). This effect has been already described by other authors [6,10]. The interplay between the natural convection and the MHD effect can be seen in the orientation E. Even if the Lorentz force tends to align the “tail” of the hydrogen bubble, it does not succeed completely. The final direction of the tail is also affected by the natural convection. The direction of the Lorentz force in the case of the orientation E is in the plane of the electrode, while the natural convection is perpendicular to the electrode.

Figure 57a is a typical example for the damping changes of the quartz crystal (in terms of changes of the FWHM of its resonance curve, see section I.2, p.11) during the deposition in orientation E.

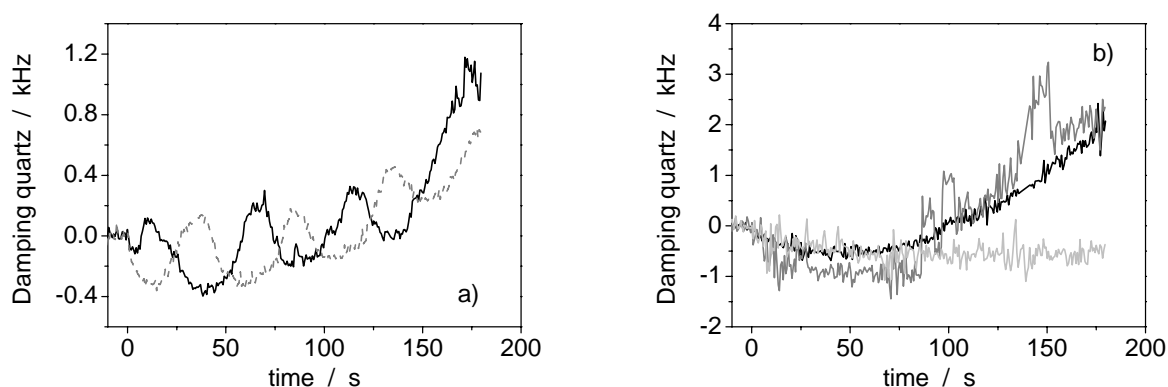


Figure 57. The variation of the damping of the quartz in time. The total current density was  $j_{\text{total}} = -25 \text{ mA cm}^{-2}$ . (a): black curve stands for  $B=0\text{mT}$ , and grey curve stands for  $740\text{mT}$  (orientation E). (b): black curve stands for  $B=0\text{mT}$ , and grey curve stands for  $615 \text{ mT}$  (orientation C), and the light grey curve stands for  $715 \text{ mT}$  (orientation B). Electrolyte 4, (pH 3.0) was used (Table 1, p.39).

The periodic oscillations seen in Fig. 57a can be explained with interference effects of compressional waves emitted by the quartz crystal. These waves are reflected by the surface of the counter electrode and depending on the distance between the source (quartz surface) and the reflector (counter electrode) interact constructively or destructively. In other words, the volume between the working and the counter electrode acts as a resonance cavity and the dimension of this cavity becomes smaller by the electrodeposition process. A more detailed investigation of this effect is currently under way. However, it is not in focus of the present work. A similar behaviour has been found in the case of evaporation of liquids above a quartz crystal [203]. The aperiodic oscillations of the damping have a different origin. It is

well known that the damping of the quartz crystal increases with the viscosity of the adjacent medium. As the viscosity of hydrogen is much smaller than that of the aqueous solution the detachment of the hydrogen bubbles is accompanied by an increase in the damping, while a decrease in the damping indicates that new hydrogen bubbles are formed and are growing.

The increasing tendency of the damping with the time indicates an increasing surface roughness of layers. Rough layers deposited on the quartz crystal induce a larger damping compared to smooth layers. This can be explained with the generation of turbulences above the rough surface which leads to an increased dissipation of energy. The qualitative information about the roughness of the deposited layers given by EQCM can be compared to the quantitative information given by AFM. The gold electrode on the polished quartz has a typical roughness of 4-5 nm (RMS value determined by AFM). The growth of the layer will increase this value up to 25 nm (see section IV.4, p.106).

For orientation C there were no clear oscillations of the damping (Fig. 57b). In orientations B and C the quartz is fixed vertically and the reference electrode between the quartz and the counter electrode acts as a spoiler for the compressional waves.

For orientation B (Fig. 57b) the damping stays constant during the whole deposition process. That means that smooth layers are formed.

#### ***IV.4 Morphology and Roughness of Ni-Fe layers***

Scanning electron microscopy showed some degree of porosity for the layers prepared in the absence of a magnetic field (Figs. 58, a and c) from the bath 4 (Table 1, p.39).

Atomic force microscopy (figures not shown) indicated a pore depth of (at least) some ten nm and a pore diameter of some hundred nm. With increasing current density the porosity decreases (Fig. 59). If the layers were deposited in a B field there were no pores. The pore formation is a consequence of the HER. Small hydrogen bubbles stay trapped long enough at the surface to cause the formation of voids. Under the influence of the MHD flow the residence time of the bubbles at the surface is shorter (they are swept away) and pore formation does not occur.

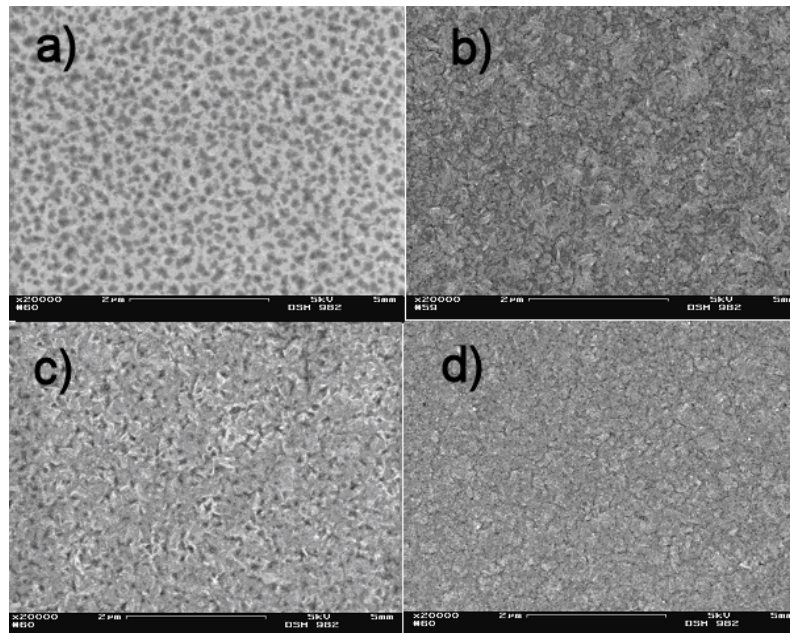


Figure 58. SEM images for Ni-Fe layers electrodeposited at  $j_{\text{total}} = -25 \text{ mA cm}^{-2}$ , in orientation E (*a* and *b*) and in orientation B (*c* and *d*). The images *a* and *c* show the layers which are prepared without an external magnetic field, *b* and *d* show the layers which are prepared in a magnetic field applied perpendicular to the electric current,  $B = 740 \text{ mT}$  (*b*), respectively  $715 \text{ mT}$  (*d*). Bath 4 (see Table 1, p.39) was used for these measurements.

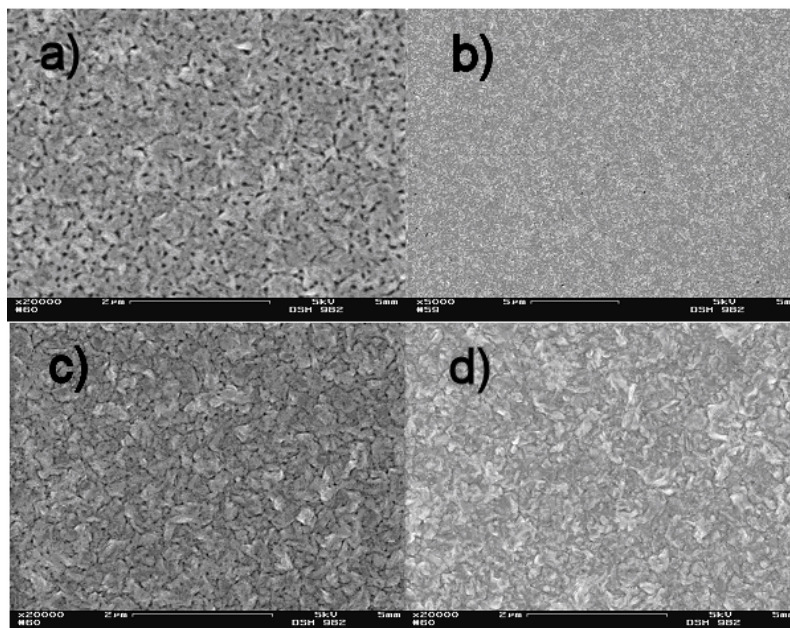


Figure 59. The SEM images for Ni-Fe layers electrodeposited at  $j_{\text{total}} = -60 \text{ mA cm}^{-2}$ , orientation E (*a* and *b*) and orientation B (*c* and *d*). The images *a* and *c* show the layers which are prepared without an external magnetic field, *b* and *d* show the layers which are prepared in a magnetic field applied perpendicular to the electric current,  $B = 740 \text{ mT}$  (*b*), respectively  $715 \text{ mT}$  (*d*). Bath 4 (see Table 1, p. 39) was used for these measurements.

One can see in Fig. 60 that for the permalloy, which is  $\text{Fe}_{20}\text{Ni}_{80}$ , (like in the case of Ni-Fe

alloy with low Fe content), more homogenous and more uniform layers are obtained in the case when MHD convection is present [197].

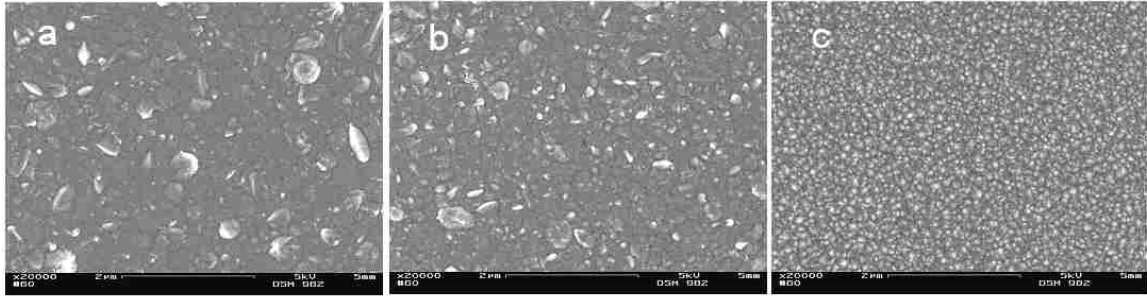


Figure 60. SEM images for a Ni-Fe layers deposited from electrolyte 3 (see Table 1, p.39), pH=2. Current density  $j = -50 \text{ mA cm}^{-2}$  (a)  $B = 0 \text{ mT}$ , Fe=19at% (orientation B), (b)  $B = 615 \text{ mT}$ , Fe=26at% ( $B \parallel j$ , orientation C), (c)  $B = 715 \text{ mT}$ , Fe=36at% ( $B \perp j$ , orientation B).

A magnetic field applied parallel to the electrode surface increases the Fe content of the alloys. This will induce changes in the morphology of the layers. It was observed that the layers with high iron content look more compact and more uniform (Fig. 60c).

For both the permalloy and the low Fe content alloy, no significant macroscopic changes in the morphology were observed when the layers were deposited in a magnetic field applied perpendicular to the electrode surface (Figs. 60b, 61).

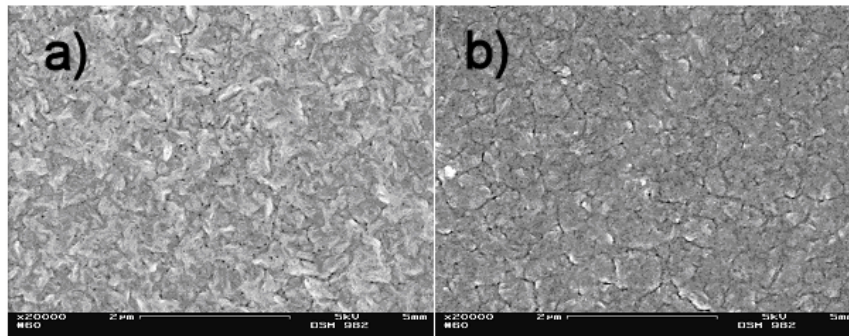


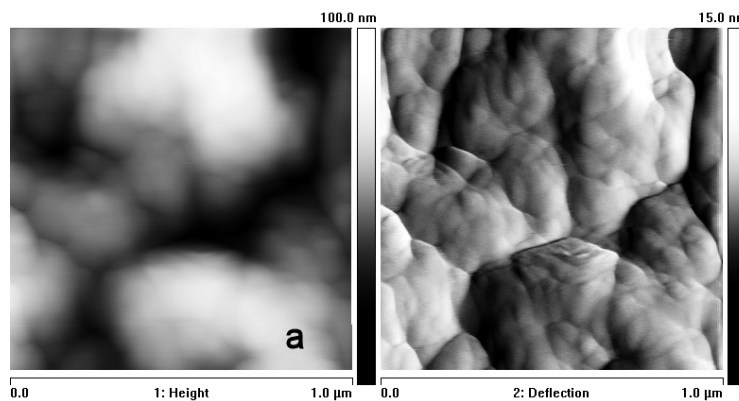
Figure 61. SEM images of the deposited layers in orientation C. (a):  $j_{\text{total}} = -60 \text{ mA cm}^{-2}$ , (b):  $j_{\text{total}} = -25 \text{ mA cm}^{-2}$ . Electrolyte 4 (pH 3.0) was used (see Table 1, p.39).

However, the AFM measurements proved a slight decrease in the roughness values for the layers deposited in a magnetic field, independent if it was parallel or perpendicular to the electric current (Table 14). The decrease in roughness with the magnetic field was obtained for both electrolytes analysed (baths 3 and 4, see Table 1, p.39) (from  $10|_{0\text{T}} - 8|_{0.7\text{T}}$  nm for permalloy, and from  $8|_{0\text{T}} - 7|_{0.7\text{T}}$  nm for the low Fe content alloy). This decrease can be

correlated with the micro and macro MHD convections on the electrode surface that influence the growth (see also section I.3.1, p.11). The decrease of the roughness is in agreement with the disappearance of the pores seen in the SEM. As an additional fact, it was observed that the layers deposited between  $-1$  and  $-5 \text{ mA cm}^{-2}$  were very rough and had a poor visual appearance.

Table 14. Surface roughness ( $R_q$ ) of the deposited layers, expressed in nm. Electrolyte 4 (pH 3.0) was used here (see Table 1, p.39).			
$j_{\text{total}} \text{ (mA cm}^{-2}\text{)}$	<b>B=0T</b> orientation B	<b>B=0.7 T</b> orientation B	<b>B=0.6T</b> orientation C
<b>-25</b>	$8.6 \pm 1.4$	$7.8 \pm 0.5$	$7.4 \pm 1.1$
<b>-60</b>	$10.2 \pm 0.5$	$9.7 \pm 0.3$	$9.5 \pm 0.3$

AFM investigations showed that smaller grains are formed in the presence of a magnetic field. This applies to the perpendicular and the parallel orientation (Fig. 62). For the perpendicular orientation of B and j the grains seem to be elongated in one preferential direction (Fig. 62c). This could be a direct consequence of the MHD convection, which would favor the growth of the grains in the direction of the Lorentz force. Such an explanation is in perfect agreement with literature [70]. The local microscopic MHD turbulences, which appear for B and j parallel, seem to induce a more or less circular symmetry of the grains (Fig. 62b) [197,198].



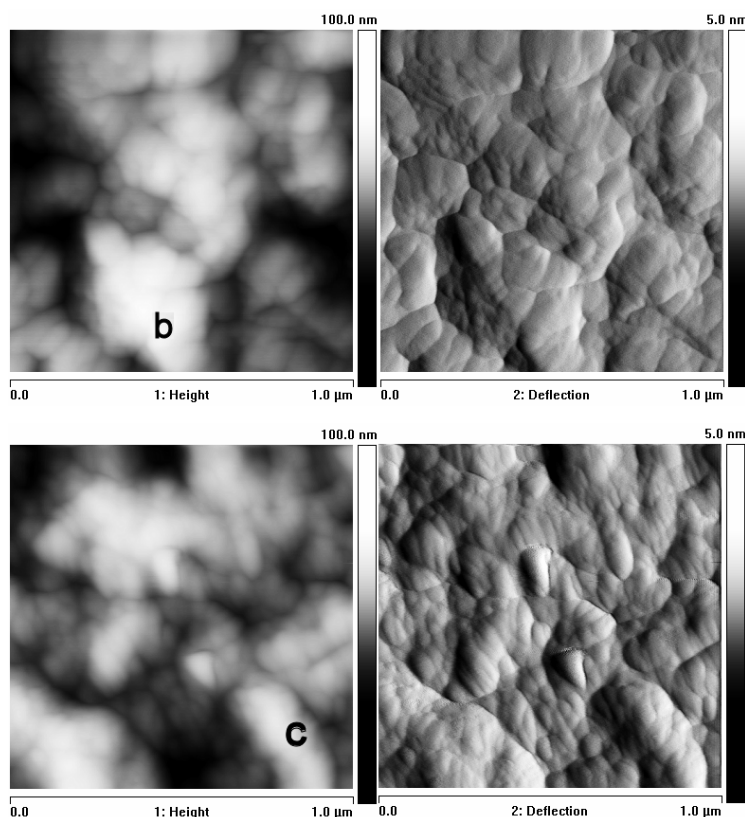


Figure 62. AFM images of the layers deposited at  $j_{\text{total}} = -60 \text{ mA cm}^{-2}$ ; (a) 0mT, (b) 615 mT orientation C, (c) in 715 mT orientation B. Bath 4 (see Table 1, p.39) was used for Ni-Fe alloy electrodeposition.

## IV.5 XRD Analysis

### IV.5.1 Ni-Fe Alloys containing less than 10at.% Fe

In Fig. 63 one can see the results obtained for Ni-Fe alloys with a relatively small iron content (less than 10 at%), in both possible orientations of the working electrode: parallel and perpendicular to gravitation.

Samples deposited at a total current density  $-25 \text{ mA cm}^{-2}$  showed a strong change in the morphology in the presence of a magnetic field (see section IV.4, Fig. 58). One reason for that could be the increase of the hydrogen evolution reaction in a magnetic field. This can induce also a stronger inhibition of the deposition and changes in the texture of the deposited layers.

Two representative samples were chosen for the XRD analysis in the case that the deposition was made without a superimposed magnetic field, in a magnetic field applied perpendicular (0.74T- orientation E, 0.71T- orientation B), respectively parallel to the electric current (0.6T- orientation C) (see Fig. 10, p.38).

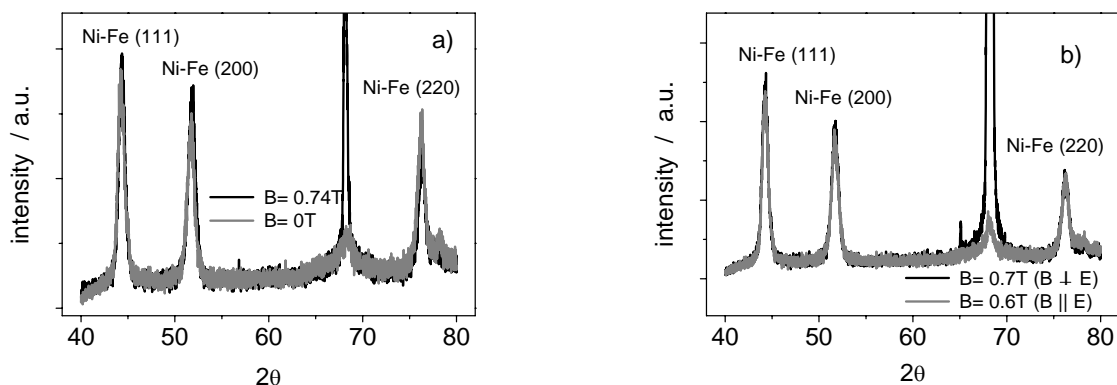


Figure 63. XRD patterns for a Ni-Fe layers deposited from the electrolyte 4 (pH 3), (Table 1, p.39) at  $j = -25 \text{ mA cm}^{-2}$ ; (a) Magnetic field was applied perpendicular to the electric field, orientation E; (b) Magnetic field was applied perpendicular, (orientation B), and parallel (orientation C) to the electric current.

Four peaks could be seen for the range of 2 Theta angles from  $40^\circ$  to  $80^\circ$ . Three are marked in the figure and correspond to a cubic Ni-Fe structure (phase Taenite awaruite, space group 225 (Fm3m), JCPDS no. 23-297, which describes the Ni-Fe alloys with compositions from 100% Ni to 24.81%Ni). The third peak (without indices in Fig. 63) is assigned to the quartz substrate (see Fig. 27). In the following the discussion will focus just on the three peaks corresponding to the cubic structure of Ni-Fe alloy.

The samples deposited in the absence of the magnetic field, as well as the samples deposited in orientations B and C, do not seem to present stress anisotropy. The peaks corresponding to a texture appeared at the same angle. The peak positions for the samples deposited in a magnetic field (in orientation E) were slightly shifted compared to the peak positions of the layers deposited without a magnetic field. For these layers (deposited in a magnetic field in orientation E), the crystalline cell seems to be deformed.

Comparing the intensities obtained for the two conditions (samples deposited in a magnetic field and without magnetic field, (Fig 63A and B) we noticed an increasing tendency of the  $\{111\}$  and  $\{200\}$  textures. The increase of the (200) peak has been reported before in [7], for Ni-Fe deposition from a chloride bath with saccharine and SDS. Remarkably however, one can notice that for the texture  $\{220\}$  the peak intensities for the samples deposited in the B field are smaller than those deposited in  $B=0$ . This effect can be attributed to a suppression of the growth in a magnetic field of the grains with  $\{220\}$  texture [7].



The orientation index (see Table 15) was calculated with Eq. 14. The plane for which the texture index is higher than one gives the preferred orientation. Thus, in the present study it seems to be the (220) plane in absence of a magnetic field and (111) in the presence of a magnetic field applied perpendicular to the electric current. When the magnetic field and the electric field were parallel, the planes (111) and (220) seem to be in almost equal in number. The smallest preferential plane for growth is the (200) plane. However, for the orientation E in a magnetic field the orientation index of this plane is larger than the orientation index of the (220) plane. This can be attributed to the strong changes in morphology that these layers experience in the orientation E in a magnetic field (Fig. 58). The changes in morphology comprise the disappearance of the pores for the Ni-Fe layers electrodeposited in a magnetic field.

Table 15. Orientation index for Ni-Fe alloys electrodeposited from the electrolyte 4 (pH 3.0), (see Table 1, p.39), at  $j = -25 \text{ mA cm}^{-2}$ .

<b>Orientation plan</b>	<b>0mT, orientation E</b>	<b>740mT, orientation E</b>	<b>715mT, orientation B</b>	<b>615mT, orientation C</b>
<b>(111)</b>	0.98 +/-0.05	1.32 +/- 0.05	1.07 +/- 0.01	1.01 +/- 0.01
<b>(200)</b>	0.90 +/- 0.03	1.02 +/- 0.10	0.97 +/- 0.01	0.97 +/- 0.06
<b>(220)</b>	1.19 +/- 0.14	0.72 +/- 0.12	0.90 +/- 0.03	1.03 +/- 0.11

The theoretical pattern in function of the Ni content of the Ni-Fe alloys (phase taenite awaruite) was calculated with the PowderCell program. In this way the composition of the alloy given by EDX can be compared with the composition given by XRD. The differences between the values given by the two methods were smaller than 5%.

Each peak from the pattern was fitted with a Lorentzian. Thus, it was possible to evaluate the grain size with the Debye-Scherrer formula (Eq. 29) [204]:

$$L = \frac{0.9\lambda}{w \cos\theta_c} \quad (\text{Eq. 29})$$

where  $\lambda$  is the wavelength,  $w$  is the full width at half maximum (in radians),  $L$  is the grain size and  $\theta_c$  is the angle satisfying Bragg's law. The results are presented in Table 16.

The instrumental broadening was neglected, which is acceptable for a nanocrystalline material [204]. The stress induced line broadening – if present- should cause a line broadening as the  $2\theta$  angle increases. It was estimated after a standard procedure [205] (strain = FWHM/  $4\tan\theta$ ) and it was found that for our data its contribution is one order of

magnitude smaller than the experimental determined values. The induced stress would contribute  $2 \cdot 10^{-3}$  radians to the FWHM, while the measured values of FWHM were around  $15 \cdot 10^{-3}$  radians.

Table 16. Grain size calculated from the XRD patterns of Ni-Fe layers electrodeposited from the electrolyte 4 (Table 1, p.39), pH 3.0, at  $j_{total} = -25 \text{ mA cm}^{-2}$  for 180 s.

Crystalline plan	L (nm) 0mT, orientation E	L (nm) 611mT, orientation E	L (nm) 740mT, orientation E	L (nm) 715mT, orientation B	L (nm) 615mT, orientation C
(111)	$20.4 \pm 0.3$	$21.8 \pm 0.7$	$22.1 \pm 1.9$	$22.0 \pm 0.3$	$23.0 \pm 0.8$
(200)	$17.4 \pm 2.6$	$19.2 \pm 0.2$	$18.5 \pm 2.5$	$19.1 \pm 0.5$	$17.4 \pm 2.6$
(220)	$21.8 \pm 1.0$	$19.5 \pm 1.4$	$21.7 \pm 3.1$	$21.4 \pm 1.1$	$21.8 \pm 1.0$

The grain size obtained from the XRD patterns was compared to that obtained from the AFM images. The smallest particles that could be identified by the AFM software had 10nm diameter, 13nm length and 13nm width. Notice, however that these were singular events that appear on a surface of  $6.6 \mu\text{m} \times 6.6 \mu\text{m}$ . More particles were recorded usually starting from 14 nm diameter, 20 nm length and 17 nm width (Fig. 64).

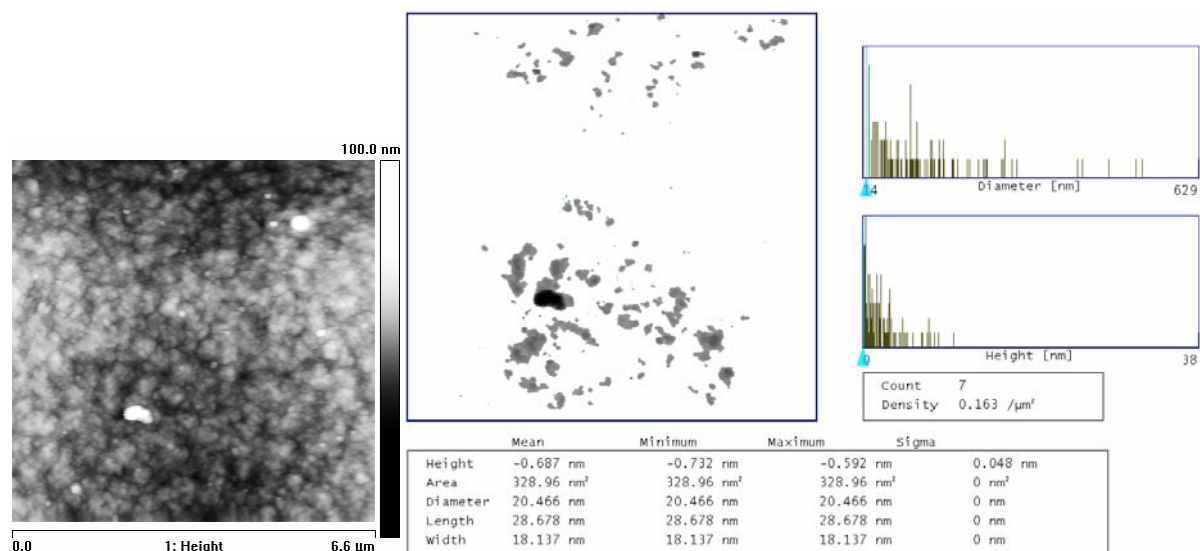


Figure 64. Height image and the corresponding particle analysis for a Ni-Fe layer electrodeposited from electrolyte 4 (Table 1, p.39), pH 3.0, at  $j_{total} = -25 \text{ mA cm}^{-2}$  for 180 s in B=0T.

Due to the formation of particle agglomerations, the AFM software counts the particles with a diameter between 40-90 nm as having the highest frequency of appearance. Calculating the grain size from the XRD patterns one gets the crystal size of individual

grains, while AFM can consider particle agglomerates as individual grains.

The grain size of the (220) oriented grains is comparable to the grain size of the (111) oriented grains. The (200) grains seem to be responsible for more fine grained films. A slightly increasing tendency of the grain size for the grains oriented parallel to the (111) plane could be observed when the magnetic field was applied. In the case of the other two orientations (grains which grow parallel to the (200) and (220) plane), no clear tendency could be observed with the magnetic field.

It has been discussed before (Table 15) that more grains grow in a magnetic field parallel to the planes (111) and (200) in comparison to the case without a magnetic field. The fine grains oriented parallel to the (200) plane will induce the formation of finer grained films. This can explain the slight decrease in the roughness of the layers obtained in a magnetic field (see section IV.4, p.103).

#### IV.5.2 Permalloy

For obtaining the permalloy, galvanostatic depositions were done with a constant total charge density of  $4.5 \text{ C cm}^{-2}$  from an electrolyte containing  $0.5\text{M NiSO}_4$ ,  $0.07\text{M FeSO}_4$ ,  $0.4\text{M H}_3\text{BO}_3$ ,  $\text{pH}=2$ . The thickness of the deposited layer was around  $1.5 \mu\text{m}$ .

In Fig. 65 one can see the effect of the total current density on the orientation index. The error bars represent the standard error of the mean value of at least three measurements.

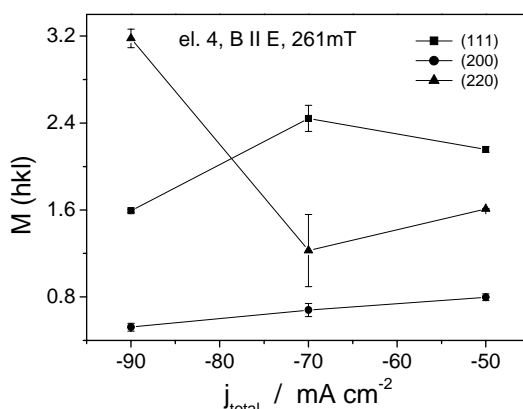


Figure 65. Orientation index in function of the total current density applied. Electrolyte 3 (pH 2.0) was used here (see Table 1, p.39).

The layers deposited at smaller current densities (less than  $-50 \text{ mA cm}^{-2}$ ) grow preferentially parallel to the crystallographic plane (111), while at high current densities, the

preferred plane for growth becomes the (220). The less preferred plane is (200).

At more cathodic potentials the crystallisation occurs more quickly, but more hydrogen is generated at the same time. The important role that the hydrogen has in electro-crystallization processes was pointed out before. On the other hand, according to the two dimensional nucleation theory [95], the deposition overpotential will affect the initial orientation of the 2D grains. Thus with increasing the overpotential the texture will change. For the permalloy, the texture evolution in the current range investigated, is as follows: (111)  $\rightarrow$ (220).

Permalloy samples were deposited at a total current density of  $-50 \text{ mA cm}^{-2}$  in the presence of a magnetic field (Fig. 66). In this case, no clear evolution of the preferred orientation plane could be noticed as a function of the applied magnetic field. However, it has to be mentioned that a (BCC) phase seems to form. A small peak starts to evolve at  $2\theta = 65^\circ$  for the samples that contained more than 30% wt Fe (not shown).

The differences obtained in the XRD patterns of Ni-Fe alloys electrodeposited in a magnetic field can be attributed to the specific effects of a magnetic field. The magnetic field can increase the HER thus increasing the specific adsorption of some inhibiting species. These will inhibit the crystal growth and thus the grain size can be modified. The magnetic field can also lead to a preferential growth of the grains if their easy axis of magnetization is in the direction of the applied field [102]. The additional MHD convection induced by the Lorentz force can be also responsible for the texture evolution [96]. The possible mechanism through which the MHD convection can influence the texture is based on the changes of the surface pH induced by a magnetic field [96a].

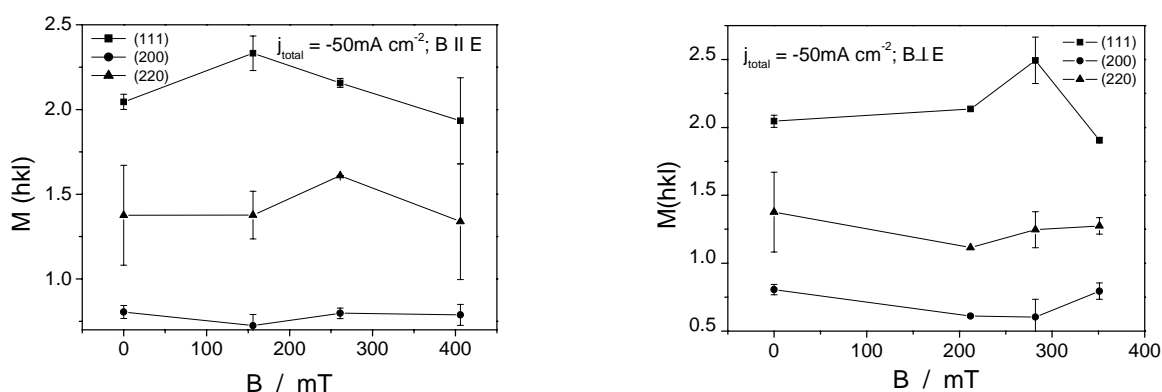


Figure 66. The orientation indices for the layers deposited at  $j_{\text{total}} = -50 \text{ mA cm}^{-2}$  from electrolyte 3 (see Table 1, p.39) (pH 2.0), in function of the magnetic field. Orientations of the cell are here C and B.

## V. Conclusions and Outlook

The key results obtained in this work, which were discussed in detail in the previous sections (III and IV) will now be summarized. A short outlook is given at the end of this section, which contains some ideas for (possible) future work.

The scope of this work was to investigate the effects that a magnetic field can induce during the electrodeposition of Ni and Ni-Fe alloys. Special regard was given to mass transport controlled effects. Magnetic field effects on the nucleation and growth of ferromagnetic layers and on the properties of electrodeposited layers were also investigated.

### ***V.1 Conclusions for Ni Electrodeposition in a Magnetic Field***

#### **V.1.1 Ni Layers Electrodeposited from a dilute Ni Electrolyte**

Nucleation and growth of thin Ni layers on gold electrodes under a superimposed magnetic field were analysed in-situ with the Electrochemical Quartz Crystal Microbalance technique. Cyclic voltammograms showed the potential region where Ni deposition occurs. The deposition rates as a function of the scan rates obtained from experiments were compared to the theoretical ones, predicted by the Randles- Sevcik equation. It was found that the deposition rates calculated from the cyclic voltammograms with a scan rate of  $5 \text{ mV s}^{-1}$  are similar to the theoretical ones, assuming a mass transport controlled process (section III.1.1, p.43).

Potential step experiments were performed from 0.5V to -1V or -1.1V vs. SCE in a dilute Ni electrolyte. Using EQCM one can separate the current due to Ni electrodeposition and the partial current of hydrogen evolution. The shape of the current density of Ni differs strongly from the shape of the total current density (Fig. 17, p.50). Therefore, when discussing the magnetic field effects on the nucleation and growth, just the partial current of Ni has to be considered. One main conclusion was that the interplay between the natural and the MHD convections should be taken into account. Thus, when the Lorentz force and the natural convection act in the same direction, an increase of the partial current due to Ni electrodeposition with the magnetic field was obtained (Fig. 17, p. 50). When they act in opposite directions, the Ni current density was influenced just at the beginning of deposition (first 10 seconds). At longer times, the magnetic field has no effect on the Ni current.

However, the total current ( $j_{Ni} + j_{HER}$ ) decreases with the magnetic field (Fig. 18, p.51).

In the absence of a macroscopic MHD convection, the Ni current density decreases with the magnetic field the first 10-15 seconds of deposition (Fig. 19, p.52). On longer time scales no influence of the magnetic field could be noticed for this configuration.

The Ni mass increases with the magnetic field when the natural and the MHD convections act in the same direction. For the other three orientations analysed, the deposited mass does not vary with the magnetic field (Fig. 20, p.53). Two linear regions were observed in the mass transients. The initial Ni layer grows more quickly than the later one if the deposition was carried out at sufficiently cathodic potentials (-1.1V vs. SCE). The deposition rates were higher in a magnetic field when a MHD convection was present and they were not influenced by a moderate magnetic field if this was applied parallel to the electric current (Table 2, p.54).

Three theoretical models were chosen for characterizing the Ni nucleation in a magnetic field: Scharifker-Hills (SH), Scharifker-Mostany (SM) and Heerman-Tarallo (HT) (section I.5.4, p.26).

When the experimental data were compared with the predictions from the SH model, a transition from instantaneous nucleation (first 10-15 seconds of deposition) to progressive nucleation was noticed. However, in the case that the Lorentz force and the natural convection act in the same direction, the nucleation and growth remained instantaneous during the whole deposition (Table 3, p.57). This is due to the strong additional convection that is generated in this configuration of the cell.

The nucleation site density ( $N_0$ ) and the nucleation rate constant ( $A$ ) were obtained by non-linear least squares fitting of the Ni current density curves using the Levenberg-Marquardt algorithm. The theoretical expression of the current density as a function of  $A$  and  $N_0$  was taken from the two other nucleation models. The fitting with the SM model yielded similar values for  $N_0$  and  $A$ , respectively, independent of the orientation of the working electrode with regard to the magnetic field (Table 4, p.58). As the AFM images proved that more nuclei appear in a magnetic field in the case that the Lorentz force and the natural convection act in the same direction, it was concluded that the SM model is not suitable for fitting the experimental data. The results obtained with the HT model agreed well with those given by the AFM software (Fig. 23, p.59 and Fig. 24, p.61). Thus,  $N_0$  increases with the magnetic field when natural and MHD convections act in the same direction. However, the values of  $A$  indicated that after the current reaches its maximum, the nucleation becomes progressive also in the case that Lorentz force and natural convection act in the same direction. This is in contradiction with the results obtained from SH model, but can be

explained on the basis of the different expressions for the theoretical current density in the two models.

### V.1.2 Ni Layers Electrodeposited from Ni-Sulfamate Electrolytes

Two surfactants were used in the case that Ni was electrodeposited from a sulfamate bath: SDS and sulfirol 8. The effects on the Ni electrodeposition process induced by the simultaneous action of the surfactants and a superimposed magnetic field were analysed.

The presence of the surfactants induced changes of the total current recorded during the cyclic voltammograms. In the presence of surfactants the Ni deposition sets in at less cathodic potentials and the currents corresponding to the Ni dissolution are higher (Fig. 25, p.64). However, the total mass deposited is smaller from an electrolyte with surfactants in comparison to one without surfactants, probably due to the inhibition of the active sites by the adsorbed surfactant (Fig. 26, p.65).

XRD investigations were performed for Ni layers of two thicknesses: 0.5  $\mu\text{m}$  and 5.4  $\mu\text{m}$ . The thin layers present an epitaxial growth. Thus, the preferred crystalline orientation of thin Ni layers was (111), as that of the underlying Au electrode (section III.2.1, p.66). It is known that thicker layers have a preferred crystalline orientation that does not depend on the orientation of the substrate, and that depends just on the experimental conditions (electrolyte, pH, potential of deposition, etc). For the electrolyte used in this study, it was found that the preferred crystalline orientation of thicker Ni layers is (200) (Table 8, p.68).

The effects induced by a magnetic field, which was applied perpendicular to the electric current, on the texture of Ni layers obtained from a sulfamate bath free of surfactants, were investigated. The electrodeposition was done in the galvanostatic mode, at  $j = -5\text{mA cm}^{-2}$ , and the working electrode was fixed at the bottom of the cell, perpendicular to gravity. For these experimental conditions, an increase of the (111) intensity was noticed with increasing magnetic field, for both thin and thicker Ni layers (Fig. 28, p.67). Just in the case of thicker Ni layers the (200) intensity increases with the magnetic field. The reason for this can be the specific adsorption of inhibiting species ( $\text{H}_{\text{ads}}$  or  $\text{Ni}(\text{OH})_2$ ) that is promoted by a magnetic field. No stress anisotropy was noticed for the Ni layers deposited in the presence or absence of a magnetic field. The preferred crystalline orientation of Ni layers does not change when the magnetic field is applied perpendicular to the electric current (Fig. 28, p.67). The effects induced by the magnetic field on the texture are smaller than those induced by variation of the

cathode potential, as observed before for Fe layers by Matsushima et al. [96].

When the magnetic field was applied perpendicular to the electric current, an increase of the HER with the magnetic flux density was noticed at small current densities. At higher current densities, the HER was not influenced by the intensity of the magnetic field (Fig. 29, p.69, Fig. 31, p.71). A model was proposed [171], that explains the influence of the magnetic field at different polarizations. The model is based on the fact that a magnetic field applied perpendicular to the electric current increases the limiting current density. Hydrogen reduction is mass transport controlled, and Ni reduction is activation controlled. Therefore, the magnetic field will increase the limiting current of HER at small polarization. For the electrolytes with surfactants, the increase of the HER with the magnetic field was stronger than that obtained for the electrolytes without surfactants (Fig.30, p.70). This was explained on the basis of reduced surface tension in the electrolytes with surfactants. When the magnetic field was applied parallel to the electric current, no changes of the HER with the intensity of the magnetic field were noticed. This proves the importance of MHD convection in comparison to the paramagnetic and gradient forces (Fig. 29, p.69).

Roundish grains were observed for the thin Ni layers (which had a (111) preferred crystalline orientation) and pyramidal ones for the thicker Ni layers (with a (200) preferred crystalline orientation) (Fig. 34, p.74). The morphology of the deposited layers changes in the presence of surfactants (Fig. 36, p.76). The Ni layers obtained from a sulfamate bath with sulfirol 8 presented larger grains in comparison to the layers deposited from a bath free of surfactants (section III.2.4, p.77). This increase of the grain size was attributed to the incorporation of the surfactant in the deposit.

The morphology of Ni layers obtained from a bath free of surfactant was not influenced by the magnetic flux density (Fig. 36, p.76). Coarser layers were obtained in a magnetic field (applied perpendicular to the electric current) when the electrodeposition was done from an electrolyte with surfactants (Fig. 36, p.76, Table 9, p.78). The number of grains increased with the magnetic field for the Ni layers electrodeposited from a bath free of surfactants and for a bath with SDS. As a consequence, the grain size decreased (Table 9, p.78). In the case of the electrolyte with sulfirol 8, the number of grains decreased with the magnetic field, and their size increased.

The roughness of the Ni layers electrodeposited from a bath with surfactant increased with the magnetic field, while it remains almost constant for the layers deposited from an electrolyte without surfactants (Table 9, p.78; Table 10, p.80). Roughness of the Ni layers did not change with the magnetic field if the electric current and the magnetic field lines were



parallel to each other (Fig. 40, p.82).

The influence of the magnetic field (that was applied perpendicular to the electric current) on the grain size and roughness of the layers can be attributed to the MHD effect. As an additional fact, the magnetic field seems to favour the incorporation of the surfactants in the deposit, inducing in this way coarser layers.

No anisotropy of the magnetic properties was found if the Ni layers were deposited in a magnetic field (section III.2.5, p.84).

## ***V.2 Conclusions for Ni-Fe Alloys Electrodeposition in a Magnetic Field***

The potential when the depositions of Ni, Fe and Ni-Fe alloys set in was identified from cyclic voltammograms (Fig. 43, p.87). At the same time, the potential region where the HER occurs was determined. Slightly higher hydrogen partial currents were observed in the case that Fe ions were present in the electrolytes (pH 2-3), due to lower overpotential of hydrogen on the Fe than on the Ni layers (Fig. 44, p.88).

The cyclic voltammograms that were recorded when the magnetic field was applied perpendicular to the electric current, showed an increase of the HER. At the same time, the inhibition of the alloy deposition with the magnetic field was observed at cathodic potentials (Fig. 49, p.92). This inhibition was explained on the basis of the MHD effect on the diffusion controlled processes (see the discussions for Fig. 49, p.92).

For galvanostatic depositions, the Fe content of the alloys decreases with increasing current density. However, the Fe/Ni ratio, expressed in atomic percents, is higher in the layer compared to the ratio in the electrolyte (Fig. 50, p.94) (Fig. 54, p.100). This behaviour is specific for the systems that show an anomalous codeposition. Anomalous codeposition means that the less noble metal (iron) is deposited preferentially compared to the more noble one (nickel).

The interplay between the natural and MHD convections proved to be important during Ni-Fe alloy deposition, too. When the Lorentz force and the natural convection act in the same direction, an increase of the Fe content of the alloys with the magnetic field was observed. When the Lorentz force was perpendicular to the natural convection, no significant changes were observed in the composition of the layers. The alloy composition did not change with the magnetic field when the electric current was parallel to the magnetic field lines

(Table 13, p.98).

The HER increases with the magnetic field when MHD convection was present, and does not change when the magnetic field was parallel to the electric current (Fig. 55, p.101). Optical microscopy images showed that the hydrogen bubbles were circular in the absence of the MHD convection and that they presented a tail when a Lorentz force was present (Fig. 56, p.101). The direction of the tail depends on the net force induced by the natural and MHD convections.

In the absence of a magnetic field, porous layers were obtained in the case that the working electrode was fixed perpendicular to the gravity (Figs. 58 and 59, p.104). In this case, the Fe content of the alloys was ca. 5at %. The pore formation is due to the fact that the hydrogen bubbles can stay long enough on the electrode surface to induce the formation of voids. If a magnetic field is applied perpendicular to the electric current, more uniform layers were observed. At the same time, the porosity of the layers disappears (Figs. 58 and 59, p.104). The morphology of the deposited layers did not change when the magnetic field lines were applied parallel to the electric current (Fig. 61, p.105). However, the roughness of the layers deposited in a magnetic field was smaller than that of the layers deposited in the absence of a magnetic field (Table 14, p.106). This decrease of roughness was attributed to the effects of micro and macro MHD convection on the nucleation and growth of thin layers.

Smaller grains were observed when the magnetic field was applied perpendicular to the electric current. At the same time, these grains were elongated in the direction of the Lorentz force. Circular grains were obtained in the absence of the MHD convection (Fig. 62, p.107). The alignment of the grains in the direction of the Lorentz force is a direct consequence of the MHD convection.

For the Ni-Fe alloys, which contained less than 10 at% Fe, the preferred crystalline orientation changes from (220), in the absence of a magnetic field, to (111), (when the magnetic field was applied perpendicular to the electric current). When the magnetic field lines were parallel to the electric current, both the (111) and (220) textures were preferred in almost the same proportion (Table 15, p.109). In the case of the Ni-Fe alloys with approximately 20 at% Fe, no effect of the magnetic field could be noticed on the texture of the deposits (Fig. 66, p.112). However, the preferred crystalline orientation changed with the total current density (Fig. 65, p.111). The effects of a magnetic field on the texture of Ni-Fe layers were explained on the basis of the MHD convection (section IV.5, p.107).

As a general conclusion of this work it can be said that the magnetic field applied perpendicular to the electric current influences the mass transport processes. Thus, an increase of the partial current of Fe and of the HER was obtained. The grain size, texture, morphology and roughness of the deposited layers depend on the direction and intensity of the magnetic field. The interplay between the natural and MHD convection proved to be important in determining the properties of the ferromagnetic layers. No anisotropy of the magnetic properties was noticed for thin Ni layers electrodeposited in a magnetic field. The nucleation and growth of Ni layers is influenced by the intensity and direction of the magnetic field.

Choosing the right experimental condition, one can improve the morphology and the properties of the deposited layers by applying a magnetic field. At the same time, the magnetic properties of ferromagnetic layers can be improved. An interesting future aspect is to study how the magnetic field modifies the magnetic properties of the Ni based layers. Thus, novel magnetic materials could be developed. The effect of the magnetic field on the mass transport can be used to increase the deposition rates of different metals. At the same time, external magnetic fields can be used to obtain more uniform and finer grained layers. This characteristic can be used for example when the electrodeposition is carried out in nanostructures, as well as on macroelectrodes. All in all it can be stated that Magnetohydrodynamics in electrochemistry is and will remain a promising and fascinating field.



## VI. References

- [1] J. B. Heywood, *Physics Education* **3** (1968) 260-265.
- [2] T.Z. Fahidy, *J. Appl. Electrochem.* **13** (1983) 553-563.
- [3] R. A. Tacke, L. J. J. Janssen, *J. Appl. Electrochem.* **25** (1995) 1-5.
- [4] S. -K. Kim, D. Josell, T. P. Moffat, *J. Electrochem. Soc.* **153** (2006) C826-C833.
- [5] S. R. Brankovic, N. Vasiljevic, T. J. Klemmer, e. C. Johns, *J. Electrochem. Soc.* **152** (2005) C196-C202.
- [6] K. Msellak, J.-P. Chopart, O. Jbara, O. Aaboubi, J. Amblard, *J. Magn. Magn. Mater.* **281** (2004) 295-304.
- [7] I. Tabakovic, S. Riemer, V. Vas'Ko, V. Sapozhnikov, M. Kief, *J. Electrochem. Soc.* **150** (2003) C635-C640.
- [8] T. Z. Fahidy, *Prog. Surf. Sci.* **68** (2001) 155-188.
- [9] L. Yang, *J. Electrochem. Soc.* **101** (1954) 456.
- [10] O. Devos, A. Olivier, J.-P. Chopart, O. Aaboubi, G. Maurin, *J. Electrochem. Soc.* **145** (1998) 401-405.
- [11] A. Chiba, K. Kitamura, T. Ogawa, *Surf. Coat. Technol.* **27** (1986) 83-88.
- [12] A. L. Danilyuk, V. I. Kurmashev, A. L. Matyushkov, *Thin Solid Films* **189** (1990) 247-255.
- [13] E. Brillas, J. Rambla, J. Casado, *J. Appl. Electrochem.* **29** (1999) 1367-1376.
- [14] K. Msellak, *Electrodéposition métallique sous contról MHD. Caractérisation physique et électrochimique*, Dissertation University of Reims, 2003.
- [15] A. Krause, *Elektrokristallisation von Kobalt und Kupfer unter Einwirkung homogener Magnetfelder*, Dissertation Dresden University of Technology, 2006.
- [16] G. A. Di Bari, chapter 3 in *Modern Electroplating*, Edited by M. Schlesinger and M. Paunovic, John Wiley & Sons, Inc. 4-th edition, New York, 2000.
- [17] T. E. Buchheit, D. A. LaVan, J. R. Michael, T. R. Christenson, and S. D. Leith, *Metall. Mater. Trans. A* **33A** (2002), 539-554.
- [18] W. Ehrfeld, *Electrochim. Acta* **48** (2003), 2857-2868.
- [19] A. Brenner, *Electrodeposition of Alloys. Principles and Practice*, Vol. 1 and 2, Academic Press, New York and London, 1963.
- [20] H. Dahms, I. M. Croll, *J. Electrochem. Soc.* **112** (1965) 771-775.
- [21] S. Hessami, C. W. Tobias, *J. Electrochem. Soc.* **136** (1989) 3611-3616.

- [22] M. Matlosz, *J. Electrochem. Soc.* **140** (1993) 2272-2279.
- [23] D. Landolt, *Electrochim. Acta* **39** (1994) 1075-1090.
- [24] T. Krause, L. Arulnayagam, M. Pritzker, *J. Electrochem. Soc.* **144** (1997) 960-969.
- [25] W. Plieth, *Z. Physikal. Chem.* **217** (2003) 383-393.
- [26] W. Plieth, *J. Solid State Electrochem.* **8** (2004) 338-345.
- [27] G. S. Georgiev, V. T. Georgieva, W. Plieth, *Electrochim. Acta* **51** (2005) 870-876.
- [28] W. Plieth, G. G. Georgiev, *J. Solid State Electrochem.* **9** (2005) 859-864.
- [29] W. Plieth, *Electrochim. Acta* **52** (2006) in press.
- [30] J. Horkans, *J. Electrochem. Soc.* **128** (1981) 45-49.
- [31] N. Zech, D. Landolt, *Electrochim. Acta* **45** (2000) 3461-3471.
- [32] G. Lu, P. Evans, G. Zangari, *J. Electrochem. Soc.* **150** (2003) A551-A557.
- [33] V.C. Kieling, *Surf. Coat. Tech.* **96** (1997) 135-139.
- [34] P. L. Cavallotti, B. Bozzini, L. Nobili, G. Zangari, *Electrochim. Acta* **39** (1994) 1123-1131.
- [35] *Modern Electroplating*, 4th Edition, edited by M. Schlesinger and M. Paunovic, John Wiley & Sons, INC., 2000, pp. 140, 468.
- [36] *Nickel and chromium plating*, J. K. Dennis, T. E. Such, Ed. Newnes-Butterworths, London, 1972.
- [37] R. Oriňáková, A. Turoňová, D. Kladeková, M. Gálová, R. M. Smith, *J. Appl. Electrochem.* **36** (2006) 957-972 and references within.
- [38] J. Koryta, J. Dvořák, L. Kavan, *Principles of Electrochemistry*, 2-nd Edition, John Wiley and Sons, Belfast, UK, 1993, pp. 354.
- [39] E. Gileadi, *Electrode Kinetics for Chemists, Chemical Engineers and Material Scientists*, VCH, Weinheim, Germany, 1993, p. 164.
- [40] S.N. Srimathi, S. M. Mayanna and B. S. Sheshadri, *Surf. Technol.* **16** (1982) 277-322.
- [41] M. Alper, H. Kockar, H. Kuru, T. Meydan, *Sens. Actuators A Phys.* **129** (2006) 184-187.
- [42] H. Kockar, M. Alper, H. Kuru, T. Meydan, *J. Magn. Magn. Mater.* **304** (2006) e736-e738.
- [43] D. A. Buttry, M. D. Ward, *Chem. Rev.* **92** (1992) 1355-1379.
- [44] R. Schumacher, *Chem. Userer Zeit* **33** (1999) 268-278.
- [45] C. Behling, *The non-gravimetric response of thickness shear mode resonators for sensor applications*, Dissertation University Magdeburg, 1999.
- [46] A. Bund, *Die Quarzmikrowaage in Rheologie und Elektrochemie : Fortschritte in der*

- Signalwertung durch Netzwerkanalyse*, Dissertation Saarbrücken University 1999.
- [47] A. Bund, G. Schwitzgebel, *Electrochim. Acta* **45** (2000) 3703-3710.
- [48] A. Bund, *J. Solid State Electrochem.* **8** (2004) 182-186.
- [49] L. Daikhin, and M. Urbakh, *Langmuir* **12** (1996) 6354-6360.
- [50] V. Tsionsky, L. Daikhin, M. Urbakh, E. Gileadi, in *Electroanalytical Chemistry. A series of advances*, Vol. 22, edited by Allen. J. Bard and Israel Rubinstein, Marcel Dekker, New York, 2004.
- [51] T. Fahidy, chapter 5 in *Modern aspects of electrochemistry*, Nr. 32 (1999), edited by B. E. Conway et al. Kluwer Academic / Plenum Publishers, New York, 333-354.
- [52] C. O'Reilly, G. Hinds, J.M.D. Coey, *J. Electrochem. Soc.* **148** (2001) C674-C678.
- [53] S. Ragsdale, K.M. Grant, H.S. White, *J. Am. Chem. Soc.* **120** (1998) 13461-13648.
- [54] O. Lioubashevski, E. Katz, I. Willner, *J. Phys. Chem. B* **108** (2004) 5778-5784.
- [55] N. Leventis, M. Chen, X. Gao, M. Canals, P. Zhang, *J. Phys. Chem. B* **102** (1998) 3512-3522.
- [56] R. Aogaki, *Trans. Mater. Res. Soc. Jpn.* **25** (2000) 59-63.
- [57] N. Leventis and X. Gao, *J. Phys. Chem. B* **103** (1999) 5832-5840.
- [58] J. P. Chopart, J. Douglade, P. Fricoteaux and A. Olivier, *Electrochim. Acta* **36** (1991) 459-463.
- [59] S. R. Ragsdale, J. Lee, X. Gao, and H. White, *J. Phys. Chem.* **100** (1996) 5913-5922.
- [60] N. Leventis, X. Gao, *J. Am. Chem. Soc.* **124** (2002) 1079-1088.
- [61] N. Leventis, A. Dass, *J. Am. Chem. Soc.* **127** (2005) 4988-4989.
- [62] R. N. O'Brien, K. S. V. Santhanam, *J. Appl. Electrochem.*, **27** (1997) 573-578.
- [63] M. Waskaas, Y. I. Kharkats, *J. Phys. Chem. B*, **103** (1999) 4876-4883.
- [64] J.M.D. Coey, and G. Hinds, *J. Alloy. Comp.* **326** (2001) 238-245.
- [65] C. Iwakura, T. Edamoto, H. Tamura, *Denki Kagaku* **52** (1984) 596-601.
- [66] R. Aogaki, *Magnetohydrodynamics* **39** (2003) 453-460.
- [67] R. Morimoto, A. Sugiyama, R. Aogaki, *Electrochemistry* **72** (2004) 421-423.
- [68] J. C. Shannon, Z. H. Gu, T. Z. Fahidy, *J. Appl. Electrochem.* **29** (1999) 577-584.
- [69] P. U. Arumugam, E. A. Clark, I. Fritsch, *Anal. Chem.* **77** (2005) 1167-1171.
- [70] H. Matsushima, T. Nohira, Y. Ito, *Electrochem. Solid-State Lett.* **7** (2004) C81-C83.
- [71] R. Aogaki, *J. Chem. Phys.* **103** (1995) 8602-8615.
- [72] E. J. Kelly, *J. Electrochem. Soc.* **124** (1977) 987-994.
- [73] O. Devos, O. Aaboubi, J.-P. Chopart, A. Olivier, C. Gabrielli, B. Tribollet, *J. Phys. Chem. A* **104** (2000) 1544-1548.

- [74] O. Devos, O. Aaboubi, J. P. Chopart, E. Merienne, A. Olivier, J. Amblard, *J. Electrochem. Soc.* **145** (1998) 4135-4139.
- [75] O. Devos, O. Aaboubi, J. P. Chopart, E. Merienne, A. Olivier, C. Gabrielli, B. Tribollet, *J. Phys. Chem. B* **103** (1999) 496-501.
- [76] A. Olivier, J. P. Chopart, J. Douglade, C. Gabrielli, B. Tribollet, *J. Electroanal. Chem.*, **227** (1987), 275-279.
- [77] G. Hinds, F. E. Spada, J. M. D. Coey, T. R. Ni Mhiocháin, M. E. G. Lyons, *J. Phys. Chem. B*, **105** (2001), 9487-9502.
- [78] N. Ibl, W. Rüegg, G. Trümpler, *Helvetica Chimica Acta*, **37** (1953), fasciculus VI-no. 201, 1624-1630.
- [79] C. Wagner, *Trans. Electrochem. Soc.* **95** (1949) 161-173.
- [80] T. Z. Fahidy, *Chem. Eng. J.* **7** (1974) 21-27.
- [81] M. S. Quraishi, T. Z. Fahidy, *Electrochim. Acta* **25** (1980) 591-599.
- [82] D. A. Bograchev, V. M. Volgin, A. D. Davydov, *Russian J. Electrochem.* **41** (2005) 1197-1204.
- [83] V. M. Volgin, A. D. Davydov, D. A. Bograchev, *Russian J. Electrochem.* **41** (2005) 925-932.
- [84] M. Morisue, Y. Fukunaka, E. Kusaka, R. Yshii, K. Kuribayashi, *J. Electroanal. Chem.* **559** (2003) 155-163.
- [85] Y. Oshikiri, M. Sato, A. Yamada, R. Aogaki, *Jpn. J. Appl. Phys.* **43** (2004) 3596-3604.
- [86] Y. Awakura, Y. Takenaka, Y. Kondo, *Electrochim. Acta* **21** (1976) 789-797.
- [87] M. Ota, S. Izuo, K. Nishikawa, Y. Fukunaka, E. Kusaka, R. Ishii, J. R. Selman, *J. Electroanal. Chem.* **559** (2003) 175-183.
- [88] K. Nishikawa, Y. Fukunaka, T. Sakka, Y. H. Ogata, J. R. Selman, *J. Electroanal. Chem.* **584** (2005) 63-69.
- [89] S. Chikazumi, *Physics of Ferromagnetism*, second edition, Clarendon Press, Oxford, 1997.
- [90] *Magnétisme. II- Matériaux et Applications*, Ed. by Étienne du Trémolet de Lacheisserie, Grenoble Sciences, 2000, p. 99, 446.
- [91] S. Bodea, L. Vignon, R. Ballou, P. Molho, *Phys. Rev. Lett.* **83** (1999) 2612-2615.
- [92] R. Brendel, *IEEE Trans. UFFC*, vol. **43** (1996), no. 5, pp. 818-831.
- [93] M. Thompson, S. M. Ballantyne, L.-E. Cheran, A. C. Stevenson, C. R. Lowe, *Analyst* **128** (2003) 1048-1055.
- [94] R. Glocker and E. Kaupp, *Z. Phys. A (Hadrons and Nuclei)* **24** (1924) 121-139.



- [95] N. A. Pangarov, *J. Electroanal. Chem.* **9** (1965) 70-85.
- [96] H. Matsushima, T. Nohira, I. Mogi, Y. Ito, *Surf. Coat. Tech.* **179** (2004) 245-251. a) private discussions.
- [97] S. Yoshimura, S. Yoshihara, T. Shirakashi, E. Sato, *Electrochim. Acta* **39** (1994) 589-595.
- [98] J. Amblard, I. Epelboin, M. Froment, G. Maurin, *J. Appl. Electrochem.* **9** (1979) 233-242.
- [99] A. K. N. Reddy, *J. Electroanal. Chem.* **6** (1963) 141-152.
- [100] H. Fischer, *Electrodepos. Surface Treat.* **1** (1972/73) 319-337.
- [101] J. Amblard, M. Froment, N. Spyrellis, *Surf. Techn.* **5** (1977) 205-234.
- [102] D. Y. Li, J. A. Szpunar, *J. Matt. Sci.* **28** (1993) 5554-5559.
- [103] D. Y. Li, J. A. Szpunar, *Electrochim. Acta* **42** (1997) 37-45.
- [104] D. Y. Li, J. A. Szpunar, *Electrochim. Acta* **42** (1997) 47-60.
- [105] B. Bozzini, *Mater. Chem. Phys.* **66** (2000) 278-285.
- [106] L. Muresan, L. Oniciu, M. Froment, G. Maurin, *Electrochim. Acta* **37** (1992) 2249-2254.
- [107] B. E. Conway, J. O.'M. Bockris, *Plating* **46** (1959) 371-383.
- [108] T. Erdey-Grúz, M. Volmer, *Z. Physikal. Chem. A* **157** (1931) 165-181; 182-187.
- [109] M. Avrami, *J. Chem. Phys.* **7** (1939) 1103-1112; **8** (1940) 212-224; **9** (1941) 177-184.
- [110] H. Fischer, *Elektrolytische Abscheidung und Elektrokristallisation von Metallen*, Springer-Verlag, Berlin/Göttingen/Heidelberg, 1954.
- [111] E. Budevski, G. Staikov, W. J. Lorenz, *Electrochemical Phase Formation and Growth: An introduction to the Initial Stages of Metal Deposition*, VCH, Weinheim (Germany), 1996.
- [112] K. A. Jackson, *Kinetic Processes. Crystal Growth, Diffusion, and Phase Transitions in Materials*, Wiley-VCH, Weinheim (Germany) 2004.
- [113] K. J. Vetter, *Electrochemical Kinetics. Theoretical and experimental aspects*, Academic Press, New York, 1967; a) p. 538.
- [114] R. Kaischew, B. Mutaftschiew, *Electrochim. Acta* **10** (1965) 643-650.
- [115] M. Fleischmann, H. R. Thirsk, *Electrochim. Acta* **2** (1960) 22-49.
- [116] O. M. Magnussen, F. Möller, M. R. Vogt, R. J. Behm in *Electrochemical Nanotechnology: In-situ Local Probe Techniques at Electrochemical Interfaces*, ed. W. J. Lorenz and W. Plieth, Wiley-VCH, Weinheim (Germany), 1998.
- [117] A. Lachenwitzer, O. M. Magnussen, *J. Phys. Chem. B* **104** (2000) 7424-7430.

- [118] A. Krause, M. Uhlemann, A. Gerbert, L. Schultz, *Thin Solid Films* **515** (2006) 1694-1700.
- [119] M. Fleischmann, S. K. Rangarajan, H. R. Thirsk, *Trans. Faraday Soc.* **63** (1967) 1240-1260.
- [120] M. V. Mirkin, A. P. Nilov, *J. Electroanal. Chem.* **283** (1990) 35-51.
- [121] L. Heerman, A. Tarallo, *J. Electroanal. Chem.* **470** (1999) 70-76.
- [122] B. Scharifker, J. Mostany, *J. Electroanal. Chem.* **177** (1984) 13-37.
- [123] M. Sluyters-Rehbach, J. H. O. J. Wijenberg, E. Bosco, J. H. Sluyters, *J. Electroanal. Chem.* **236** (1987) 1-20.
- [124] G. Gunawardena, G. Hills, I. Montenegro, B. Scharifker, *J. Electroanal. Chem.* **138** (1982) 225-239.
- [125] B. Scharifker, G. Hills, *Electrochim. Acta* **28** (1983) 879-889.
- [126] A. Azizi, A. Sahari, M. L. Felloussia, G. Schmerber, C. Mény, A. Dinia, *Appl. Surf. Sci.* **228** (2004) 320-325.
- [127] M. E. Hyde, R. G. Compton, *J. Electroanal. Chem.* **549** (2003) 1-12.
- [128] W. J. Plieth, *J. Phys. Chem.* **86** (1982) 3166-3170.
- [129] B. R. Scharifker, J. Mostany, M. P. Pardavé, I. González, *J. Electrochem. Soc.* **146** (1999) 1005-1012.
- [130] L. Heerman, E. Matthijs, S. Langerock, *Electrochim. Acta* **47** (2001) 905-911.
- [131] *PLO technical manual* from Maxtek, USA
- [132] *Network Analyser Basics*, manual from Agilent Technologies, 2004, USA.
- [133] *AFM User's Manual* from Digital Instruments Inc., Santa Barbara, USA.
- [134] *Scanning Electron Microscopy and X-Ray Microanalysis*, second edition, Joseph I. Goldstein, Dale E. Newburg, Patrick Echlin, David C. Joy, Charles Fiori, Eric Lifshin, Plenum Press, New York and London, 1984.
- [135] *Scanning Electron Microscopy*, Oliver C. Wells, Alan Boyde, Eric Lifshin, Alex Rezanowich, McGraw-Hill Book Company, 1974.
- [136] *Scanning Electron Microscopy and X-Ray Microanalysis*, Grahame Lawes, Ed. John Wiley & Sons, Chichester, 1987.
- [137] *X-Ray Characterization of Materials*, Edited by Eric Lifshin, Wiley-VCH, Weinheim, 1999.
- [138] *Physical Electrochemistry. Principles, Methods, and Applications*, Edited by Israel Rubinstein, Marcel Dekker, Inc. New York 1995, p.351.
- [139] *Transmission Electron Microscopy and Diffractometry of Materials*, second edition,

- B. Fultz, J. M. Howe, Springer, Berlin 2002.
- [140] R. Brugger, *Die galvanische Vernicklung*, 2-nd Edition, Eugen G. Leuze, Saulgau, Germany (1984), p. 118.
- [141] L. Anicai, A. Petrica, L. Dima, *Chemistry Preprint Server, Physical Chemistry* (2003), **1-7**, CPS:physchem/0311003, <http://preprint.chemweb.com/physchem/0311003>
- [142] P. Duke, T. Montelbono, and L. Missel, *Plating Surf. Finish.* **69** (1982), 61-65.
- [143] *Electrochemical Methods. Fundamentals and Applications*, 2-nd Edition, Edited by Allen J. Bard and Larry R. Faulkner, John Wiley & Sons, Inc., New York, 2001, pp. 163, 231, 236.
- [144] V. Tsionsky, L. Daikhin, E. Gileadi, *J. Electrochem. Soc.* **143** (1996) 2240-2245.
- [145] C. Q. Cui, J. Y. Lee, *Electrochim. Acta* **40** (1995) 1653-1662.
- [146] M. Fleischmann, A. Saraby-Reintjes, *Electrochim. Acta* **29** (1984) 69-75.
- [147] H. Deligianni, L. T. Romankiw, *IBM J. Res. Develop.* **37** (1993) 85-95.
- [148] J. Matulis, R. Sližys, *Electrochim. Acta* **9** (1964) 1177-1188.
- [149] W. Davison, J. A. Harrison, *Electroanal. Chem. Interfacial Electrochem.* **44** (1973) 431-443.
- [150] J. L. Bubendorff, L. Cagnon, V. Costa-Kieling, J. P. Bucher, P. Allongue, *Surf. Sci.* **384** (1997) L836-L843.
- [151] E. B. Saubestre, *Plating* **45** (1958) 927-936.
- [152] M. Benje, M. Eiermann, U. Pittermann, K. G. Weil, *Ber. Bunsenges. Phys. Chem.* **90** (1986) 435-439.
- [153] M. W. Carr, A. R. Hillman, S. D. Lubetkin, M. J. Swann, *J. Electroanal. Chem.* **267** (1989) 313.
- [154] J. Amblard, M. Froment, G. Maurin, N. Spyrellis, E. Trevisan-Souteyrand, *Electrochim. Acta* **28** (1983) 909-915.
- [155] M. Y. Abyaneh, M. Fleischmann, *J. Electroanal. Chem.* **119** (1981) 187-208.
- [156] Ž. Petrović, M. Metikoš-Huković, Z. Grubač, S. Omanović, *Thin Solid Films* **513** (2006) 193-200.
- [157] G. Hinds, J.M.D. Coey, M.E.G. Lyons, *Electrochem. Comm.* **3** (2001) 215-218.
- [158] W. H. Press, S. A. Teukolsky, W. T. Vetterling, B. P. Flannery, *Numerical Recipes in C++. The Art of Scientific Computing*, 2-nd Edition, Cambridge University Press, UK, 2002, chapter 15.5.
- [159] K.-D. Song, K.B. Kim, S.H. Han, and H.K. Lee, *Electrochem. Comm.* **5** (2003) 460-

- 466.
- [160] Y.-P. Lin, J. R. Selman, *J. Electrochem. Soc.* **140** (1993) 1299-1303.
- [161] E. Michaelis, D. Wöhrle, J. Rathousky, M. Wark, *Thin Solid Films* **497** (2006) 163-169.
- [162] E. A. Marquis, A. A., J. J. Kelly, S. H. Goods, J. R. Michael, *J. Appl. Electrochem.* **36** (2006) 669-676.
- [163] S. H. Goods, J. J. Kelly, A. A. Talin, J. R. Michael, R. M. Watson, *J. Electrochem. Soc.* **153** (2006) C325.
- [164] A. A. Rasmussen, P. Møller, M. A. J. Somers, *Surf. Coat. Technol.* **200** (2006) 6037-6046.
- [165] G. I. Finch, C. H. Sun, *Trans. Faraday Soc.* **32** (1936) 852-863.
- [166] G. I. Finch, A. L. Williams, *Trans. Faraday Soc.* **33** (1937) 564-569.
- [167] G. I. Finch, H. Wilman, L. Yang, *Faraday Soc. Discussions* **1** (1947) 144-158.
- [168] E. Wicke, and G. H. Nernst, *Ber. Bunsenges.*, **68** (1964), 224-235.
- [169] M.H. Abd Elhamid, B.G. Ateya, and H.W. Pickering, *J. Electrochem. Soc.* **144** (1997), L58-L61.
- [170] T. Mizuno, M. Enyo, in R. E. White, et al. (Eds.), *Modern Aspects of Electrochemistry*, vol. **30**, Plenum Press, New York, 1996, 415-503.
- [171] A. Bund, A. Ispas, *J. Electroanal. Chem.* **575** (2005) 221-228.
- [172] R.K. Dorsch, *J. Electroanal. Chem.* **21** (1969), 495-508.
- [173] C. Arkam, V. Bouet, C. Gabrielli, G. Maurin, H. Perrot, *J. Electrochem. Soc.* **141** (1994), L103-L105.
- [174] O. Aaboubi, J. P. Chopart, J. Douglade, A. Olivier, C. Gabrielli, B. Tribollet, *J. Electrochem. Soc.* **137** (1990) 1796-1804.
- [175] K.K. Kanazawa, J.G. Gordon II, *Anal. Chim. Acta* **175** (1985), 99-105.
- [176] L. Daikhin, E. Gileadi, G. Katz, V. Tsionsky, M. Urbakh, D. Zagidulin, *Anal. Chem.* **74** (2002), 554-561.
- [177] D.S. Stevens, H. F. Tiersten, and B. K. Sinha, *J. Appl. Phys.* **54** (1983), 1704-1716.
- [178] C.A. Cousins, J. Dash, and C. Gorg, *J. Appl. Phys.* **55** (1984), 2606-2608.
- [179] A. Bund, M. Schneider, *J. Electrochem. Soc.* **149** (2002) E331-E339.
- [180] A. Bund, A. Ispas, W. Plieth, *Electrochemical Society Proceedings Volume 2004-23, Proceedings of the International Symposium Magnetic Materias, Processes, and Devices VIII*, Pennington, New Jersey, USA (2006) 444-453.
- [181] U. Retter, M. Tchachnikova, *J. Electroanal. Chem.* **550-551** (2003) 201-208.

- [182] A. Gomes, M. I. da Silva Pereira, *Electrochim. Acta* **52** (2006) 863-871.
- [183] J. F. Rusling, *Colloids Surf.* **123-124** (1997) 81-88.
- [184] C. Madore, D. Landolt, *J. Electrochem. Soc.* **143** (1996) 3936-3943.
- [185] A. Bund, S. Koehler, H. H. Kuehnlein, W. Plieth, *Electrochim. Acta* **49** (2003) 147-152.
- [186] Y. G. Li, A. Lasia, *J. Appl. Electrochem.* **27** (1997) 643-650.
- [187] C. -C. Hu, C. -M. Wu, *Surf. Coat. Technol.* **176** (2003) 75-83.
- [188] H. Matsushima, Y. Fukunaka, Y. Ito, A. Bund, W. Plieth, *J. Electroanal. Chem.* **587** (2006) 93-98.
- [189] W. Schwarzacher, *J. Phys. Condens. Matter* **16** (2004) R859-R880.
- [190] A. Ispas, A. Bund, *Proceeding of the Joint 15th Riga and 6th Pamir International Conference on Fundamental and Applied MHD*, Riga Jurmala, Latvia, (2005), volume 2, 135-138.
- [191] C.-P. Chen, and J. Jorne, *J. Electrochem. Soc.* **138** (1991), 3305-3311.
- [192] V. Heresanu, R. Ballou, P. Molho, *J. Magn. Magn. Mater.* **272-276** (2004) 2439-2441.
- [193] H. Matsushima, T. Nohira, I. Mogi, Y. Ito, *Surf. Coat. Tech.* **179** (2004) 245-251.
- [194] V. Madurga, J. J. Vergara, C. Favieres, *J. Magn. Magn. Mater.* **272-276** (2004) 1681-1683.
- [195] J. Horkans, *J. Electrochemical Soc.* **126** (1979) 1861-1867.
- [196] E. Juzeliunas, K. Jüttner, *Electrochim. Acta* **43** (1998) 1691-1696.
- [197] A. Ispas, A. Bund, H. Matsushima, F. Bogani, B. Bozzini, *ECS Transaction - Cancun Volume 3, "Magnetic Materials Processes, and Devices 9"*, accepted to be published early 2007.
- [198] A. Ispas, H. Matsushima, W. Plieth, A. Bund, *Electrochim. Acta* **52** (2007) 2785-2795.
- [199] P. C. Andricacos, C. Arana, J. Tabib, J. Dukovic, L. T. Romankiw, *J. Electrochem. Soc.* **136** (1989) 1336.
- [200] N. Zech, E. J. Podlaha, L. Landolt, *J. Electrochem. Soc.* **146** (1999) 2829.
- [201] I. Ohno, M. Mukai, *Electrodep. Surf. Treat.* **3** (1975) 213.
- [202] Y. Oshikiri, M. Sato, A. Yamada, R. Aogaki, *Electrochemistry* **71** (2003) 154-162.
- [203] A. Bund, G. Schwitzgebel, *Anal. Chim. Acta* **364** (1998) 189-194.
- [204] X. Liu, G. Zangari, M. Shamsuzzoha, *J. Electrochem. Soc.* **150** (2003) C159-C168.
- [205] S. Hasegawa, S. Watanabe, T. Inokuma, Y. Kurata, *J. Appl. Phys.* **77** (1995) 1938-

1946.

## The meaning of the symbols used in the text

a	lattice parameter of a cubic crystal
A	active area of the working electrode, or nucleation rate
$a_{\text{Me}}^{z+}$	activity of $\text{Me}^{z+}_{\text{solv}}$ ions in electrolyte
B	magnetic flux density
c	concentration
C	capacitor, or electrochemical cell
d	distance between two crystalline lattice planes
D	diffusion coefficient
E	electrical potential, or electrolyte
$E_0$	standard electrode potential
$E_a$	anisotropy energy
$E_{\text{dep}}$	deposition potential
$f_0$	resonance frequency of an unloaded quartz
f	resonance frequency
F	Faraday constant ( $96485 \text{ C mol}^{-1}$ )
$\Delta f$	shift of the resonance frequency
$\Delta f^*$	complex resonance shift ( $\Delta f^* = \Delta f + i\Delta w$ )
$F_{\nabla B}$	force generated by the gradient of the magnetic field
$F_{\nabla c}$	force generated by the concentration gradient
fcc	face-centred-cubic
$F_L$	Lorentz force
H	applied magnetic field
$H_a$	Hartman' number ( $H_a =  B (L/2)(\sigma_{\text{av}} * \mu_{\text{av}})$ )
$H_c$	coercivity
hcp	hexagonal-closed-packed
(hkl)	Miller's indexes
HT	Heerman-Tarallo model for nucleation and growth
i	imaginary part ( $i^2 = -1$ )
I	electric current
$I_0(\text{hkl})$	standard intensity in JCPDS, corresponding to the (hkl) plane
$I(\text{hkl})$	measured intensity of the diffraction pattern corresponding to a crystalline plane (hkl)

$j$	current density
$k$	constant that characterize the radial growth of a nucleus radius
$K_i$	anisotropy constants
$L$	distance between cathode and anode, or grain size, or an inductor
$L_x, L_y$	dimensions of a surface
$m$	magnetic moment, or deposited mass
$M$	magnetization, or molar mass
$Me$	metal
$Me_{ads}$	adsorbed $Me$ atoms
$M(hkl)$	orientation index
$M_s$	magnetization of saturation
$N_0$	nucleation sites
$n$	an integer
$N$	total number of growing nuclei
$NC$	natural convection
$N, S$	magnetic poles of the electromagnet (north and south poles)
$Q$	quartz crystal
$R$	universal gas constant ( $8.315 \text{ J K}^{-1} \text{ mol}^{-1}$ ), or resistor
$R_a$	mean roughness
$r_{crit}$	critical radius of a spherical nucleus
$r_d$	radius of a nucleus
$R_m$	motional resistance
$R_q$	roughness of the layers, defined as the standard deviation of the $Z$ values within a given area
$S$	substrate
$SH$	Scharifker-Hills model for nucleation and growth
$SM$	Scharifker-Mostany model for nucleation and growth
$SRWBS$	Sluyters-Reybach model for nucleation and growth
$S(t)$	planar area of independently growing nuclei
$t$	time
$t_q$	thickness of the quartz crystal
$T$	temperature
$u$	moment when the nucleus was born
$v$	scan rate



$V_m$	molar volume
$w_0$	full width at half maximum of an unloaded quartz
$w$	full width at half maximum of a quartz crystal
$\Delta w$	full width at half maximum, FWHM
$z$	number of transferred electrons
$Z$	height values on z axis in an AFM topography image
$Z_{ave}$	the averaged height value in an AFM topography image
$Z_i$	the current height value in an AFM topography image
$Z_m^*$	mechanical impedance ( $Z_m^* = Z_m' + i Z_m''$ )
$Z_q$	mechanical impedance of the quartz ( $Z_q = (\mu_q \cdot \rho_q)^{1/2}$ )
$\alpha$	a constant ( $\alpha = 2\pi \cdot (2MDc/\rho)^{1/2}$ )
$\alpha_1, \alpha_2, \alpha_3$	angles between magnetization vector and the axis of the cube
$\chi_m$	molar susceptibility
$\gamma$	surface energy
$\eta$	overpotential, or current efficiency
$\Phi$	Dawson's integral
$\lambda$	wavelength (of the X-Ray, for example)
$\mu_0$	vacuum permeability, ( $\mu_0 = 4\pi \cdot 10^{-7} \text{ H m}^{-1}$ )
$\mu_{av}$	averaged dynamic viscosity
$\mu_q$	shear modulus of the quartz crystal ( $2.957 \cdot 10^{10} \text{ N m}^{-2}$ )
$\theta$	incident angle of the X-Ray beam on the plane of the sample, or surface coverage
$\rho$	density
$\rho_q$	density of the quartz crystal ( $2684 \text{ Kg m}^{-3}$ )
$\sigma_{av}$	average conductivity between the bulk and electrode surface

## Abbreviations

AFM	Atomic Force Microscopy
CE	counter electrode
DMM	Digital MultiMeter
EDX	Energy Dispersive X-Ray
EQCM	Electrochemical Quartz Crystal Microbalance
HER	Hydrogen Evolution Reaction
JCPDS	Joint Committee for Powder Diffraction Studies
LIGA	Lithographie, Galvanoform, Abformung
MEMS	microelectromechanical systems
MHD	Magnetohydrodynamics, magneohydrodynamic effect
NA	Network Analyser
NSE	Navier-Stokes Equation
PLO	Phase Lock Oscillator
RE	reference electrode
SCE	Saturated Calomel Electrode
SDS	Na dodecylsulfate
SEM	Scanning Electron Microscopy
STM	Scanning Tunnelling Microscope
Sulfirol 8	Na 2-ethylhexyl sulfate
UPD	under potential deposition
VCO	Voltage Controlled Oscillator
VSM	Vibrating Sample Magnetometer
WE	working electrode
XRD	X-Ray Diffractometer

## VII. Appendix

### Levenberg-Marquardt Method

One often wants to compare a set of obtained results with a model, which is based on some underlying theory. If the obtained data satisfy the model, then some useful parameters can be obtained by fitting the experimental data with the chosen or designed model. Usually, the fitting procedure starts with designing of a *merit function*. This is a function which measures the agreement between the model and the experimental data. The merit function has some adjustable parameters, which will be adjusted during the fitting procedure. When the merit function reaches its minimum (which means that the closest agreement between the model and the experimental data is reached) the best fit parameters are obtained.

Suppose that one chooses a model that depends nonlinearly on a set of  $n$  unknown parameters. In this case, in order to find the minimum of the merit function, successive iterations are made. The Levenberg-Marquardt method is one of the methods that works well in practice and that has become a standard routine for a nonlinear fitting. The Levenberg-Marquardt method is implemented in the Origin program for a non-linear curve fit analysis.

In order to start a minimization, the user has to provide initial (guess) values for the parameters wanted. Then the merit function with these parameters is calculated. The parameters that are allowed to vary will be increased by a small value, which is determined from solving a linearized form of the merit function. The merit function for these new parameters is calculated and compared to its previous value. If the new value of the merit function is larger than its initial value, then the starting parameters will be increased by one order of magnitude, for example. The linearized form of the merit function is solved again for determining the new value which should be added to the (second) starting parameter. Then the merit function for the new parameters will be again calculated and compared with the previous values, etc... If after the first iteration the merit function with the new parameters was smaller than the initial merit function, then the new starting parameters will be considered those which were obtained after the first iteration. The algorithm will then continue, until a minimum value of the merit function is obtained.

The expressions of the current density as a function of the nucleation sites ( $N_0$ ) and nucleation rate ( $A$ ), obtained in the Heerman-Tarallo and Scharifker-Mostany models (Eq. 20, p.28 and Eq. 21, p.29), were used as the merit functions in the present study. All the fitting procedures were done with Origin. Thus, by selecting in an Origin worksheet the

following procedures: *Analyse*->*Non-linear curve fit*->*Advanced Fitting Tools*, one obtains a dialog window. Here one defines a new function that can be implemented for fitting the data. Thus, the number of unknown parameters that can vary and the expression of the function can be defined. One can also save the new fitting model. Seven parameters were defined:  $z$  (the number of the transferred electrons),  $D$  (diffusion coefficient),  $c$  (concentration),  $M$  (molar mass),  $\rho$  (density),  $A$  (nucleation rate) and  $N_0$  (nucleation site density). Just  $A$  and  $N_0$  were allowed to vary. A data set was selected (current density values recorded during a potentiostatic deposition and the corresponding time). Then, one can select the number of successive iterations wanted, (from one to one hundred). The fitting procedure was stopped when the difference in two successive iterations did not improve the error in  $A$  and  $N_0$ .

## Acknowledgments

This work was carried out in the Technical University of Dresden, in the department of Electrochemistry and Physical Chemistry, from 2003 until 2007. The first thank goes to Professor Waldfried Plieth, who supervised my work. For the discussions and for the stimulating ideas I am grateful.

To Dr. Andreas Bund I would like to thank for the appreciable help that he gave me within all these years. His corrections and suggestions in writing all the articles and the proceedings are highly appreciated. I am deeply grateful for the scientific discussions, especially for the help in interpretation of the experimental results. His help in designing the electrochemical cells that were used in my work is appreciated. I would like to thank my supervisors, Professor Plieth and Dr. Bund for giving me the opportunity to participate in many and very interesting national and international conferences.

In the beginning of my work in electrochemistry I got a lot of help and advices from some colleagues of the Physical Chemistry department. Therefore, I would like to express my deep gratitude to Dr. Susanne Wehner, Dr. Holger Sahrhage, Franziska Wünsche, Silvio Köhler and Holger Kühnlein. I am grateful to Eveline Zschippang, Denny Thiemig, Romy Marx and Daniela Wuttig for the assistance with some measurements.

I am also thankful to Dr. Hisayoshi Matsushima, (from Kyoto University, Japan, who was a Humboldt fellow in our working group for two years) and to Professor Benedetto Bozzini (University of Lecce, Italy) for the interesting and helpful discussions.

Many thanks are addressed to Ellen Kern (TU Dresden, Physical Chemistry) for the SEM and EDX measurements and to Anja Bensch (TU Dresden, Inorganic Chemistry) for the XRD measurements. I express my deep gratitude for the help of Dr. Mihai Stoica and Dr. Stefan Roth (from IFW Dresden) in the VSM measurements. I would like to thank Matthias Gestrich (TU Dresden) who build most of my experimental cells and to Wilfried Otte who build the electronic contacts of the cells.

Special thanks are addressed to Professor Roger Grundmann and Catrin Muehlfriedel for the permanent support and for the help within the SFB 609, and to Waltraud Ahnefeld, the secretary of Physical Chemistry department, who help me all the time with all the administration problems.

I am grateful to my family, and to my friends that supported me all the time. I would like to thank all my colleagues (from TU Dresden, department of Electrochemistry and Physical Chemistry) and friends for making my stay in Dresden University full of nice memories.



Die vorliegende Arbeit wurde am Institut für Physikalische Chemie und Elektrochemie der Technischen Universität Dresden unter wissenschaftlicher Betreuung von Herrn Prof. W. Plieth und Herrn PD A. Bund angefertigt.

Hiermit versichere ich, dass ich die vorliegende Arbeit ohne unzulässige Hilfe Dritter und ohne Benutzung anderer als der angegebenen Hilfsmittel angefertigt habe; die aus fremden Quellen direkt oder indirekt übernommenen Gedanken sind als solche kenntlich gemacht. Die Arbeit wurde bisher weder im Inland noch im Ausland in gleicher oder ähnlicher Form einer anderen Prüfungsbehörde vorgelegt.

Adriana Ispas

Dresden, 12.04.2007